Repulsive Sema3E-Plexin-D1 signaling coordinates both axonal extension and steering via activating an autoregulatory factor, Mtss1

Namsuk Kim[1§], Yan Li[1§], Ri Yu[1], Hyo-Shin Kwon[1], Anji Song[1], Mi-Hee Jun[1], Jin-Young Jeong[1,2], Ji Hyun Lee[1], Hyun-Ho Lim[1], Mi-Jin Kim[3], Jung-Woong Kim[3], and Won-Jong Oh[1]*

[1]Neurovascular Unit Research Group, Korea Brain Research Institute, Daegu 41062, Republic of Korea

[2]Department of Brain and Cognitive Sciences, Daegu Gyeongbuk Institute of Science and Technology, Daegu 42988, Republic of Korea

[3]Department of Life Sciences, Chung-Ang University, Seoul 06974, Republic of Korea

[§]These authors contributed equally to this work.

*Corresponding author

E-mail: ohwj@kbri.re.kr (WJO)

Abstract

Axon guidance molecules are critical for neuronal pathfinding because they regulate directionality and growth pace during nervous system development. However, the molecular mechanisms coordinating proper axonal extension and turning are poorly understood. Here, Metastasis Suppressor 1 (Mtss1), a membrane protrusion protein, ensured axonal extension while sensitizing axons to the Semaphorin 3E (Sema3E)-Plexin-D1 repulsive cue. Sema3E-Plexin-D1 signaling enhanced Mtss1 expression in projecting striatonigral neurons. Mtss1 localized to the neurite axonal side and regulated neurite outgrowth in cultured neurons. Mtss1 also aided Plexin-D1 trafficking to the growth cone, where it signaled a repulsive cue to Sema3E. Mtss1 ablation reduced neurite extension and growth cone collapse in cultured neurons. *Mtss1*-knockout mice exhibited fewer striatonigral projections and irregular axonal routes and these defects were recapitulated in *Plxnd1*- or *Sema3e*-knockout mice. These findings demonstrate that repulsive axon guidance activates an exquisite autoregulatory program coordinating both axonal extension and steering during neuronal pathfinding.

Keywords: Axon guidance, Semaphorin3E, Plexin-D1, Mtss1, Basal ganglia development

Introduction

In the developing nervous system, axons of newly generated neurons extend toward destination targets and make connections to establish a functional circuit following an exquisitely designed program. In this long-range pathfinding process, axons encounter attractive and repulsive signals from guidance molecules, and diverse combinations of ligand-receptor pairs communicate signals to a neuron from the environment (Kolodkin and Tessier-Lavigne, 2011; Tessier-Lavigne and Goodman, 1996). In addition to the conventional guidance mode, which has been established, recent studies have demonstrated the complexity of signaling through different mechanistic layers, such as crosstalk between guidance molecules (Dupin et al., 2015; Poliak et al., 2015), guidance switching between different holoreceptor complexes (Bellon et al., 2010) or guidance tuning by intrinsic regulators (Bai et al., 2011; Bonanomi et al., 2019). In general, the specific cognate guidance receptors that sense extracellular signals are mostly localized in growth cones, a specialized structure at the fore of a growing axon, and these receptors convey intracellular signaling cues within neurons (Dent et al., 2011; Franze, 2020). Therefore, proper signaling from guidance molecules in the growth cone surface is critical as axons travel to their destination. Because the axonal destination can be as far as a meter or more away from the soma, various transport systems consisting of specific adaptors and motor proteins transport guidance proteins to axon terminals and are thus critical for axonal movement (Dent et al., 2011; Winckler and Mellman, 2010). However, how individual guidance molecules are correctly delivered to growth cones and can accommodate the axonal growth pace is unclear, and the molecular machinery critical for the specific transportation of guidance molecules is unknown.

Growth cones are highly dynamic and motile cellular structures that facilitate axon growth and steering through activated receptors that alter cytoskeletal actin and microtubule assembly (Lowery and Vactor, 2009; Vitriol and Zheng, 2012). Therefore, guidance receptors undoubtedly need to be localized to these protrusive structures to control actin dynamics. Since actin filament assembly is typically accompanied by membrane remodeling, a group of cytoskeletal scaffold proteins linking actin to the cell membrane must be activated (Vitriol and Zheng, 2012). One such protein group consists of Bin/Amphiphysin/Rvs (BAR) domain proteins, which have been implicated in many actin-associated membrane functions, such as cell motility, endocytosis, and organelle trafficking (Chen et al., 2013). Among these proteins, metastasis suppressor 1 (Mtss1, also called missing in metastasis), one of a few inverse BAR (I-BAR) domain subfamily proteins, is notable due to its capability of

forming cellular protrusions by promoting inverse membrane curvature (Machesky and Johnston, 2007). Because of its unique ability to connect the plasma membrane inner leaflet with actin, the role of Mtss1 has been characterized in promoting spine protrusions as well as neuronal dendrite growth (Galbraith et al., 2018; Saarikangas et al., 2015; Yu et al., 2016). However, in contrast to these many studies of Mtss1 on the dendritic side during development, few studies have investigated whether Mtss1 is expressed and plays a specific role in axons.

Semaphorin 3E (Sema3E), a class-3 secreted semaphorin family protein, conveys guidance signals by directly binding with the Plexin-D1 receptor in both the nervous and vascular systems (Gu et al., 2005; Oh and Gu, 2013a). The Sema3E-Plexin-D1 pair mainly transmits a repulsive guidance cue via local cytoskeletal changes, thereby inhibiting axonal overgrowth and/or ectopic synapse formation in the central nervous system (Chauvet et al., 2007; Ding et al., 2012; Fukuhara et al., 2013; Mata et al., 2018; Pecho-Vrieseling et al., 2009). Previous studies have demonstrated that Sema3E-Plexin-D1 signaling is involved in dendritic synapse formation as well as traditional axon projection in the basal ganglia circuitry, which is essential for diverse behavioral and cognitive functions in the brain (Ding et al., 2012; Ehrman et al., 2013). Notably, Plexin-D1 is expressed only in direct-pathway medium spiny neurons (MSNs) projecting to the substantia nigra pars reticulata (SNr), one of two distinct types of MSNs in the striatum (Ding et al., 2012). Plexin-D1-positive striatonigral axons travel through the corridor between the globus pallidus (Gp) and reticular thalamic nucleus (rTh)/zona incerta (ZI), in which Sema3E molecules reside and emit repulsive signals to direct proper pathway formation toward the SNr (Chauvet et al., 2007; Ehrman et al., 2013). However, how the striatonigral pathway coordinates axonal growth and steering during pathfinding remains largely unknown.

In this study, we investigated the molecular mechanism of the repulsive Sema3E-Plexin-D1 guidance signaling pair in striatonigral-projecting neurons during mouse basal ganglia circuit development. We found that Sema3E-Plexin-D1 signaling coordinates axonal extension and diversion by enhancing the action of the facilitator protein Mtss1 during active striatonigral projection progression. In the context of the important and intricate networks in the brain, this study provides evidence showing that autoregulatory factor expression regulated by guidance signaling leads to the correct neuronal trajectory to the destination.

Results

Sema3E-Plexin-D1 signaling regulates Mtss1 expression in the developing striatum

The majority of striatal neurons are MSNs (up to 90%), and the MSNs are equally divided into direct and indirect pathways (Gerfen and Surmeier, 2011). In a previous study, we found that *Plxnd1* is selectively expressed in direct-pathway MSNs (also called striatonigral neurons) that project directly to the substantia nigra, with approximately 45% of striatal neurons identified as Plexin-D1-positive neurons (Ding et al., 2012). Because of the relative abundance of Plexin-D1-positive neurons, we expected a high probability of discovering the potential downstream responsive genes modulated by Sema3E-Plexin-D1 signaling in the striatum. Therefore, we performed bulk RNA sequencing (RNA-seq) with striatal tissues at P5, when *Plxnd1* expression is high in the striatum, and compared the results obtained with control (*Plxnd1*$^{f/f}$) and conditional neuronal *Plxnd1*-knockout (*Nes-Cre; Plxnd1*$^{f/f}$) mice (Figure 1A). *Plxnd1* mRNA ablation in striatal tissues was validated in pan-neuronal *Plxnd1*-knockout (Nestin-Cre) mice (Figures S1A and S1B).

Next, we performed gene expression profile analysis. The principal component analysis (PCA) plot showed that *Plxnd1*-knockout accounted for the largest variance, and the results obtained in biological replicates showed high reproducibility (Figure S1C). Application of a conservative DEseq approach to RNA-seq data analysis confirmed 2,360 differentially expressed transcripts (Figure S1D). Gene Ontology (GO) analysis was then performed, and biological connections between upregulated (1,240 transcripts) and downregulated (1,120 transcripts) differentially expressed genes (DEGs) in *Plxnd1*-knockout mice compared to wild-type (control) mice were identified (Figure S1E). Clustering of the downregulated DEGs in *Plxnd1*-knockout mice enabled their classification into several categories that were associated with axon guidance, regulation of dendritic spine morphology, and neuronal projection. The volcano plots present the statistical significance of differential transcript expression with the respective fold change values ($P < 0.05$, absolute log2 (fold change, FC) > 1) compared to the expression observed in the control group (Figure 1B).

Among the downregulated genes, Mtss1 was particularly notable due to its high relevance to actin cytoskeletal rearrangement (Galbraith et al., 2018; Lin et al., 2005; Saarikangas et al., 2015). *Mtss1* gene expression was verified by quantitative RT–PCR (qRT–PCR) performed with *Plxnd1*-knockout striatal tissues (Figures 1C). The Mtss1 protein levels were also markedly decreased in the knockout mice at P5 (Figures 1D and 1E). We also analyzed Mtss1 expression in *Sema3e*-knockout striatal samples obtained at P5 and found that its

96 expression was decreased, but less dramatically than it was in *Plxnd1*-knockout striatal samples (Figures 1F and
97 1G). These results suggest that Sema3E-Plexin-D1 signaling activation can increase Mtss1 expression in striatal
98 neurons during development.
99
100 **Mtss1 is selectively expressed in striatonigral-projecting neurons during the active pathfinding period**
101 To determine whether this Mtss1 expression is specific to Plexin-D1-positive neurons, we first performed
102 fluorescence *in situ* hybridization. Mtss1 expression significantly overlapped with *Plxnd1*-positive neurons in
103 both the cortex and striatum, and its expression was reduced in *Plxnd1*-knockout mice (Figures 1H and 1I).
104 Moreover, when we performed immunostaining with Drd1a-tdT mice, in which direct-pathway MSNs fluoresced
105 red (Ade et al., 2011), Mtss1 expression significantly overlapped with Drd1a-tdT striatal neurons (Figure 1J; 98.2
106 ± 1.72%), suggesting that Plexin-D1 signaling mediates Mtss1 expression selectively in striatonigral projecting
107 MSNs. Although Mtss1 was expressed at a low level regardless of Plexin-D1 presence at E16.5, it seemed to be
108 under the control of Plexin-D1 signaling in the developing striatum from the last gestation period to the early
109 postnatal period (Figures 1K and 1L). Furthermore, the Sema3E ligand activating the Plexin-D1 receptor was
110 predominantly expressed in the thalamus and released into the striatum, probably during thalamostriatal projection
111 at E16.5, as observed in the early postnatal stage in a previous study (Figure S2) (Ding et al., 2012). Next, we
112 analyzed the expression profiles of Plexin-D1 and Mtss1 from the developmental stage to the adult stage. Both
113 Plexin-D1 and Mtss1 were expressed in the embryonic striatum, and their expression was elevated in the perinatal
114 stage. Interestingly, Mtss1 expression was maintained at a relatively high level from E18.5 to P5 and then declined
115 sharply and disappeared in the adult striatum, and although Plexin-D1 showed a similar expression pattern, its
116 expression was maintained at a low level in the adult striatum, presumably to regulate other functions such as
117 thalamostriatal synapse formation (Figures 1M and 1N) (Ding et al., 2012).
118
119 **Sema3E-Plexin-D1 signaling regulates Mtss1 expression in cultured medium spiny neurons**
120 To determine whether Plexin-D1-driven Mtss1 expression can be recapitulated *in vitro*, we compared the Mtss1
121 levels in cultured striatal neurons isolated from wild-type and *Plxnd1*-null mice. In wild-type neurons, both Plexin-
122 D1 and Mtss1 expression levels were low at day 3 *in vitro* (DIV3) and then increased by DIV6. In contrast,
123 *Plxnd1*-knockout neurons failed to elevate Mtss1 expression by DIV6, suggesting that Mtss1 expression is

124 induced at the cellular level rather than by indirect systemic changes at the circuit level *in vivo* (Figures 2A and
125 2B). In addition, the expression of Mtss1 was decreased in cultured *Sema3e*-knockout neurons (Figures 2C and
126 2D). Next, to further confirm that the Sema3E-Plexin-D1 guidance pair is required for the activation of Mtss1
127 expression in striatonigral neurons, we supplemented the *Sema3e*- or *Plxnd1*-knockout neurons with exogenous
128 Sema3E ligand according to the scheme in Figure 2E. Given that some Sema3E ligands are naturally present in
129 our striatal cultures from globus pallidus neurons, conducting tests on the exogenous Sema3E effect in the
130 *Sema3e*-knockout cultures is ideal to minimize experimental variation. In fact, Mtss1 expression was increased
131 by Sema3E replenishment in *Sema3e*-knockout neurons, whereas it was not altered in *Plxnd1*-knockout neurons
132 (Figures 2F-2I). Moreover, since Akt is already known to mediate the Sema3E-Plexin-D1 signaling cascade in
133 neurons (Burk et al., 2017), we next examined whether disturbing Akt activity alters Mtss1 expression in cultured
134 neurons. Treatment with an Akt inhibitor, MK2206, downregulated Mtss1 expression but caused no changes in
135 Plexin-D1 levels (Figures 2J-2M). Furthermore, the elevated expression of Mtss1 due to the addition of exogenous
136 Sema3E supplement in *Sema3e*-knockout neurons was also diminished by MK2206, suggesting that the Sema3E-
137 Plexin-D1 pathway is involved in Mtss1 expression through Akt signaling (Figures 2N and 2O). These results
138 suggest that Mtss1 is a downstream expression target of Sema3E-Plexin-D1 signaling in direct-pathway MSNs.
139

140 **Mtss1 is important for neurite extension in direct-pathway MSNs**

141 Since Mtss1 has a well-characterized role in the regulation of filopodia and spine precursors (Saarikangas et al.,
142 2015; Yu et al., 2016), we first tested the morphological changes induced by Mtss1 in COS7 cells. Mtss1 was
143 weakly expressed in COS7 cells, but its levels were not altered after overexpressing Plexin-D1 with or without
144 Sema3E (Figures S3A and S3B). Mtss1 overexpression in COS7 cells led to a diverse degree of morphological
145 changes, such as excessively spiky or thin and long processes, and highly localized in F-actin-enriched protrusions.
146 However, overexpression of Mtss1 lacking the I-BAR domain failed to generate these protrusive shapes (Figures
147 S3C and S3D). Mtss1 lacking WH2 domain showed much weaker effect because WH2 is an important region for
148 Mtss1 interaction with F-actin (Mattila et al., 2003). These results suggest that Mtss1 is involved in F-actin
149 dynamics and thus may be an important regulator of neurite outgrowth in cultured MSNs, similar to the situations
150 in other types of neurons (Galbraith et al., 2018; Saarikangas et al., 2015; Yu et al., 2016).

151 Interestingly, Mtss1 was significantly localized to the Tau-positive-axonal side of cultured MSNs at

152 DIV3 (Figure 3A). We measured the neurite length of the direct-pathway MSNs that had been genetically labeled
153 with red fluorescence in Drd1a-tdT crossbred reporter mice. We observed significant growth retardation in MSNs
154 lacking *Mtss1* compared to wild-type neurons at DIV3 and DIV6 (Figures 3B-3C and 3E-3F). Furthermore, we
155 also observed that *Mtss1*-deficient neurons failed to extend neurites more than twice the size of the cell body,
156 suggesting that a lack of *Mtss1* presumably caused a severe neurite growth defect (Figure 3D). Next, we analyzed
157 neurite length in *Plxnd1*-knockout neurons. Interestingly, there was no difference in neurite length between Drd1a-
158 positive wild-type MSNs and *Plxnd1*-knockout MSNs at DIV3 (Figures 3G and 3H), probably due to the low
159 Mtss1 induction shown in Figure 2A, whereas the length was significantly reduced in the *Plxnd1*-deficient MSNs
160 at DIV6 (Figures 3I and 3J). These results suggest the possibility that Mtss1 expression is independent of Plexin-
161 D1 signaling in the young neurons as observed in early development (Figure 1K). However, Mtss1 expression
162 appears to be highly induced by Sema3E-Plexin-D1 activation to regulate axonal extension as neurons mature. To
163 further confirm that low Mtss1 expression is critical for shortening neurite outgrowth, we overexpressed Mtss1 in
164 *Plxnd1*-deficient MSNs. In comparison to the neurite length observed in GFP-overexpressing MSNs, ectopic
165 Mtss1 overexpression rescued the growth reduction phenotype in the *Plxnd1*-knockout neurons (Figures 3K and
166 3L). These results suggest that the Sema3E-Plexin-D1 repulsive guidance cue is capable of regulating axonal
167 growth through positive facilitator proteins such as Mtss1.
168
169 **The Mtss1 I-BAR domain binds to Plexin-D1, and this interaction is Sema3E-independent**
170 Since both Plexin-D1 and Mtss1 regulate actin cytoskeletal rearrangement as a guidance molecule and membrane
171 transformer, respectively, near the cell surface, we speculated that Plexin-D1 and Mtss1 might interact with each
172 other via the BAR domain to induce actin-related cellular events. To test whether Plexin-D1 and Mtss1 can
173 physically interact, we generated multiple deletion constructs of human Plexin-D1 and Mtss1 (Figure 4A). When
174 we overexpressed full-length Plexin-D1 and Mtss1 together in HEK293T cells, both proteins were successfully
175 pulled down together (Figure 4B). However, Plexin-D1 with the intracellular domain (ICD) deleted failed to bind
176 Mtss1, indicating an intracellular Plexin-D1 and Mtss1 interaction (Figure 4C). When we overexpressed full-
177 length Plexin-D1 and each Mtss1 deletion construct, every Mtss1 construct containing the I-BAR domain
178 coprecipitated with Plexin-D1, but I-BAR-deficient Mtss1 failed to interact with Plexin-D1 (Figure 4D). In a
179 previous study, it was determined that Plexin-D1 interacts with SH3-domain binding protein 1 (SH3BP1), another

180 protein of the BAR domain family (Tata et al., 2014), thus we investigated whether Plexin-D1 also binds to other
181 BAR domain-containing proteins in general. As previously reported, we found that overexpression of Plexin-D1
182 in HEK293T cells resulted in the formation of a complex with overexpressed SH3BP1 (Figure S4A). However, it
183 did not form a complex with srGAP2, a protein containing an F-BAR domain, or IRSP53, another protein
184 containing an I-BAR domain like Mtss1 (Figure S4B and S4C). Conversely, we also examined whether Mtss1
185 can interact with other members of the Plexin family. As shown in Figures S4D and S4E, overexpressed Mtss1
186 was unable to form a complex with Plexin-B2 or -B3 proteins. These findings suggest that the formation of the
187 Plexin-D1-Mtss1 complex is relatively specific.

188 Since Sema3E binding to Plexin-D1 caused SH3BP1 release from the complex (Tata et al., 2014), we
189 examined whether Sema3E binding influences Mtss1 dissociation from Plexin-D1. In contrast to the effect on
190 SH3BP1, Sema3E treatment did not interfere with Plexin-D1-Mtss1 complex formation, indicating that the
191 complex is formed in a Sema3E-independent manner (Figures 4E and 4F). Moreover, to determine whether
192 Plexin-D1 and Mtss1 can bind directly to each other, we performed an *in vitro* protein-protein binding assay using
193 the purified intracellular domain of Plexin-D1 and the I-BAR domain of Mtss1 proteins. As shown in Figure 4G,
194 both proteins precipitated together, suggesting that Plexin-D1 and Mtss1 play a role as direct binding partners.
195

196 **Mtss1 transports Plexin-D1 to the growth cone in cultured direct-pathway MSNs**

197 Because of the high probability of localization of the Plexin-D1-Mtss1 complex at the cell membrane, Mtss1 may
198 regulate Plexin-D1 function at the cell surface. To investigate the role of Mtss1 in Plexin-D1 activity, we first
199 examined whether Mtss1 affects the Plexin-D1 level on the plasma membrane by performing a surface molecule
200 biotinylation analysis. We observed that overexpressed Plexin-D1 proteins in COS7 cells were efficiently
201 biotinylated on the cell surface, but the Plexin-D1 protein level on the surface was not changed during Mtss1
202 coexpression (Figures S5A and S5B). Another potential mechanism by which Mtss1 may affect Plexin-D1 activity
203 might be endocytic regulation because Plexin-D1 is rapidly endocytosed after Sema3E treatment (Burk et al.,
204 2017). However, Mtss1 coexpression did not affect Sema3E-induced Plexin-D1 endocytosis (Figures S5C and
205 S5D). Additionally, Mtss1 overexpression did not change the binding affinity of Sema3E for Plexin-D1 (Figure
206 S5E). These data, including those regarding Sema3E-independent complex formation (Figures 4E and 4F),
207 suggest that Mtss1 does not directly affect the functional role of Sema3E-Plexin-D1 at the cell-surface level.

208 We next hypothesized that Mtss1 forms a complex with Plexin-D1 that targets Plexin-D1 to filopodium-
209 like structures, since we observed that Mtss1 is mainly involved in protrusion formation and neurite outgrowth in
210 cultured cells. To test this possibility, we coexpressed Plexin-D1 and Mtss1 and analyzed their localization in
211 COS7 cells. As shown in Figures S5F and S5G, when Plexin-D1 and Mtss1 were coexpressed, both proteins were
212 mostly present in F-actin-enriched protrusions. However, overexpression of Plexin-D1 lacking the ICD
213 overlapped with Mtss1 to a lesser extent than overexpression of wild-type Plexin-D1, whereas Mtss1 was
214 abundant in the protrusions. In addition, Mtss1 lacking the I-BAR domain, which possesses membrane-bending
215 activity, did not generate filopodia-like protrusions in COS7 cells but was localized with F-actin, including in
216 marginal areas, probably via the Mtss1 WH2 domain (Mattila et al., 2003). Interestingly, although Plexin-D1 was
217 evenly distributed throughout a cell, most Plexin-D1 was not present with Mtss1 missing the I-BAR domain. In
218 addition, the localization of Plexin-D1 and Mtss1 in the protrusions was also not disturbed in the presence of
219 Sema3E (Figure S5H). These results suggest that Mtss1 not only induces cell protrusion formation but also
220 contributes to Plexin-D1 localization to specific sites.

221 Next, to confirm that Mtss1 leads Plexin-D1 to protrusive structures, such as growth cones in cultured
222 neurons, Mtss1 and Plexin-D1 localization was analyzed by transfecting *Mtss1*-deficient striatal neurons with
223 expression constructs carrying both proteins. Both overexpressed Plexin-D1 and Mtss1 proteins seemed to be
224 colocalized along growing neurites, but the Mtss1 mutant lacking the I-BAR domain showed reduced Plexin-D1
225 level as well as a low colocalization rate (Figures 5A-5C). As shown in COS7 cells (Figure S5F), wild-type Mtss1
226 proteins were present with Plexin-D1 in F-actin-enriched regions of growth cones; in contrast, mutant Mtss1 was
227 expressed at a lower level than wild-type Mtss1 and failed to colocalize with Plexin-D1, resulting in reduced
228 Plexin-D1 localization in the growth cone (Figures 5D-5F). However, the intensity of Plexin-D1 upon co-
229 expression of wild-type Mtss1 or mutant Mtss1 remained unchanged in the cell body (Figures S6A and S6B). It
230 is plausible that overexpressed proteins accumulate in the soma, and a limited proportion of them are destined to
231 the axon terminal on demand (Droz et al., 1973). To explore the role of Mtss1 in transporting Plexin-D1, we
232 directly monitored the movement of Plexin-D1 along neurites in real-time by imaging Drd1a-positive MSNs
233 expressing Plexin-D1-GFP fusion proteins in wild-type and *Mtss1*-knockout neurons at DIV6. Our live cell
234 imaging showed that the majority of Plexin-D1-containing vesicles were dynamically transported in both proximal
235 and distal directions in wild-type MSNs. In contrast, the Plexin-D1-positive vesicles in *Mtss1*-deficient MSNs

236 remained stationary, and their overall numbers in neurites were also slightly reduced (Figures 5G-5K and Videos
237 1-4). These observations demonstrate that Mtss1 facilitates the dynamic transportation of Plexin-D1 along the
238 growing neurites of direct-pathway MSNs, leading to an increased rate of Plexin-D1 localization in the growth
239 cones.

240 Moreover, to examine whether endogenous Mtss1 expression affects Plexin-D1 localization in the
241 growth cone, leading to an active guidance role, we performed an AP-Sema3E binding analysis in Drd1a-positive
242 MSNs at DIV6 (Gu et al., 2005). The AP-Sema3E binding assay has been used in many previous studies as an
243 alternative method to detect endogenous Plexin-D1 protein due to the lack of reliable anti-Plexin-D1 antibodies
244 (Bellon et al., 2010). The *Mtss1*-knockout neurons exhibited a low level of AP-Sema3E binding in the growth
245 cones, indicating that the endogenous trafficking of Plexin-D1 to the tip of the growing axon is disrupted in the
246 absence of Mtss1 (Figures 5L and 5M). These results suggest that Mtss1 serves to deliver Plexin-D1 to the growth
247 cone.
248

249 **Plexin-D1 trafficking to the growth cone by Mtss1 potentiates the repulsive response to Sema3E**

250 Because Mtss1 facilitates Plexin-D1 transport to the growth cone, proper Plexin-D1 localization at the membrane
251 may contribute to the triggering of repulsive signaling by Plexin-D1 in response to Sema3E. To test this hypothesis,
252 we performed a growth cone collapse assay at DIV3 in direct-pathway MSNs and found that wild-type Drd1a-
253 tdT-positive striatal neurons underwent a high collapse rate after exogenous Sema3E treatment, whereas the
254 growth cones of neurons lacking *Mtss1* did not collapse at a significantly different rate (Figures 6A and 6B).
255 However, reintroduction of wild-type Mtss1 into *Mtss1*-knockout MSNs resulted in growth cone collapse, but
256 overexpressed Mtss1 lacking the I-BAR domain showed less response to Sema3E (Figures 6C and 6D). In addition,
257 *Plxnd1*-null MSNs also showed a very low collapse rate regardless of Sema3E addition at DIV6 (Figure 6E),
258 consistent with a previous report that Sema3E-Plexin-D1 signaling acts as a repulsive guidance cue (Chauvet et
259 al., 2007). The reduced collapse phenotypes were rescued by overexpression of full-length Plexin-D1 but not by
260 ICD-deleted Plexin-D1 (Figure 6F). In summary, Mtss1 targeting of Plexin-D1 to the growth cone is critical for
261 robust Sema3E-induced repulsive signaling.
262

263 **Absence of Mtss1 reduces projection density and Plexin-D1 localization in the striatonigral pathway**

264 First, to determine whether Mtss1 is indeed expressed in the projecting striatonigral axons and their destination,
265 the SNr, we performed immunostaining using wild-type or *Mtss1*-knockout mouse brains. We observed Mtss1
266 localization in the striatonigral tract and SNr, but the immunostaining signal disappeared in *Mtss1*-deficient mice
267 (Figure S7). Although we also detected Mtss1 in the SNr region, we could not rule out the possibility that
268 substantia nigra neurons express Mtss1 at this stage. Next, to investigate the role of Mtss1 in striatonigral pathway
269 development *in vivo*, we performed an AP-Sema3E binding assay to examine the Plexin-D1-positive tract in brain
270 tissue (Chauvet et al., 2007). In mice expressing wild-type *Mtss1*, a significant amount of Plexin-D1 was observed
271 in the neuronal tract reaching the substantia nigra. In contrast, *Mtss1*-knockout mice exhibited a relatively small
272 area of Plexin-D1-positive striatonigral tracts, including both poor neuronal projection and reduced Plexin-D1
273 localization at E17.5 (Figures 7A-7D). In addition, despite these reduced neuronal projections in the *Mtss1*-
274 knockout mice, the density of the AP-Sema3E-positive tracts was reduced even more (Figure 7E), indicating that
275 the absence of Mtss1 prevents both normal axonal projections and Plexin-D1 trafficking. In the coronal view, the
276 bundle density of Plexin-D1-positive projections passing between the rTh and Gp was reduced in the *Mtss1*-
277 knockout mice (Figure 7F). Because most mice with conditional Nestin-Cre-driven *Mtss1* deletion were born alive,
278 we analyzed the Plexin-D1-positive striatonigral pathway at P5. Consistent with the results obtained with E17.5
279 embryos, *Mtss1*-deficient neonates showed fewer Plexin-D1-positive striatonigral projections in the coverage area
280 and a reduced path width (Figures 7G-7J).

281 To further identify Plexin-D1-positive striatonigral pathway defects, we crossed Drd1a-tdT transgenic
282 reporter mice with conditional *Mtss1*-knockout mice and visualized the pathway in the offspring. Consistent with
283 the results shown in AP-Sema3E binding experiments, the total boundary area with Drd1a-tdT-positive
284 projections was smaller and less compact in the *Mtss1*-knockout mice than in the wild-type mice at P5 (Figures
285 7K-7M). At P30, the projection density defects were more obvious, but the boundary area in the wild-type and
286 mutant mice was not significantly different, indicating that *Mtss1* deficiency led to the formation of fewer
287 striatonigral axonal bundles (Figures S8A-S8C). We assumed that Mtss1 regulates the initial striatonigral axonal
288 projection during development of the neonate and that the pathway establishment ends by P7 (Morello et al.,
289 2015); therefore, the scarcity of the projections may be clearer when the brain increases to the adult size. Moreover,
290 we examined whether Mtss1 expression affects Plexin-D1 levels on the Drd1a-tdT-positive tracks at P5, using the
291 same methodology as employed at E17.5 (Figure 7A). Our findings revealed a decreased ratio of AP-Sema3E

292 binding per tdT staining, suggesting that Mtss1 is implicated not only in axonal projections but also in Plexin-D1
293 trafficking in navigating striatonigral projections (Figures 7N-7Q).
294 We then investigated whether Mtss1 specifically contributes to the development of descending
295 striatonigral projections rather than dendritic arborization. Since global *Mtss1*-mutant mice have enlarged brain
296 ventricles and decreased cortical thickness (Minkeviciene et al., 2019), we first examined whether the axonal
297 projection in *Mtss1*-knockout mice is due to cellular death of MSNs in the striatum. Using cleaved caspase 3
298 staining to detect apoptotic cells, we found few dying cells in the wild-type and *Mtss1*-mutant neonates (Figures
299 S9A and S9B), indicating that no significant cell pathology was induced by *Mtss1* expression deficiency. Because
300 Mtss1 is selectively expressed in direct-pathway MSNs, which comprise approximately 45% of striatal neurons
301 (Figure 1), we expected that Golgi staining would be sufficient to detect any dendritic defects, such as aberrant
302 number and/or length of branches. However, we found no detectable difference between the wild type and *Mtss1*
303 mutants at P5 (Figures S9C-S9E). In addition, no significant change in Plexin-D1 levels was observed in the
304 striatum or cultured neurons of *Mtss1*-deficient mice compared to those in littermate controls (Figures S9F-S9I).
305 These results indicate that the weakening of the Plexin-D1-positive striatonigral pathway in *Mtss1*-knockout mice
306 is caused by both impairments of neuronal projections and inappropriate Plexin-D1 distribution due to Mtss1
307 downregulation.
308
309 **The absence of Plexin-D1 or Sema3E reduces the axonal projection of direct-pathway MSNs**
310 Since Mtss1 expression is under the control of Sema3E-Plexin-D1 signaling, we investigated whether *Plxnd1*
311 deletion leads to phenocopying of the striatonigral projection defects observed in *Mtss1*-knockout mice. During
312 the neonatal period, the boundary area and compactness of descending striatonigral projections were small and
313 loose in the *Plxnd1*-knockout mice, but only a reduced projection density was observed in adult mice, which was
314 similar to that of *Mtss1*-knockout mice (Figures 7R-7T and S8D-S8F). Moreover, *Sema3e*-knockout at P5 also
315 showed these projection defects, albeit somewhat milder compared to those observed in *Plxnd1*- or *Mtss1*-
316 deficient mice (Figure S10A-S10E). These phenocopy results suggest that activation of Sema3E-Plexin-D1
317 signaling, which leads to induction of Mtss1, is required for the striatonigral trajectory during the axonal
318 pathfinding period.
319

320 **Absence of Mtss1 or Plexin-D1 results in irregular projection patterns in direct-pathway MSNs**

321 Subsequently, we examined whether striatonigral projection patterns are altered by Mtss1 deficiency. Interestingly,
322 we observed that the descending striatonigral projections in the wild-type mice were relatively straight and
323 untangled near the Gp region through the sagittal view (Figure 8A). When visualizing the striatonigral projection
324 using 3-D imaging by sparsely labeling with DiI injection at the dorsal striatum, the axonal bundles appeared
325 relatively fasciculated and straight in the wild-type at P5 (Figures 8B and 8C). However, *Mtss1* mutants showed
326 irregular projection patterns with random directionality and mild defasciculation (Figures 8A-8C). To assess
327 axonal deviation, we measured the number of projections intersecting each other in the same region, as shown in
328 Figures 8A and 8B. The deficiency of Mtss1 led to more deviant ectopic projections (Figure 8E). However, the
329 misguidance defects were not apparent at P30, likely because abnormal projections were discarded as mice
330 matured into adults (Figure S8G). These results suggest that inefficient Plexin-D1 trafficking to the extending
331 axons in the *Mtss1*-knockout mice may have weakened the proper guidance response.

332 Previous studies have reported that Sema3E-Plexin-D1 signaling defects lead to ectopic projection during
333 development or misguidance in the adult striatonigral pathway (Chauvet et al., 2007; Ehrman et al., 2013), but
334 these phenotypes were not detected in our study. Instead, we also observed irregular projection patterns near the
335 Gp in *Plxnd1*-knockout mice at P5 but not at P30 (Figures 8D, 8F and S8H), similar to those seen in *Mtss1*-
336 knockout mice. Moreover, *Sema3e*-knockout at P5 showed a few axonal bundles deviated from their typical
337 trajectories (Figures S10F and S10G). These results demonstrate that Sema3E-Plexin-D1 signaling, probably in
338 concert with Mtss1 molecules, is specifically involved in the proper guidance of descending striatonigral
339 projections. Collectively, our results confirm that Sema3E-Plexin-D1 signaling activates Mtss1 action, through
340 which striatonigral neurons are extended and steered through the proper route to the target destination (Figure 8J).

341 Finally, since Sema3E-Plexin-D1 is well known to regulate both neural and vascular development (Oh
342 and Gu, 2013a), we wondered whether Mtss1 also plays a role in the vasculature as a downstream player of the
343 common guidance cue. Although it was expressed in neuronal cells, Mtss1 was not detected in vascular endothelial
344 cells expressing Plexin-D1 during development (Figure S11A). In addition, *Mtss1*-knockout mice did not result
345 in an obvious intersomatic vasculature defect, which is a typical phenotype observed in *Sema3e* or *Plxnd1* mutants
346 (Burk et al., 2017; Gu et al., 2005) (Figure S11B). Interestingly, Mtss1 was highly expressed in the two different
347 types of cultured endothelial cells but was not controlled by Sema3E-Plexin-D1 signaling (Figure S11C). These

348 results provide evidence that the activation of Mtss1 by the Sema3E-Plexin-D1 signaling pathway and its function

349 in neurons could be selective and distinct.

Discussion

There are two main aspects of the traditional axon guidance concept: attractive cue-guided axon growth and repulsive cue-guided axon growth. In these processes, the axon terminals are constantly facing both types of signals *en route* to their destination. In the present study, we show that repulsive guidance cues, namely, Sema3E-Plexin-D1 pairs, induce a dual-functioning facilitator, Mtss1, through which navigating axons ensure incessant extension to their target tissues while exhibiting sensitivity and subsequent steering in response to repulsive signals. In our model (Figure S12), Plexin-D1 on the cell body of direct-pathway MSNs in the striatum receives its specific ligand, Sema3E, through the thalamostriatal projection at the late embryonic stage and induces a unique pool of regulatory factors, including Mtss1. Mtss1 then generates axonal projections to targets in the substantia nigra while enabling Plexin-D1 to transport along axons. In the growth cones, Mtss1 promotes membrane curvature to form a protruding filopodium, and Plexin-D1 is positioned on the cell surface to sense the external repulsive guidance signals from Sema3E. Currently, it is not clear whether Plexin-D1 and Mtss1 are present as a complex at the membrane surface of the growth cone, but Mtss1 does not seem to directly affect the repulsive signaling activation of Sema3E-Plexin-D1. In this way, Mtss1 provides an efficient transport system for its own activator during striatonigral axon growth and potentiates the repulsive guidance cue.

Gene expression by axon guidance signaling

Although many studies have reported the identification of proteins locally synthesized in the axon terminal (Jung et al., 2012), most proteins required for growth cone behavior are generated in and delivered from the soma. Because of the diverse roles of guidance molecules, such as driving neuronal cell migration, cell death, and axonal regeneration, as well as in traditional axonal navigation in the nervous system (Kolodkin and Tessier-Lavigne, 2011), guidance signaling is generally thought to be involved in the activation of a gene expression program in the nucleus. However, few studies have examined gene expression changes induced by guidance signaling at the level of transcriptional regulation, and the most definitive results have been obtained in the *Drosophila* model. (Russell and Bashaw, 2018). A well-described example is the Frazzled (Fra) receptor in the regulation of midline axon crossing in *Drosophila*, where the truncated intracellular domain of Fra is generated by gamma-secretase and enters the nucleus to activate transcription of the *commissureless (comm)* gene (Neuhaus-Follini and Bashaw, 2015). In a rodent model, microarray analysis of the Robo mutant revealed hundreds of DEGs that may be related

377 to the dynamics of neuronal progenitors in the developing cortex (Yeh et al., 2014). Another example is Eph-
378 Ephrin signaling in neural progenitor cells, where Ephrin-B1 reverse signaling downregulates miR-124 expression
379 to inhibit neurogenesis as a posttranscriptional repressor (Arvanitis et al., 2010).

380 Through a bulk RNA-seq analysis, we showed that Sema3E-Plexin-D1 signaling changed the expression
381 of specific genes, including Mtss1, required for the precise axon guidance of striatonigral neurons. Since ablation
382 of Plexin-D1 expression results in the ectopic formation of thalamostriatal synapses on the MSN cell body as well
383 as on dendrites (Ding et al., 2012), it is likely that Plexin-D1 is expressed in the soma of MSNs and is capable of
384 transmitting gene expression signals. Although Sema3E-Plexin-D1 signaling regulated the expression of a set of
385 genes in the present study, the precise signaling cascade that extends into the nucleus is still not completely
386 understood. Nevertheless, we cannot dismiss the possibility that Mtss1 expression activation through Sema3E-
387 Plexin-D1 signaling may be subject to post-transcriptional or translational regulatory mechanisms. Thus, to
388 uncover the molecular mechanism through which these guidance molecules mediate specific gene expression or
389 ensure stability, comprehensive studies on gene regulation in a suitable homogenous cellular model are necessary.
390 A growing body of evidence demonstrates that diverse extracellular stimuli induce mechanotransduction through
391 dynamic changes in the actin and microtubule cytoskeletal networks, which depend on Rho family proteins to
392 cascade signals in the cytosol and nucleus to activate gene expression (Dupont and Wickström, 2022; Giehl et al.,
393 2015; Miralles et al., 2003; Percipalle and Visa, 2006; Samarakoon et al., 2010). Previously, Sema3E-Plexin-D1
394 signaling was shown to modulate such cytoskeletal rearrangement through the PI3K/Akt pathway in regulating
395 endothelial cell mobility, axonal growth, and growth cone collapse (Aghajanian et al., 2014; Bellon et al., 2010;
396 Burk et al., 2017). Likewise, we found that disturbance of Akt signaling reduced Mtss1 expression in young
397 cultured MSNs, suggesting that activation of Sema3E-Plexin-D1 signaling induces specific molecule expression
398 through similar Akt-mediated actin dynamics.

399 Despite the fact that Mtss1 is a downstream molecule under Sema3E-Plexin-D1 signaling, it is still
400 puzzling how Mtss1 expression is specifically and selectively regulated during striatonigral pathfinding. Since
401 Mtss1 expression did not appear to be affected by *Plxnd1*-knockout at early embryonic stages and some level of
402 Mtss1 persisted in cultured neurons lacking *Sema3e* or *Plxnd1*, we cannot exclude the possibility that other
403 pathways activate Mtss1 expression. Nevertheless, it is certain that Mtss1 expression is under Sema3E-Plexin-D1
404 signaling activation during striatonigral projection and that, when axons reach their destination at P7, Mtss1

405 expression is downregulated. Such concurrence of Mtss1 downregulation and axonal projection leads us to
406 speculate that target-derived factor-driven retrograde signaling may be involved in this gene regulation
407 (Harrington and Ginty, 2013), and elucidating the relevant mechanism may be an interesting objective for future
408 study. Furthermore, it is noteworthy that levels of both Plexin-D1 and Mtss1 were exclusively upregulated during
409 the late gestation to early postnatal period, followed by an abrupt downregulation. Therefore, it is plausible that
410 the activation of Mtss1 relies on the reinforcement of Plexin-D1 signaling. During angiogenic sprouting, the
411 expression of Plexin-D1 in endothelial cells is controlled by VEGF signaling (Kim et al., 2022; Yu et al., 2022).
412 However, the upstream pathway responsible for Plexin-D1 expression in neurons and the precise regulation of
413 signaling strength in this context is still uncertain.

414 **Trafficking of Plexin-D1-Mtss1 in striatonigral neurons**

415 Another intriguing finding in our study is that Plexin-D1-containing vesicles undergo both anterograde and
416 retrograde movement along neurites in cultured direct-pathway MSNs. Until now, neurotrophin or semaphorin
417 3A-mediated retrograde trafficking has been extensively studied due to its crucial role in controlling the growth
418 of axons and dendrites, promoting neuronal survival, and facilitating synaptogenesis within the peripheral nervous
419 system. Additionally, finely regulated anterograde transport is essential for replenishing receptors on the growth
420 cone surface to ensure the responses of appropriate target-derived guidance signals (Scott-Solomon and Kuruvilla,
421 2018; Yamashita, 2019). We observed that Mtss1 contributes to the Plexin-D1 localization in the growth cone of
422 cultured MSNs and in the terminal region of descending striatonigral projections. Previously, it has been reported
423 that signaling endosomes containing Sema3A/Plexin-A at the axonal growth cones are retrogradely transported to
424 soma. This process facilitates the localization of AMPA receptor GluA2 to the distal dendrites, thereby regulating
425 dendritic development in the cultured hippocampal neurons (Yamashita et al., 2014). Since it is known that Plexin-
426 D1 plays a role in the somatodendritic synaptogenesis of direct-pathway MSNs (Ding et al., 2012), the connection
427 of the retrograde trafficking Plexin-D1-positive vesicles in this process or other developmental mechanisms like
428 retrograde Sema3A signaling in the soma remains to be elucidated.

429 **Axon-specific role of Sema3E-Plexin-D1-Mtss1 in striatonigral neuron**

430 Sema3E-Plexin-D1 signaling is involved in dendritic synapse formation during the postnatal stage as well as
431 traditional axon projection from the embryonic to the postnatal stage in the basal ganglia circuit (Ding et al., 2012).

In addition, since axon projection and synapse formation are sequential events that occur in different cellular compartments during circuit establishment (Kuo and Liu, 2019), Sema3E-Plexin-D1 signaling may play discrete roles within different parts of a neuron, such as the dendrite versus the axon, through a unique subset of molecules. Indeed, our observations that the duration of Mtss1 expression coincided with active striatonigral axon pathfinding, that Mtss1 was significantly expressed on the axonal side, and that axon projection defects were observed after Sema3E-Plexin-D1 signaling disruption suggest that the Sema3E-Plexin-D1-Mtss1 complex appears to mainly regulate axon projection and guidance, at least during striatonigral pathway development. However, the cellular distribution of Mtss1 is somewhat controversial, as its expression is mainly observed on the dendritic side of Purkinje cells and hippocampal neurons, and its knockout shows defective dendritic arborization and spine formation (Galbraith et al., 2018; Saarikangas et al., 2015; Yu et al., 2016), while a study has also shown that Mtss1 is more localized in the axoplasmic compartment of Purkinje cells (Hayn-Leichsenring et al., 2011). In this study, *Mtss1*- knockout did not show clear dendritic changes in MSNs, at least at P5 when an active axon trajectory occurs; however, given the enlarged ventricle and decreased cortical volume phenotype in knockout adults (Minkeviciene et al., 2019), later Mtss1 expression (even at low levels) may affect overall dendritic development. Consistent with this assumption, a previous study reported a slight decrease in dendritic spine density but a slight increase in the number of dendritic crossings without a change in total dendritic length in the direct pathway MSNs of 3- to 4-week-old *Plxnd1*- or *Sema3e*-knockout mice (Ding et al., 2012). Thus, we cannot exclude the possibility that the Sema3E-Plexin-D1-Mtss1 complex modulates MSN dendritic development later than the axonal pathfinding period.

Counterintuitive mechanism of attractive and repulsive guidance by Mtss1

From a traditional guidance point of view, our finding was somewhat unexpected because it was counterintuitive: conventional repulsive guidance cues that mediate growth inhibition induce upregulation of a positive regulator of neurite extension. We revealed that Mtss1 plays a dual role in striatonigral neurons, axon extension by membrane protrusion ability and axon guidance by efficient Plexin-D1 trafficking to the growth cone. Therefore, our findings represent two important discoveries regarding the axon guidance mechanism. First, axon guidance signaling can switch on the specific regulatory program necessary for facilitating its own function, thereby generating the appropriate machinery to accomplish an intrinsic guidance role during neuronal pathfinding. Second, molecules such as Mtss1 coordinate positive and negative growth potentials in the axonal pathfinding

460 route. Axon guidance cues require various auxiliary proteins to perform their programmed functions, in particular,
461 transporting guidance receptors to the growth cone, endocytic sorting, and activating signaling cascades
462 (O'Donnell et al., 2009), but none of the cofactors discovered to date have induced direct expression regulation
463 of the guidance signaling with which it is involved. Previous studies have shown that Sema3E-Plexin-D1 signaling
464 can switch its role from repulsive to attractive by interacting with the coreceptors neuropilin-1 (Npn1) and vascular
465 endothelial growth factor receptor type 2 (VEGFR2) in subiculum neurons (Bellon et al., 2010; Chauvet et al.,
466 2007). This mechanism is not applicable to developing striatonigral MSNs because the Npn1 receptor is not
467 expressed in early postnatal striatal neurons (Ding et al., 2012). Instead, striatonigral neurons seem to adopt a new
468 strategy, such as activating their own attractive driver to promote axonal growth. From a phenotypic perspective,
469 it is also plausible that the positive or negative guidance roles of Mtss1 may be interdependent. Striatonigral
470 extension defects could potentially lead to inadequate responses to Sema3E signals during pathfinding,
471 consequently resulting in misguided projections. Similarly, guidance defects may disrupt normal signaling
472 processes within the growth cone, thereby transmitting incorrect information for the replenishment of Plexin-D1
473 to the soma. This erroneous signaling could weaken Mtss1 expression and normal trafficking, ultimately leading
474 to axonal growth defects.

475 **Diverse roles of BAR domain proteins in the axon guidance signaling pathway**

476 Mtss1 promotes membrane curvature through the I-BAR domain and induces the redistribution of lipids in the
477 membrane, thereby increasing the local phosphatidylinositol 4,5-bisphosphate (PIP_2) level at the negatively
478 curved membrane. The elevation of local PIP_2 levels leads to membrane binding of the I-BAR domain via
479 electrostatic interactions (Lin et al., 2018). Interestingly, Sema3E binding to Plexin-D1 elevates PIP_2 locally to
480 activate Arf6, resulting in rapid focal adhesion disassembly (Sakurai et al., 2011). Since Mtss1 I-BAR can interact
481 with Plexin-D1 at the curved membrane, the local increase in PIP_2 in the curved membrane region may trigger
482 signaling cascades. Although BAR-domain proteins play pivotal roles in membrane dynamics, a direct association
483 between BAR-domain proteins and axon guidance receptors has not been extensively studied, and functional
484 relevance *in vivo* is unclear. One example is the srGAP2 protein, which has been studied and shown to bind
485 directly with the SH3 domain of the Robo1 guidance protein in cooperation with the F-BAR and RhoGAP domains
486 (Guez-Haddad et al., 2015). Interestingly, in endothelial cells, Plexin-D1 forms a complex with SH3BP1, another
487 small GTPase protein containing the N-BAR domain (Tata et al., 2014). Similar to the effect of Mtss1 and Plexin-

488 D1 complex formation via the I-BAR domain, SH3BP1 colocalized with Plexin-D1 at lamellipodia in a complex
489 formed via the N-BAR domain and mediates Sema3E-induced cell collapse through Rac1 activity regulation.
490 However, in contrast to the effect of the Mtss1 mutant lacking the I-BAR domain, which failed to change the cell
491 morphology, SH3BP1 lacking N-BAR led to cell collapse. Moreover, Sema3E binding to Plexin-D1 caused
492 SH3BP1 to be released from the complex, whereas Sema3E did not interfere with the Plexin-D1-Mtss1 complex.
493 In addition, the presence of Mtss1 had no effect on the endocytosis of Plexin-D1 by Sema3E or on the ability of
494 Sema3E to bind to Plexin-D1. Hence, it is plausible that Mtss1 plays a role as a facilitator of Plexin-D1 trafficking
495 rather than as a direct downstream signaling transducer such as SH3BP1. Because of the diverse roles played by
496 Sema3E-Plexin-D1 across cell types, the effect of signaling induced by this guidance cue may be determined by
497 distinct downstream molecules that share structural similarities in a relevant biological context. Another intriguing
498 finding is the specific complex formation between Plexin-D1 and Mtss1 in the present study. Plexin-D1 did not
499 form a complex with other BAR-domain-containing proteins, srGAP2 and IRSP53, known to have a role in
500 neurons. While we did not conduct an extensive examination, it is noteworthy that at least two other Plexin
501 proteins were unable to form a complex with Mtss1. Therefore, it would be interesting to explore the structural
502 characteristics underlying these interactions.

503 **Variable axon projection defects in direct pathway MSNs mediated by Sema3E-Plexin-D1 signaling**

504 To modulate movement information conveyed through basal ganglia circuitry, two distinct types of striatal MSNs
505 send axonal projections to different targets: a direct-pathway MSN expresses the dopamine D1 receptor to promote
506 movement, and an indirect-pathway MSN expresses the dopamine D2 receptor to inhibit movement (Kreitzer and
507 Malenka, 2008; Surmeier et al., 2007). Because of these unique functional and anatomical features, decoding the
508 distinct molecular properties of the two types of MSNs and the regulatory mechanisms involved in circuitry
509 formation is important. A few previous transcriptome analyses have been performed with juvenile and adult mouse
510 brains (Heiman et al., 2008; Kronman et al., 2019; Lobo et al., 2006), but an understanding of the molecular
511 repertoire of each MSN during development is very limited. In the present study, Mtss1 was identified as a
512 selective molecule expressed in striatonigral projection neurons mediated by Sema3E-Plexin-D1 signaling, but its
513 expression is limited to only the early striatonigral projection period; therefore, the previous transcriptome
514 database in adults may have failed to identify Mtss1 as a specific marker molecule in direct-pathway MSNs.

515 In this study, Mtss1 expression was found to be relatively high during the perinatal period and then was
516 dramatically downregulated by P7, by which time striatonigral projection has been completed (Morello et al.,
517 2015). Consistent with a previous study showing that Plexin-D1-positive cells in the striatum were first detected
518 on E14.5 (Zwaag et al., 2002), we found that its expression increased in the early postnatal stage. During a similar
519 developing window in the striatonigral pathway, Sema3E was predominantly expressed in the GP and rTh/ZI,
520 which is located in the route to the substantia nigra; therefore, the absence of repulsive Sema3E-Plexin-D1
521 signaling resulted in defects in striatonigral projection (Burk et al., 2017; Chauvet et al., 2007; Ehrman et al.,
522 2013). However, we did not find ectopic projections, misguidance defects, or enlarged paths in *Mtss1*- or *Plxnd1*-
523 knockout mice. Nevertheless, we observed fewer projections with aberrantly tangled patterns. These discrepancies
524 may be explained by the following observations. First, because we used a genetic model to selectively label the
525 striatonigral projections, we could detect abnormal phenotypes at a better specific resolution. Second, we noticed
526 a certain degree of developmental retardation in the *Mtss1*- or *Plxnd1*-knockout neonates, even among those in
527 the same litter; therefore, we strictly selected samples on the basis of body weight. However, despite the low
528 striatonigral projection formation rate in the *Mtss1*-, *Plxnd1*- or *Sema3e*-knockout mice, the adult mice showed a
529 normal overall range of projection boundary size and width, suggesting that a decrease in repulsive signals in the
530 mutants may have widened the descending projections. Third, the mouse genetic background may have led to the
531 observed phenotypic discrepancies. We previously observed that certain vascular phenotypes were more evident
532 in *Sema3e*-knockout mice with a 129SVE background than in those with a C57BL/6 background(Oh and Gu,
533 2013b), implying that relatively minor defects may vary depending on the genetic background.

534 Although Sema3E-Plexin-D1 has a similar mechanism of action as a common guidance cue in the
535 nervous and vascular systems, it also exhibits completely different behavior in each system (Oh and Gu, 2013a).
536 For example, the Plexin-D1-Npn1-VEGFR2 complex transmits an attractive signal upon Sema3E binding in
537 specific neurons (Bellon et al., 2010), but endothelial cells still respond negatively to Sema3E despite the presence
538 of all three receptors (Oh and Gu, 2013b). Interestingly, Sema3E-Plexin-D1 utilizes Akt-mediated cytoskeletal
539 dynamics for its signaling cascade in both neuronal and endothelial cells (Burk et al., 2017; Moriya et al., 2010),
540 and various auxiliary molecules, such as SH3BP1, Arf6, and GIPC1, have been revealed in each cell (Burk et al.,
541 2017; Sakurai et al., 2010; Tata et al., 2014). However, only a few of these cofactors have shown a common
542 molecular mechanism and expression by exchanging cells with each other, suggesting that Sema3E-Plexin-D1

signaling requires unique factors to perform different functions. Similarly, we identified Mtss1 as a downstream factor of the Sema3E-Plexin-D1 cue, but its function seems to be limited in neurons, at least *in vivo*. Therefore, it is necessary to elucidate whether Sema3E-Plexin-D1 signaling activates a specific pool of regulatory factors required for vascular development and to compare this with the results obtained in neurons, which will help us to understand the underlying mechanism of specific molecule expression by guidance signaling. Furthermore, given the tremendous complexity of wiring in the central nervous system, it will be intriguing to discover new dual-function molecules similar to those in the Sema3E-Plexin-D1-Mtss1 complex that are involved in the formation of other circuits in the future.

551 # Materials and Methods

552 **Mice**

553 *Plxnd1*$^{flox/flox}$ (*Plxnd1*$^{f/f}$) mice (Kim et al., 2011) and *Sema3e*$^{+/-}$ mice (Chauvet et al., 2007) were maintained on a
554 C57BL/6 (#000664, The Jackson Laboratory) background. Nestin-Cre (#003771), Tie2-cre (#008863), and
555 Drd1a-tdTomato (#016204) mice were obtained from The Jackson Laboratory (Bar Harbor, USA) and maintained
556 on the same background. The frozen sperm of *Mtss1*$^{flox/+}$ mice were generously provided by Dr. Mineko Kengaku
557 and rederived at the Laboratory Animal Resource Center in the Korea Research Institute of Bioscience and
558 Biotechnology (Cheongju, Korea). All protocols for animal experiments were approved by the Institutional
559 Animal Care and Use Committee of Korea Brain Research Institute (IACUC-18-00008, 20-00012). All
560 experiments were performed according to the National Institutes of Health Guide for the Care and Use of
561 Laboratory Animals and ARRIVE guidelines.

562 **Primary striatal neuron culture**

563 Primary mouse striatal neurons were isolated from neonatal pups as described in a previous report with some
564 modifications (Penrod et al., 2011). Whole striatal tissues including the globus pallidus were digested with 20
565 units/ml papain (LS003124, Worthington, Lakewood USA) diluted in dissection solution (5 mM $MgCl_2$ and 5
566 mM HEPES in 1× Hanks' balanced salt solution, pH 7.2) followed by multiple washes in inhibition solution (0.1%
567 BSA and 0.1% Type II-O trypsin inhibitor diluted in dissection solution). The tissues were resuspended in neuronal
568 plating medium (1 mM pyruvic acid, 0.6% glucose, and 10% heat-inactivated horse serum in Minimum Essential
569 Medium with Earle's Salts) and triturated fifty times with a fire-polished Pasteur pipette. The dissociated neurons
570 were centrifuged at 1000 ×g for 5 min and resuspended in fresh neuronal plating media for cell counting. Then,
571 the cells were plated on coverslips or culture dishes coated with 50 μg/ml poly-D-lysine (P6407, Sigma) and
572 1 μg/ml laminin (354232, Corning) at a density of 3×10^4 cells/cm^2. After 4 h of incubation at 37°C, the plating
573 media were replaced with neuronal growth media (0.5 mM L-glutamine, B27 supplements in neurobasal medium
574 (10888022, Gibco)), and a quarter of the media was replaced with fresh growth media every 3 days until harvest.

575 **Plasmids**

576 A pBK-CMV vector containing VSV-tagged human Plexin-D1 cDNA (Gu et al., 2005) was recloned into a pCAG
577 vector (pCAG-vsv-hPlexin-D1), and a Plexin-D1 construct lacking an intracellular domain (amino acids deleted:
578 1,299–1,925) was generated by PCR-based mutagenesis (pCAG-vsv-hPlexin-D1ΔICD). To generate the pCAG-
579 hPlexin-D1-GFP fusion construct, a GFP gene fragment was inserted at the C-terminus of the pCAG-vsv-hPlexin-
580 D1 plasmid. pAPtag-5-Sema3E vectors were reported previously (Chauvet et al., 2007), and the mouse Plexin-
581 D1 extracellular domain (amino acids: 1–1,269) was amplified from mouse Plexin-D1 cDNA and directly cloned
582 into a pAPtag-5 vector (pAPtag5-mPlexin-D1-ECD). The human full-length Mtss1 expression construct was
583 purchased from Origene (pCMV6-hMtss1, Cat# RC218273, USA), and Myc-tagged Mtss1 deletion constructs
584 (Mtss1ΔI-BAR [amino acids deleted: 1–250], Mtss1ΔWH2 [amino acids deleted: 714–745], and Mtss1-I-BAR
585 [amino acids: 1–250]) were generated by PCR-based mutagenesis. To generate full-length mouse Flag-Plexin-D1,
586 SH3BP1-HA, and HA-srGAp2, each gene was isolated directly from the mouse brain cDNA library and cloned
587 into pCAG vector with the tagging fragment. The mouse vsv-plexin-B2, mouse vsv-plexin-B3 and human pECE-
588 M2-BAIAP2 (IRSP53-Flag) were purchased from Addgene (#68038, #68039, #31656, USA).

589 **RNA sequencing analysis**

590 RNA sequencing (RNA-seq) library preparation and sequencing were conducted at Ebiogen (Seoul, South Korea).
591 Libraries were constructed using a NEBNext Ultra Directional RNA-seq Kit customized with mouse-specific
592 oligonucleotides for rRNA removal. Directional mRNA-seq was conducted using the paired-end, 6 Gb read option
593 of the Illumina HiSeq X10 system.

594 **Bioinformatic analysis for RNA-seq**

595 The entire analysis pipeline of RNA-seq was coded using R software (ver. 3.6), which was controlled by
596 systemPipeR (ver.1.18.2). The raw sequence reads were trimmed for adaptor sequences and masked for low-
597 quality sequences using systemPipeR. Transcript quantification of the RNA-seq reads was performed with
598 GenomicAlignments (ver.1.20.1) using reads aligned with the *Mus musculus* transcriptome annotation using
599 Rsubread (ver. 1.24.6). The fragments per kilobase of transcript per million mapped reads (FPKM) values were
600 calculated using the fpkm function of DESeq2 (ver. 1.24.0) and were processed using the robust median ratio
601 method. Transcript reads were normalized by the voom function of Limma (ver. 3.40.6). To determine if a
602 transcript was differentially expressed (DE), EdgeR (ver. 3.26.7) calculated the results based on the normalized

603 counts from entire sequence alignments. Significantly DE transcripts with a fold change greater than the raw
604 FPKM value (> 2) and adjusted p value (< 0.01) in all experimental comparisons were selected and used for
605 further analysis. Gene annotations were added with an online database using Ensembl biomaRt (ver. 2.40.4), and
606 visualization was performed using the R base code and gplots package (ver. 3.0.1.1). For DEG sets, hierarchical
607 cluster analysis was performed using complete linkage and Euclidean distance to measure similarity. All data
608 analysis and the visualization of DEGs were conducted using R version 3.0.2 (www.r-project.org).

609 **Quantitative reverse transcription PCR (qRT–PCR)**

610 Total RNA was extracted from dissected tissue using TRIzol™ (15596026, Thermo). cDNA was synthesized from
611 200 ng of total RNA with a QuantiTect Reverse Transcription Kit (205313, Qiagen). Quantitative PCRs were
612 carried out in triplicate using SYBR Green I Master Mix (S-7563, Roche) on a LightCycler 480 system (Roche).
613 Expression was calculated using the $2^{-\Delta\Delta Ct}$ method with *Gapdh* as a reference. The following primers were used
614 (forward primer and reverse primer, respectively): *Plxnd1*: 5'-CTAGAGATCCAGCGCCGTTT, 5'-
615 GGCACTCGACAGTTGGTACA, *Mtss1*:5'-CCTTTCCCTCATTGCCTGCCT,5'-TCTGAGATGACGGGAACATGCC,
616 and *Gapdh*: 5'-TGACGTGCCGCCTGGAGAAAC, 5'-CCGGCATCGAAGG TGGAAGAG.

617 **Transfection**

618 DNA expression constructs were transfected into COS7 or HEK293T cells by Lipofectamine 2000 (11668019,
619 Invitrogen) in OPTI-MEM (31985-070, Gibco) for 4 h according to the manufacturer's instructions and then
620 replaced with normal culture media until the next procedure. For imaging analysis, 0.5 μg of DNA was transfected
621 into COS7 cells (1×10^4 cells/cm^2) cultured on coverslips in a 12-well plate. For biochemical analysis, 4 μg of
622 DNA was transfected into HEK293T cells (3×10^4 cells/cm^2) cultured on a 10-cm dish. To achieve high transfection
623 efficiency into primary neurons, the nucleofection technique using a Lonza Amaxa Nucleofector was performed
624 following the manufacturer's instructions (Basic Nucleofector Kit for Primary Mammalian Neurons, VAPI-1003).
625 To transfect into neurons, 4 μg of expression constructs were added to at least 1×10^6 isolated neuronal cells for
626 each electroporation, and the transfected cells were plated and cultured as described in the previous section.

627 **Alkaline phosphatase (AP)-conjugated ligand preparation and binding analysis**

628 AP-conjugated Sema3E and Plexin-D1-ECD ligands were generated in HEK293T cells, and ligand binding

629 experiments were performed as described in previous reports (Chauvet et al., 2016, 2007). Briefly, the AP-
630 conjugated expression construct was transfected into cells by Lipofectamine 2000 and cultured overnight in
631 Dulbecco's modified Eagle's medium containing 10% fetal bovine serum (FBS). Then, the medium was replaced
632 with OPTI-MEM and harvested at 5 days posttransfection. The collected conditioned medium was filtered to
633 increase the ligand concentration.

634 To measure the binding ability of AP-Sema3E to the Plexin-D1 receptor, COS7 cells on a six-well plate
635 were transfected with each expression vector and cultured for 24 h. The next day, the cells were washed in HBHA
636 buffer [1× HBSS, 0.5 mg/ml BSA, 0.5% sodium azide, and 20 mM HEPES (pH 7.0)] and incubated with 2 nM
637 AP or AP-Sema3E for 1 h at room temperature. After seven washes in the HBHA buffer, the cells were lysed in
638 1% Triton X-100 and 10 mM of Tris-HCl (pH 8.0), and the supernatant was obtained by centrifugation at 13,000
639 ×g for 10 min. The lysates were heat-inactivated at 65°C for 10 min, and each lysate was used for AP concentration
640 using a BioMate™ 3S spectrophotometer (Thermo Scientific), and the amount of protein was measured by BCA
641 assay.

642 For AP-conjugated ligand binding analysis of tissues, 20-μm-thick cryosections were fixed in cold
643 methanol for 8 min and preincubated in 1× Phosphate-buffered saline (PBS) containing 4 mM $MgCl_2$ and 10%
644 FBS for 1 h. Next, a binding solution (1× PBS–$MgCl_2$ and 20 mM HEPES, pH 7.0) containing 2 nM AP-Sema3E
645 was applied, and sections were incubated for 2 h at room temperature. After five washes in 1× PBS–$MgCl_2$, the
646 sections were briefly soaked in acetone–formaldehyde fixative (60% acetone, 1.1% formaldehyde, and 20 mM
647 HEPES, pH 7.0) and heat-inactivated in 1× PBS at 65°C for 2 h. Next, the sections were incubated in AP buffer
648 (NBT/BCIP tables, 11697471001, Roche) until clear purple precipitation was observed at room temperature. For
649 quantification, three brain sections per animal were analyzed and averaged. For the AP-Sema3E binding analysis
650 of growth cones, MSNs grown for 6 days on glass coverslips were washed in 1× PBS, immediately fixed in cold
651 methanol for 5 min, and blocked in TBS buffer (100 mM TBS, 4 mM $MgCl_2$, 4 mM $CaCl_2$, pH 7.4) with 10% FBS
652 at RT for 1 h. The MSNs were then incubated in 0.5 nM AP-Sema3E ligand diluted in blocking solution at RT for
653 1 h. After five washes in TBS buffer, the MSNs were fixed in acetone/formaldehyde solution, heat-inactivated,
654 and incubated in AP buffer as described above.

655 **AP treatment of HUVECs and HCMEC/D3 cells**

656 HUVECs were purchased from Lonza, and the HCMEC/D3 cell line was obtained from Millipore. The cell culture
657 media and culture conditions used followed the information provided by the respective companies. Cultured
658 HUVECs and HCMEC/D3 cells were treated with 2 nM AP or AP-Sema3E for 24 hr. Then, the cells were lysed
659 and prepared for Western blotting as described below.

660 **Immunoblotting**

661 Brain tissue was collected in Radioimmunoprecipitation assay (RIPA) buffer [50 mM Tris-HCl (pH 8.0), 150 mM
662 NaCl, 1% NP-40, and 1% sodium deoxycholate] with a protease inhibitor cocktail (78444, Thermo Fisher
663 Scientific), and protein amounts were quantified using a BCA protein assay kit (23227, Thermo Fisher Scientific).
664 A total of 40 μg of protein was loaded into each well of a sodium dodecyl sulfate (SDS) polyacrylamide gel, after
665 which it was separated and transferred to a polyvinylidene fluoride membrane (IPVH00010, Merck) at 100 V for
666 90 min. All membranes were blocked in Everyblot blocking buffer (12010020, Bio-Rad) for 1 h and probed
667 overnight with primary antibodies in blocking buffer at 4°C. The primary antibodies included the following: anti-
668 Mtss1 (1:1000, Novus, NBP2-24716), anti-Plexin-D1 (1:1000, AF4160, R&D Systems), anti-β-actin (1:5000,
669 5125S, Cell Signaling), anti-Myc (1:1000, 2276S, Cell Signaling), anti-vsv (1:1000, ab3861, Abcam), anti-
670 Sema3E (1:500, LS-c353198, LSBio), anti-p-AKT (1:1000, 9271, Cell Signaling), and anti-AKT (1:1000, 9272S,
671 Cell Signaling). The membranes were incubated in TBST, and the appropriate horseradish peroxidase (HRP)-
672 conjugated secondary antibodies and bands were developed with enhanced chemiluminescence using Fusion FX7
673 (Vilber, Germany) and then analyzed using ImageJ software.

674 **Immunoprecipitation**

675 HEK293T cells were transfected with Lipofectamine 2000, and after 24 h, they were lysed in a buffer consisting
676 of 100 mM Tris-HCl (pH 7.5), 100 mM EDTA, 150 mM NaCl, and 1% Triton X-100 with freshly added phosphate
677 and protease inhibitors. The cell lysates were centrifuged at 13,000 × g for 10 min at 4°C, and supernatants were
678 incubated with antibodies (1:200) at 4°C overnight. Then, the protein lysates were incubated with magnetic beads
679 for 1 h at 4°C. Next, the beads were washed five times with lysis buffer, and the bound proteins were eluted with
680 a 2× SDS sample buffer by heating the beads at 95°C for 5 min. The samples were then analyzed by SDS–PAGE
681 and Western blotting. The following antibodies were purchased from commercial sources: anti-Myc (1:1000,
682 2276S, Cell Signaling), anti-vsv (1:1000, ab3861, Abcam), anti-Mtss1 (1:1000, NBP2-24716, Novus), anti-

683 Plexin-D1 (1:1000, AF4160, R&D Systems), and anti-β-Actin (1:5000, 5125S, Cell Signaling).

684 **Protein–protein interaction assay**

685 The I-BAR domain of human Mtss1 was purchased from Sino Biological (Cat 13085-H10E). The human Plexin-
686 D1 cytosolic domain was prepared. Briefly, the coding sequence of the human PLXND1 (NM_105103.3)
687 cytosolic domain (amino acid residue 1297~1925; hPLXND1_Cyto) was subcloned into the mammalian
688 expression vector CAGs-MCS EEV (SBI, Palo Alto, CA) in-framed fused with a C-terminal twin strep tag
689 (SAWSHPQFEKGGGSGGGSGGSAWSHPQFEK). HEK293 GnTI$^-$ cells were transfected with the PLXND1
690 expression vector and grown in FreeStyle™ 293 Expression Medium supplemented with 2% (v/v) FBS in a
691 humidified CO_2 incubator (35°C, 5% CO_2) with shaking at 150 rpm for 3 days. Cells were harvested, resuspended
692 in resuspension buffer (500 mM NaCl, 10 mM Tris-HCl, pH 8.0, 5% (v/v) glycerol, 3 mM β-mercaptoethanol,
693 protease inhibitor cocktail (Roche), 0.4 mg/mL DNase I (GOLDBIO)), and disrupted by using a Dounce
694 homogenizer followed by sonication. After the removal of cell debris by centrifugation, the cell lysate was loaded
695 onto preequilibrated Strep-Tactin XT 4Flow resin (IBA Lifesciences GmbH, Germany) and washed with wash
696 buffer (500 mM NaCl, 10 mM Tris-HCl, pH 8.0, 5% (v/v) glycerol, 3 mM β-mercaptoethanol). hPLXND1_Cyto
697 with a twin strep tag was eluted with elution buffer (50 mM biotin, 500 mM NaCl, 10 mM Tris-HCl, pH 8.0, 5%
698 (v/v) glycerol, 3 mM b-mercaptoethanol) and further purified by using size-exclusion chromatography on a size-
699 exclusion column (Superdex 200) equilibrated with FPLC buffer (150 mM NaCl, 20 mM Tris, pH 8.0, 10%
700 glycerol (v/v), 2 mM DTT). To obtain the tag-free hPLXND1_Cyto proteins, the C-terminal twin strep tag was
701 removed by incubating with the 3C protease (Takara Bio, Japan; 1.5 unit/50 mg protein) and ran on a size-
702 exclusion column. To analyze direct binding, Mtss1-I-BAR with Plxind-D1-ICD was mixed in binding buffer (50
703 mM Tris-HCl, 0.1% Triton X-100) and incubated overnight at 4°C. The mixed proteins were then incubated with
704 Ni-NTA beads for 1 h at 4°C. Next, the beads were washed five times with binding buffer, and the bound protein
705 was eluted with 2× SDS sample buffer by heating the beads at 95°C for 5 min. The samples were then analyzed
706 by SDS–PAGE and stained with Coomassie blue solution. After washing with water five times, the stained gels
707 were visualized using a Bio-Rad instrument.

708 **Cell surface biotinylation and endocytosis analysis**

709 Transfected COS7 cells on a 100-mm dish were biotinylated by incubation in 1 mg/ml NHS-SS-Biotin (21331,

710 Thermo Scientific), diluted in 1× PBS containing 1 mM $MgCl_2$ and 0.1 mM $CaCl_2$ (PBS–MC) for 15 min, washed
711 in PBS–MC containing 10 mM glycine at least three times, and then rinsed in ice-cold PBS–MC twice at 4°C.
712 For the negative control, the cells were incubated in stripping buffer (50 mM glutathione, 75 mM NaCl, 10 mM
713 EDTA, 75 mM NaOH, and 1% bovine serum albumin (BSA)) and washed twice in PBS–MC. For the
714 neutralization of glutathione, the cells were incubated in PBS–MC containing 50 mM iodoacetamide (I1149,
715 Sigma) three times. All biotinylated or stripped cells were lysed in ice-cold RIPA buffer [50 mM Tris-HCl (pH
716 8.0), 150 mM NaCl, 1% NP-40, and 1% sodium deoxycholate] with a protease inhibitor cocktail, and 100 μg of
717 protein extracts was incubated in prewashed streptavidin agarose resin (20357, Thermo Scientific) overnight and
718 rotated throughout. Cell extracts were serially washed in bead-washing solution [Solution A: 150 mM NaCl, 50
719 mM Tris-HCl (pH 7.5), and 5 mM EDTA; Solution B: 500 mM NaCl, 50 mM Tris-HCl (pH 7.5), and 5 mM EDTA;
720 Solution C: 500 mM NaCl, 20 mM Tris-HCl (pH 7.5), and 0.2% BSA] followed by another wash in 10 mM Tris-
721 HCl (pH 7.5). The bound biotinylated proteins were recovered by adding 2× sample buffer and boiling extracts
722 for 5 min, and then the supernatants were subjected to western blotting.

723 To analyze endocytic protein levels, cells were incubated for 25 min at 37°C in the presence of prewarmed
724 culture media with 2 nM AP or AP-Sema3E ligands after surface biotinylation. Then, the biotinylated proteins
725 remaining on the cell surface were removed by stripping procedures, and the rest of the experiment was continued
726 as described in the above section. Except for those used in the ligand stimulation process, all reagents were
727 prechilled, and experiments were performed in an ice or cold chamber.

728 **Immunostaining**

729 For immunocytochemistry, cultured cells or neurons on coverslips were fixed in 4% paraformaldehyde (PFA) for
730 5 min and washed several times in PBS. Then, the cells were permeabilized in PBST (PBS containing 0.1% Triton
731 X-100) for 5 min, blocked with 5% horse serum in PBST for 60 min at room temperature, and incubated with
732 primary antibodies diluted in blocking solution overnight at 4°C. The next day, the samples were washed with
733 PBST three times and incubated for 1 h with Alexa Fluor 488-, 594-, or 647-conjugated secondary antibodies
734 (1:1000, Thermo). To enable visualization of the F-actin, Alexa Fluor-conjugated phalloidin (1:50, Thermo) was
735 added during the secondary antibody incubation. After being washed again with PBST, the samples were mounted
736 with Prolong Diamond antifade solution containing DAPI (P36962, Thermo). Image processing was performed

using ImageJ or Adobe Photoshop (Adobe Photoshop CC2019) under identical settings. All other immunostaining procedures were the same as those described above. The following primary antibodies for immunocytochemistry were used: anti-vsv (1:1000, ab3861, Abcam), anti-Myc (1:1000, 2276S, Cell Signaling), phalloidin Alexa Fluor 488 (1:50, A12379, Thermo), phalloidin Alexa Fluor 647 (1:100, A22287, Thermo), anti-RFP (1:1000, ab62341, Abcam), anti-RFP (1:1000, MA5-15257, Thermo), anti-Tau (1:500, sc-1995, Santa Cruz), and anti-alpha-tubulin (1:1000, T5168, Sigma). Images were collected using a Nikon Eclipse Ti-U microscope (Nikon, Japan), Leica TCS SP8 Confocal Microscope (Leica, Germany), or Structured Illumination Microscope (Nikon, Japan).

For immunohistochemistry with tissue samples, brains were fixed in 4% PFA overnight and equilibrated with 20% sucrose in 1× PBS. Mouse brain sections were cut into 20-μm slices on a cryostat (Leica Microsystems Inc., Buffalo Grove, IL, USA). Mouse brain sections were permeabilized in PBST (PBS containing 0.2% Triton X-100) for 10 min, blocked with 2% BSA and 5% normal donkey serum in PBST for 60 min at room temperature, and then incubated in primary antibodies diluted with 2% BSA in PBST overnight at 4°C. The following primary antibodies were used: anti-Mtss1 (1:1000, NBP2-24716, Novus), anti-RFP (1:1000, MA5-15257, Thermo), anti-neurofilament (1:500, 2H3, Hybridoma Bank), anti-CD31 (1:500, 553370, BD Biosciences), and anti-cleaved caspase 3 (1:1000, 9661, Cell Signaling). After being washed with PBS/0.2% Tween 20 (PBST) three times, sections were incubated for 1 h with Alexa Fluor 488-, 594-, or 647-conjugated secondary antibodies (1:1000, Invitrogen). For negative controls, brain sections were stained with secondary antibodies only. Image processing was performed using ImageJ or Adobe Photoshop (Adobe Photoshop CC2019).

Growth cone collapse and neurite length analysis

For the growth cone collapse assay, striatal neurons at DIV3 were incubated with 5 nM AP or AP-Sema3E 3 for 25 min. For the preservation of the growth cone structure, 8% PFA was directly added to cultured neurons to equalize at 4% PFA for 10 min at 37°C, and subsequently, another 5-min round of 4% PFA fixation was performed on ice before the immunostaining procedure. Growth cone images were collected from tdT-positive neurons using a Structured Illumination Microscope (SIM, Nikon), and collapsed growth cones were determined blindly. Growth cones with broad lamellipodia were considered intact, whereas those with a few filopodia lacking lamellipodia were defined as collapsed according to previous guidelines (Oh and Gu, 2013b).

For measurement of neurite length, dissociated striatal neurons were cultured in the presence of 5 nM

764 ligands and immunostained as described in the above section. The neurons were imaged by a fluorescence
765 microscope (Nikon ECLIPSE Ti-U), and the longest neurite length from tdT-positive neurons was determined
766 using ImageJ software. The neurites that formed a network with another neurite and those whose longest
767 protrusions were smaller than twice the cell body diameter were excluded from measurement according to
768 previous guidelines (Chauvet et al., 2016). For quantification of the degree of colocalization, Pearson's correlation
769 coefficients were calculated using the manufacturer's software (Nikon, NIS-Elements software).

770 ***In situ* hybridization (ISH)**

771 ISH was performed under RNase-free conditions as described in a previous study (Ding et al., 2012). After fixation
772 in 4% PFA for 20 min, 20-μm-thick cryosections were preincubated in hybridization buffer (5× Denhardt's
773 solution, 5× saline sodium citrate (SSC), 50% formamide, 0.25 mg/ml Baker yeast tRNA, and 0.2 mg/ml salmon
774 sperm DNA) for 2 h at room temperature. Next, the sections were hybridized in the same buffer containing the
775 indicated digoxigenin-conjugated riboprobe at 60°C overnight. After hybridization, the sections were washed in
776 a serial SSC buffer and formamide solution and then preincubated in buffer 1 (100 mM Tris-HCl, pH 7.5, 150
777 mM NaCl) with a 1% blocking reagent (Roche) for 1 h at room temperature. Next, the sections were incubated
778 with sheep anti-digoxigenin-alkaline phosphatase (AP) antibody (1:3000, Roche) for 90 min at room temperature,
779 washed in buffer 1, and then incubated in AP buffer (100 mM Tris–HCl, pH 9.5; 100 mM NaCl; and 5 mM $MgCl_2$)
780 containing 4-nitro blue tetrazolium chloride (NBT, Roche), 5-bromo-4-chloro-3-indolyl-phosphate (BCIP, Roche),
781 and levamisole (1359302, Sigma) until purple precipitates were observed. After mounting them with coverslips,
782 the samples were analyzed using confocal laser-scanning microscopy with a Nikon Eclipse Ti-U Microscope or
783 Leica TCS SP8 Confocal Microscope. For double fluorescence ISH, the tyramide signal amplification method
784 with minor modifications was used according to the manufacturer's instructions (NEL753001KT, PerkinElmer).
785 The following antisense riboprobes were used: *Plxnd1* (Ding et al., 2012), *Sema3e* (Gu et al., 2005), and *Mtss1*
786 (Allen Brain Atlas, Probe RP_040604_01_B06).

787 **Live cell imaging**

788 Isolated striatal neurons were transfected with an expression plasmid, as described in the above section, and were
789 plated onto a 35-mm confocal dish (211350, SPL Life Sciences) at a density of 1×10^4 cells/cm^2. At DIV6, time-
790 lapse imaging was performed in a stage-top cell incubator (37 °C with 5% CO_2 supplied). Images were acquired

791 at 1-second intervals for 3 minutes using a Nikon A1-Rsi confocal microscope. To quantify Plexin-D1-GFP
792 trafficking, time-lapse images were analyzed using Particle Tracking Recipe in AIVIA microscopy image analysis
793 software (Aivia lnc.).

794 **Golgi staining and dendrite analysis**

795 Golgi staining was conducted according to the manufacturer's protocol (FD Rapid GolgiStain Kit (PK401A, FD
796 NeuroTechnologies, Inc.)). In brief, P5 mouse brains were immersed in a staining solution for 2 weeks before
797 being transferred to a wash solution for 4 days. Then, 100-μm slices were obtained using a vibratome and collected
798 on gelatin-coated slides. During the staining process, the slices were washed twice with distilled water for 4 min,
799 immersed in the staining solution for 10 min, and then washed again. The slices were then dehydrated, cleared in
800 xylene three times for 4 min, mounted with Eukitt® Quick-hardening mounting medium (Sigma, 03989), and
801 imaged by light microscopy with Z-stack. Image processing was performed using Neurolucida360 software in 3D
802 analysis.

803 **Whole embryo immunostaining and clearance**

804 Mouse embryos were fixed in 4% PFA overnight at 4°C and washed three times in PBS. Then, the embryos were
805 permeabilized in PBST (PBS containing 1% Triton X-100) for 2 h at room temperature (RT), incubated in blocking
806 solution (75% PBST, 20% dimethyl sulfoxide, 5% normal goat serum) for 3 h at RT, and incubated in anti-CD31
807 (1:500, company name) diluted in the blocking solution at RT. After three days, the embryos were washed with
808 PBST for 8 h and incubated with Alexa Fluor 488-conjugated secondary antibody (1:500, Thermo) for 2 days at
809 RT. After washing again with PBST for 8 h, the embryos were cleared with ethyl cinnamate (ECi; cat#112372,
810 Sigma) according to a previous protocol (Klingberg et al., 2017). Briefly, the embryos were subjected to serial
811 dehydration with ethanol (EtOH) (30%, 50%, and 70% EtOH, pH 9.0 with 2% Tween 20, followed by twice 100%
812 EtOH). The solutions were changed every 12 h and incubated at 4°C. The samples were transferred to ECi and
813 incubated at RT with gentle shaking until they became transparent, and cleared samples were stored in ECi at RT
814 until imaging. All clearing procedures were performed in the dark. A Dragonfly 502w (Andor Technology) was
815 used for imaging, and Imaris x64 9.6.1 (Bitplane) was used for image reconstruction.

816 **DiI injection and imaging**

817 For the tracing of the neural projection, small crystals of DiI (1.1-dioctadecyl-3,3,3,3-tetramethyl-
818 indocarbocyanine perchlorate, Sigma) were inserted into the thalamus of an E16.5 mouse brain fixed in 4% PFA
819 overnight and sealed with 2% agarose melt in 1× PBS. Then, the brain was incubated in 4% PFA at 37°C for 2
820 weeks and divided into 100-μm thick sections by a vibratome (Leica VT200S). Serial brain slices were
821 immediately collected, and DiI-stained sections were imaged by a fluorescence microscope (Nikon Eclipse Ti-U).
822 To sparsely label the striatonigral projection, DiI crystals were injected into the dorsal striatum of P5 mouse brain
823 and incubated for a month or so under the same conditions as described above. Afterward, the tissue was sectioned
824 into 100-μm thick slices using a vibratome (Leica VT200S). Z-stack images were obtained by using Leica TCS
825 SP8 Confocal Microscope, and the 3-D images were reconstructed utilizing Leica Application Suite X, an image
826 analysis software.

827 **Striatonigral projection analysis**

828 For the analysis of striatonigral projections, P5 or P30 brains from wild-type (*Drd1a-tdT; Mtss1*$^{f/f}$), *Mtss1* cKO
829 (*Drd1a-tdT; Nes-cre; Mtss1*$^{f/f}$), or *Plxnd1* cKO (*Drd1a-tdT; Nes-cre; Plxnd1*$^{f/f}$) mice were fixed in 4% PFA
830 overnight and embedded in a 4% agarose block melt in PBS after being washed with PBS three times. Then, the
831 areas of interest in the brain were divided into 100-μm-thick sections by a vibratome (Leica VT200S). Serial brain
832 slices were immediately collected and mounted with Prolong Diamond antifade solution containing DAPI
833 (P36962, Thermo). The sections were imaged with a fluorescence microscope (Nikon Eclipse Ti-U). To analyze
834 the guidance phenotype in the striatonigral projections, we quantified the number of axon bundles intersecting
835 with others between the globus pallidus (Gp) and the entopeduncular nucleus (EP). Since some mutants within
836 the same litter occasionally displayed significant developmental delays, we selectively chose samples from mutant
837 littermates with ± 5% body weight variance for a reliable phenotypic assessment.

838 **Quantification and Statistical analysis**

839 The estimate of variance was determined by the standard error of the mean (SEM), and statistical significance
840 was set at $P<0.05$. All data were tested with a Gaussian distribution using the Shapiro–Wilk test before statistical
841 analysis. Pairwise comparisons were performed using the two-tailed Student's *t* test or Mann–Whitney test, and
842 multiple-group analyses were conducted with one-way or two-way ANOVA with Tukey's or Bonferroni's multiple
843 comparisons test or Kruskal–Wallis test with Dunn's multiple comparisons test. For the growth cone collapse

assay, the $\chi 2$ test was used as previously reported (Burk et al., 2017). For the quantification of colocalization, the images were analyzed using the Jacop plugin in ImageJ (National Institutes of Health, Bethesda, MD). Statistical data on colocalization were obtained using Costes' randomization based on the colocalization module, as previously described (BOLTE and CORDELIÈRES, 2006). Statistical analyses were performed with Prism 9 (GraphPad Software). At least three pairs of mice were used per experiment for all histological analyses. For the quantification of image data, at least three brain sections per animal were collected and analyzed. All data analyses were performed by an investigator blinded to the groups. No statistical methods were used to predetermine sample sizes, but our sample sizes were similar to those generally employed in the field.

Data and code availability

The accession number for the RNA-Seq data reported in the present study is GSE196558.

Acknowledgments

We thank Drs. Ayal Ben-Zvi, Soonmoon Yoo, and Chenghua Gu for reading the manuscript and providing critical advice; Dr. Chenghua Gu for providing *Sema3e* and *Plxnd1-flox* mice; Drs. Mineko Kengaku and Masayoshi Mishina for providing *Mtss1-flox* mice; Juhyun Lee for helping with quantification; the Advanced Neural Imaging Center in KBRI for image analysis**.** This research was supported by the KBRI basic research program of the Korea Brain Research Institute funded by the Ministry of Science and ICT (KBRI 23-BR-01-02), the National Research Foundation (NRF) funded by the Korean government (NRF-2014R1A1A2058234), the Bio & Medical Technology Development Program of the NRF & funded by the Korean government (MSIT) (NRF-2020M3E5D9079766 and NRF-2022M3E5E8017701) to WO, and the Young Researcher Program of the National Research Foundation (NRF) funded by the Korean government (MSIT) (2020R1C1C1010509) to NK.

Authors' contributions

WO conceived and designed the project. WO, NK, YL, RY, AS, HK, JJ, and JL conducted experiments and acquired data. MK and JK performed RNA-seq and analyzed data. NK, JK, HL, and WO wrote the manuscript.

Declaration of interests: The authors declare that they have no competing interests

References

Ade KK, Wan Y, Chen M, Gloss B, Calakos N. 2011. An Improved BAC Transgenic Fluorescent Reporter Line for Sensitive and Specific Identification of Striatonigral Medium Spiny Neurons. *Front Syst Neurosci* **5**:32. doi:10.3389/fnsys.2011.00032

Aghajanian H, Choi C, Ho VC, Gupta M, Singh MK, Epstein JA. 2014. Semaphorin 3d and Semaphorin 3e Direct Endothelial Motility through Distinct Molecular Signaling Pathways*. *J Biol Chem* **289**:17971–17979. doi:10.1074/jbc.m113.544833

Arvanitis DN, Jungas T, Behar A, Davy A. 2010. Ephrin-B1 Reverse Signaling Controls a Posttranscriptional Feedback Mechanism via miR-124. *Mol Cell Biol* **30**:2508–2517. doi:10.1128/mcb.01620-09

Bai G, Chivatakarn O, Bonanomi D, Lettieri K, Franco L, Xia C, Stein E, Ma L, Lewcock JW, Pfaff SL. 2011. Presenilin-Dependent Receptor Processing Is Required for Axon Guidance. *Cell* **144**:106–118. doi:10.1016/j.cell.2010.11.053

Bellon A, Luchino J, Haigh K, Rougon G, Haigh J, Chauvet S, Mann F. 2010. VEGFR2 (KDR/Flk1) Signaling Mediates Axon Growth in Response to Semaphorin 3E in the Developing Brain. *Neuron* **66**:205–219. doi:10.1016/j.neuron.2010.04.006

BOLTE S, CORDELIÈRES FP. 2006. A guided tour into subcellular colocalization analysis in light microscopy. *J Microsc* **224**:213–232. doi:10.1111/j.1365-2818.2006.01706.x

Bonanomi D, Valenza F, Chivatakarn O, Sternfeld MJ, Driscoll SP, Aslanian A, Lettieri K, Gullo M, Badaloni A, Lewcock JW, Hunter T, Pfaff SL. 2019. p190RhoGAP Filters Competing Signals to Resolve Axon Guidance Conflicts. *Neuron* **102**:602-620.e9. doi:10.1016/j.neuron.2019.02.034

Burk K, Mire E, Bellon A, Hocine M, Guillot J, Moraes F, Yoshida Y, Simons M, Chauvet S, Mann F. 2017. Post-endocytic sorting of Plexin-D1 controls signal transduction and development of axonal and vascular circuits. *Nat Commun* **8**:14508. doi:10.1038/ncomms14508

Chauvet S, Cohen S, Yoshida Y, Fekrane L, Livet J, Gayet O, Segu L, Buhot M-C, Jessell TM, Henderson CE, Mann F. 2007. Gating of Sema3E/PlexinD1 Signaling by Neuropilin-1 Switches Axonal Repulsion to Attraction during Brain Development. *Neuron* **56**:807–822. doi:10.1016/j.neuron.2007.10.019

Chauvet S, Mire E, Mann F. 2016. Semaphorin Signaling, Methods and Protocols. *Methods Mol Biol* **1493**:223–235. doi:10.1007/978-1-4939-6448-2_16

Chen Y, Aardema J, Corey SJ. 2013. Biochemical and functional significance of F-BAR domain proteins interaction with WASP/N-WASP. *Semin Cell Dev Biol* **24**:280–286. doi:10.1016/j.semcdb.2013.01.005

Dent EW, Gupton SL, Gertler FB. 2011. The Growth Cone Cytoskeleton in Axon Outgrowth and Guidance. *Cold Spring Harb Perspect Biol* **3**:a001800. doi:10.1101/cshperspect.a001800

Ding JB, Oh W-J, Sabatini BL, Gu C. 2012. Semaphorin 3E–Plexin-D1 signaling controls pathway-specific synapse formation in the striatum. *Nat Neurosci* **15**:215–223. doi:10.1038/nn.3003

Droz B, Koenig HL, Biamberardino LD, Giamberardino LD. 1973. Axonal migration of protein and glycoprotein to nerve endings. I. Radioautographic analysis of the renewal of protein in nerve endings of chicken ciliary ganglion after intracerebral injection of [3H]lysine. *Brain Res* **60**:93–127. doi:10.1016/0006-8993(73)90852-4

909 Dupin I, Lokmane L, Dahan M, Garel S, Studer V. 2015. Subrepellent doses of Slit1 promote Netrin-1 chemotactic
910 responses in subsets of axons. *Neural Dev* **10**:5. doi:10.1186/s13064-015-0036-8

911 Dupont S, Wickström SA. 2022. Mechanical regulation of chromatin and transcription. *Nat Rev Genet* **23**:624–
912 643. doi:10.1038/s41576-022-00493-6

913 Ehrman LA, Mu X, Waclaw RR, Yoshida Y, Vorhees CV, Klein WH, Campbell K. 2013. The LIM homeobox
914 gene Isl1 is required for the correct development of the striatonigral pathway in the mouse. *Proc Natl Acad Sci*
915 **110**:E4026–E4035. doi:10.1073/pnas.1308275110

916 Franze K. 2020. Integrating Chemistry and Mechanics: The Forces Driving Axon Growth. *Annu Rev Cell Dev*
917 *Biol* **36**:1–23. doi:10.1146/annurev-cellbio-100818-125157

918 Fukuhara K, Imai F, Ladle DR, Katayama K, Leslie JR, Arber S, Jessell TM, Yoshida Y. 2013. Specificity of
919 Monosynaptic Sensory-Motor Connections Imposed by Repellent Sema3E-PlexinD1 Signaling. *Cell Rep* **5**:748–
920 758. doi:10.1016/j.celrep.2013.10.005

921 Galbraith KK, Fujishima K, Mizuno H, Lee S-J, Uemura T, Sakimura K, Mishina M, Watanabe N, Kengaku M.
922 2018. MTSS1 Regulation of Actin-Nucleating Formin DAAM1 in Dendritic Filopodia Determines Final Dendritic
923 Configuration of Purkinje Cells. *Cell Rep* **24**:95-106.e9. doi:10.1016/j.celrep.2018.06.013

924 Gerfen CR, Surmeier DJ. 2011. Modulation of Striatal Projection Systems by Dopamine. *Annu Rev Neurosci*
925 **34**:441–466. doi:10.1146/annurev-neuro-061010-113641

926 Giehl K, Keller C, Muehlich S, Goppelt-Struebe M. 2015. Actin-Mediated Gene Expression Depends on RhoA
927 and Rac1 Signaling in Proximal Tubular Epithelial Cells. *PLoS ONE* **10**:e0121589.
928 doi:10.1371/journal.pone.0121589

929 Gu C, Yoshida Y, Livet J, Reimert DV, Mann F, Merte J, Henderson CE, Jessell TM, Kolodkin AL, Ginty DD.
930 2005. Semaphorin 3E and Plexin-D1 Control Vascular Pattern Independently of Neuropilins. *Science* **307**:265–
931 268. doi:10.1126/science.1105416

932 Guez-Haddad J, Sporny M, Sasson Y, Gevorkyan-Airapetov L, Lahav-Mankovski N, Margulies D,
933 Radzimanowski J, Opatowsky Y. 2015. The Neuronal Migration Factor srGAP2 Achieves Specificity in Ligand
934 Binding through a Two-Component Molecular Mechanism. *Structure* **23**:1989–2000.
935 doi:10.1016/j.str.2015.08.009

936 Harrington AW, Ginty DD. 2013. Long-distance retrograde neurotrophic factor signalling in neurons. *Nat Rev*
937 *Neurosci* **14**:177–187. doi:10.1038/nrn3253

938 Hayn-Leichsenring G, Liebig C, Miething A, Schulz A, Kumar S, Schwalbe M, Eiberger B, Baader SL. 2011.
939 Cellular distribution of metastasis suppressor 1 and the shape of cell bodies are temporarily altered in Engrailed-
940 2 overexpressing cerebellar Purkinje cells. *Neuroscience* **189**:68–78. doi:10.1016/j.neuroscience.2011.05.038

941 Heiman M, Schaefer A, Gong S, Peterson JD, Day M, Ramsey KE, Suárez-Fariñas M, Schwarz C, Stephan DA,
942 Surmeier DJ, Greengard P, Heintz N. 2008. A Translational Profiling Approach for the Molecular
943 Characterization of CNS Cell Types. *Cell* **135**:738–748. doi:10.1016/j.cell.2008.10.028

944 Jung H, Yoon BC, Holt CE. 2012. Axonal mRNA localization and local protein synthesis in nervous system
945 assembly, maintenance and repair. *Nat Rev Neurosci* **13**:308–324. doi:10.1038/nrn3210

946 Kim J, Oh W-J, Gaiano N, Yoshida Y, Gu C. 2011. Semaphorin 3E–Plexin-D1 signaling regulates VEGF function
947 in developmental angiogenesis via a feedback mechanism. *Genes Dev* **25**:1399–1411. doi:10.1101/gad.2042011

948 Kim N, Jun M-H, Jeong J-Y, Oh W-J. 2022. Optimized protocol for translatome analysis of mouse brain
949 endothelial cells. *PLoS ONE* **17**:e0275036. doi:10.1371/journal.pone.0275036

950 Klingberg A, Hasenberg A, Ludwig-Portugall I, Medyukhina A, Männ L, Brenzel A, Engel DR, Figge MT, Kurts
951 C, Gunzer M. 2017. Fully Automated Evaluation of Total Glomerular Number and Capillary Tuft Size in Nephritic
952 Kidneys Using Lightsheet Microscopy. *J Am Soc Nephrol* **28**:452–459. doi:10.1681/asn.2016020232

953 Kolodkin AL, Tessier-Lavigne M. 2011. Mechanisms and Molecules of Neuronal Wiring: A Primer. *Cold Spring*
954 *Harb Perspect Biol* **3**:a001727. doi:10.1101/cshperspect.a001727

955 Kreitzer AC, Malenka RC. 2008. Striatal Plasticity and Basal Ganglia Circuit Function. *Neuron* **60**:543–554.
956 doi:10.1016/j.neuron.2008.11.005

957 Kronman H, Richter F, Labonté B, Chandra R, Zhao S, Hoffman G, Lobo MK, Schadt EE, Nestler EJ. 2019.
958 Biology and Bias in Cell Type-Specific RNAseq of Nucleus Accumbens Medium Spiny Neurons. *Sci Rep* **9**:8350.
959 doi:10.1038/s41598-019-44798-9

960 Kuo H-Y, Liu F-C. 2019. Synaptic Wiring of Corticostriatal Circuits in Basal Ganglia: Insights into the
961 Pathogenesis of Neuropsychiatric Disorders. *eNeuro* **6**:ENEURO.0076-19.2019. doi:10.1523/eneuro.0076-
962 19.2019

963 Lin J, Liu J, Wang Y, Zhu J, Zhou K, Smith N, Zhan X. 2005. Differential regulation of cortactin and N-WASP-
964 mediated actin polymerization by missing in metastasis (MIM) protein. *Oncogene* **24**:2059–2066.
965 doi:10.1038/sj.onc.1208412

966 Lin X, Wang H, Lou Z, Cao M, Zhang Z, Gu N. 2018. Roles of PIP2 in the membrane binding of MIM I-BAR:
967 insights from molecular dynamics simulations. *FEBS Lett* **592**:2533–2542. doi:10.1002/1873-3468.13186

968 Lobo MK, Karsten SL, Gray M, Geschwind DH, Yang XW. 2006. FACS-array profiling of striatal projection
969 neuron subtypes in juvenile and adult mouse brains. *Nat Neurosci* **9**:443–452. doi:10.1038/nn1654

970 Lowery LA, Vactor DV. 2009. The trip of the tip: understanding the growth cone machinery. *Nat Rev Mol Cell*
971 *Biol* **10**:332–343. doi:10.1038/nrm2679

972 Machesky LM, Johnston SA. 2007. MIM: a multifunctional scaffold protein. *J Mol Med* **85**:569–576.
973 doi:10.1007/s00109-007-0207-0

974 Mata A, Gil V, Pérez-Clausell J, Dasilva M, González-Calixto MC, Soriano E, García-Verdugo JM, Sanchez-
975 Vives MV, Río JA del. 2018. New functions of Semaphorin 3E and its receptor PlexinD1 during developing and
976 adult hippocampal formation. *Sci Rep* **8**:1381. doi:10.1038/s41598-018-19794-0

977 Mattila PK, Salminen M, Yamashiro T, Lappalainen P. 2003. Mouse MIM, a Tissue-specific Regulator of
978 Cytoskeletal Dynamics, Interacts with ATP-Actin Monomers through Its C-terminal WH2 Domain*. *J Biol Chem*
979 **278**:8452–8459. doi:10.1074/jbc.m212113200

980 Minkeviciene R, Hlushchenko I, Virenque A, Lahti L, Khanal P, Rauramaa T, Koistinen A, Leinonen V, Noe FM,
981 Hotulainen P. 2019. MIM-Deficient Mice Exhibit Anatomical Changes in Dendritic Spines, Cortex Volume and
982 Brain Ventricles, and Functional Changes in Motor Coordination and Learning. *Front Mol Neurosci* **12**:276.
983 doi:10.3389/fnmol.2019.00276

984 Miralles F, Posern G, Zaromytidou A-I, Treisman R. 2003. Actin Dynamics Control SRF Activity by Regulation
985 of Its Coactivator MAL. *Cell* **113**:329–342. doi:10.1016/s0092-8674(03)00278-2

986 Morello F, Prasad AA, Rehberg K, Sá RV de, Antón-Bolaños N, Leyva-Diaz E, Adolfs Y, Tissir F, López-Bendito
987 G, Pasterkamp RJ. 2015. Frizzled3 Controls Axonal Polarity and Intermediate Target Entry during Striatal
988 Pathway Development. *J Neurosci* **35**:14205–14219. doi:10.1523/jneurosci.1840-15.2015

989 Moriya J, Minamino T, Tateno K, Okada S, Uemura A, Shimizu I, Yokoyama M, Nojima A, Okada M, Koga H,
990 Komuro I. 2010. Inhibition of Semaphorin As a Novel Strategy for Therapeutic Angiogenesis. *Circ Res* **106**:391–
991 398. doi:10.1161/circresaha.109.210815

992 Neuhaus-Follini A, Bashaw GJ. 2015. The Intracellular Domain of the Frazzled/DCC Receptor Is a Transcription
993 Factor Required for Commissural Axon Guidance. *Neuron* **87**:751–763. doi:10.1016/j.neuron.2015.08.006

994 O'Donnell M, Chance RK, Bashaw GJ. 2009. Axon Growth and Guidance: Receptor Regulation and Signal
995 Transduction. *Annu Rev Neurosci* **32**:383–412. doi:10.1146/annurev.neuro.051508.135614

996 Oh W-J, Gu C. 2013a. The role and mechanism-of-action of Sema3E and Plexin-D1 in vascular and neural
997 development. *Semin Cell Dev Biol* **24**:156–162. doi:10.1016/j.semcdb.2012.12.001

998 Oh W-J, Gu C. 2013b. Establishment of Neurovascular Congruency in the Mouse Whisker System by an
999 Independent Patterning Mechanism. *Neuron* **80**:458–469. doi:10.1016/j.neuron.2013.09.005

1000 Pecho-Vrieseling E, Sigrist M, Yoshida Y, Jessell TM, Arber S. 2009. Specificity of sensory–motor connections
1001 encoded by Sema3e–Plxnd1 recognition. *Nature* **459**:842–846. doi:10.1038/nature08000

1002 Penrod RD, Kourrich S, Kearney E, Thomas MJ, Lanier LM. 2011. An embryonic culture system for the
1003 investigation of striatal medium spiny neuron dendritic spine development and plasticity. *J Neurosci Methods*
1004 **200**:1–13. doi:10.1016/j.jneumeth.2011.05.029

1005 Percipalle P, Visa N. 2006. Molecular functions of nuclear actin in transcription. *J Cell Biol* **172**:967–971.
1006 doi:10.1083/jcb.200512083

1007 Poliak S, Morales D, Croteau L-P, Krawchuk D, Palmesino E, Morton S, Cloutier J-F, Charron F, Dalva MB,
1008 Ackerman SL, Kao T-J, Kania A. 2015. Synergistic integration of Netrin and ephrin axon guidance signals by
1009 spinal motor neurons. *eLife* **4**:e10841. doi:10.7554/elife.10841

1010 Russell SA, Bashaw GJ. 2018. Axon guidance pathways and the control of gene expression. *Dev Dyn* **247**:571–
1011 580. doi:10.1002/dvdy.24609

1012 Saarikangas J, Kourdougli N, Senju Y, Chazal G, Segerstråle M, Minkeviciene R, Kuurne J, Mattila PK, Garrett
1013 L, Hölter SM, Becker L, Racz I, Hans W, Klopstock T, Wurst W, Zimmer A, Fuchs H, Gailus-Durner V,
1014 Hrabě de Angelis M, von Ossowski L, Taira T, Lappalainen P, Rivera C, Hotulainen P. 2015. MIM-Induced
1015 Membrane Bending Promotes Dendritic Spine Initiation. *Dev Cell* **33**:644–659. doi:10.1016/j.devcel.2015.04.014

1016 Sakurai A, Gavard J, Annas-Linhares Y, Basile JR, Amornphimoltham P, Palmby TR, Yagi H, Zhang F, Randazzo
1017 PA, Li X, Weigert R, Gutkind JS. 2010. Semaphorin 3E Initiates Antiangiogenic Signaling through Plexin D1 by
1018 Regulating Arf6 and R-Ras. *Mol Cell Biol* **30**:3086–3098. doi:10.1128/mcb.01652-09

1019 Sakurai A, Jian X, Lee CJ, Manavski Y, Chavakis E, Donaldson J, Randazzo PA, Gutkind JS. 2011.
1020 Phosphatidylinositol-4-phosphate 5-Kinase and GEP100/Brag2 Protein Mediate Antiangiogenic Signaling by
1021 Semaphorin 3E-Plexin-D1 through Arf6 Protein*. *J Biol Chem* **286**:34335–34345. doi:10.1074/jbc.m111.259499

1022 Samarakoon R, Goppelt-Struebe M, Higgins PJ. 2010. Linking cell structure to gene regulation: Signaling events
1023 and expression controls on the model genes PAI-1 and CTGF. *Cell Signal* **22**:1413–1419.
1024 doi:10.1016/j.cellsig.2010.03.020

1025 Scott-Solomon E, Kuruvilla R. 2018. Mechanisms of neurotrophin trafficking via Trk receptors. *Mol Cell*
1026 *Neurosci* **91**:25–33. doi:10.1016/j.mcn.2018.03.013

1027 Surmeier DJ, Ding J, Day M, Wang Z, Shen W. 2007. D1 and D2 dopamine-receptor modulation of striatal
1028 glutamatergic signaling in striatal medium spiny neurons. *Trends Neurosci* **30**:228–235.
1029 doi:10.1016/j.tins.2007.03.008

1030 Tata A, Stoppel DC, Hong S, Ben-Zvi A, Xie T, Gu C. 2014. An image-based RNAi screen identifies SH3BP1 as
1031 a key effector of Semaphorin 3E–PlexinD1 signaling. *J Cell Biol* **205**:573–590. doi:10.1083/jcb.201309004

1032 Tessier-Lavigne M, Goodman CS. 1996. The Molecular Biology of Axon Guidance. *Science* **274**:1123–1133.
1033 doi:10.1126/science.274.5290.1123

1034 Vitriol EA, Zheng JQ. 2012. Growth Cone Travel in Space and Time: the Cellular Ensemble of Cytoskeleton,
1035 Adhesion, and Membrane. *Neuron* **73**:1068–1081. doi:10.1016/j.neuron.2012.03.005

1036 Winckler B, Mellman I. 2010. Trafficking Guidance Receptors. *Cold Spring Harb Perspect Biol* **2**:a001826.
1037 doi:10.1101/cshperspect.a001826

1038 Yamashita N. 2019. Retrograde signaling via axonal transport through signaling endosomes. *J Pharmacol Sci*
1039 **141**:91–96. doi:10.1016/j.jphs.2019.10.001

1040 Yamashita N, Usui H, Nakamura F, Chen S, Sasaki Y, Hida T, Suto F, Taniguchi M, Takei K, Goshima Y. 2014.
1041 Plexin-A4-dependent retrograde semaphorin 3A signalling regulates the dendritic localization of GluA2-
1042 containing AMPA receptors. *Nat Commun* **5**:3424. doi:10.1038/ncomms4424

1043 Yeh ML, Gonda Y, Mommersteeg MTM, Barber M, Ypsilanti AR, Hanashima C, Parnavelas JG, Andrews WD.
1044 2014. Robo1 Modulates Proliferation and Neurogenesis in the Developing Neocortex. *J Neurosci* **34**:5717–5731.
1045 doi:10.1523/jneurosci.4256-13.2014

1046 Yu J, Lin S, Wang Mei, Liang L, Zou Z, Zhou X, Wang Meichi, Chen P, Wang Y. 2016. Metastasis suppressor 1
1047 regulates neurite outgrowth in primary neuron cultures. *Neuroscience* **333**:123–131.
1048 doi:10.1016/j.neuroscience.2016.07.002

1049 Yu R, Kim N, Li Y, Jeong J-Y, Park S-J, Zhou B, Oh W-J. 2022. Vascular Sema3E-Plexin-D1 Signaling
1050 Reactivation Promotes Post-stroke Recovery through VEGF Downregulation in Mice. *Transl Stroke Res* **13**:142–
1051 159. doi:10.1007/s12975-021-00914-4

1052 Zwaag BVD, Hellemons AJCGM, Leenders WPJ, Burbach JPH, Brunner HG, Padberg GW, Bokhoven HV. 2002.
1053 PLEXIN-D1, a novel plexin family member, is expressed in vascular endothelium and the central nervous system
1054 during mouse embryogenesis. *Dev Dyn* **225**:336–343. doi:10.1002/dvdy.10159

1055

1056

Figure legends

Figure 1. Sema3E-Plexin-D1 signaling induces Mtss1 expression selectively in developing striatonigral projecting neurons. (A) RNA sequencing (RNA-seq) analysis of wild-type (WT) (*Plxnd1*$^{f/f}$) and conditional neuronal knockout (cKO) (*Nes-cre; Plxnd1*$^{f/f}$) pups at P5. The box in red indicates the dorsal striatum region from which RNA was isolated. (B) Volcano plot of significant differentially expressed genes (DEGs) between WT and *Plxnd1* cKO. Blue and red circles indicate significantly down- and upregulated genes, respectively, as indicated by a fold change greater than 2. (C) Relative levels of *Mtss1* expression in the striatum of WT or *Plxnd* cKO mice at P5 were compared by quantitative RT–PCR (RT–qPCR). n=16 for WT mice, n=14 for *Plxnd1* cKO mice in four independent experiments. (D-E) Western blot images showing Mtss1 expression in the striatum of WT or *Plxnd1* cKO mice and quantification. The values are averaged from n=5 for WT mice and n=4 for *Plxnd1* cKO mice. (F-G) Western blot images and quantification of Mtss1 expression in the striatum of WT or *Sema3e* KO mice at P5. WT mice, n=7, and *Sema3e* KO mice, n=8. (H) Fluorescence *in situ* hybridization (FISH) for *Plxnd1* mRNA (green) and *Mtss1* mRNA (red) in the striatum of WT or *Plxnd1* cKO mice at P5. White dotted boxes are shown in the inset image on the bottom. Scale bar, 200 μm. (I) Quantification of fluorescence intensity to measure the expression levels of Mtss1 in (H). WT mice, n=3, and *Plxnd1* cKO mice, n=3. (J) Immunohistochemistry showing tdTomato-expressing Drd1a+ MSNs (red) and Mtss1 (green) in the striatum of *Drd1a-tdT* mice at P5. The small boxes in the striatum and cortex are shown at better resolution in the inset images. Scale bar, 100 μm. (K) Western blot images showing the expression of Mtss1 and Plexin-D1 in the striatum of WT or *Plxnd1* cKO mice at different developmental stages ranging from E16.5 to P0. (L) Quantification of band intensity in (K). WT, n=4, and KO, n=4 at E16.5, WT, n=3, and KO, n=3 at E18.5, WT, n=3, and KO, n=3 at P0. (M-N) Western blot images showing the temporal expression of Plexin-D1 and Mtss1 in the striatum from E14.5 to adulthood (8 weeks old) and quantification. Error bars, mean ± SEM; *$p<0.05$, **$p<0.01$ by Student's t test for all quantifications. The values represent the average band intensity, n=3 at each age. str, striatum; cx, cortex; Th, thalamus; SNr, substantia nigra. Source data 1. Western blots shown in Figures 1D, 1F, 1K, and 1M.

1081 **Figure 2. In cultured MSNs, Mtss1 expression is directly regulated by Sema3E-Plexin-D1 signaling through**
1082 **the AKT pathway.** (A) Western blot images showing Mtss1 expression in MSNs derived from the striatum of
1083 WT or *Plxnd1* cKO mice at P0 and measured at DIV3 and DIV6 in culture. (B) Quantification of band intensity
1084 in (A). two-way ANOVA with Tukey's post hoc correction for multiple comparisons; n=3. (C) Mtss1 expression
1085 in MSNs obtained from the striatum of WT or Sema3e KO mice at P0 and measured at DIV6 in culture. (D)
1086 Quantification of the blots shown in (C). Student's t test; n=5 for WT, n=5 for KO in five independent
1087 experiments. (E) Schematic illustration of the experimental strategy for Sema3E-ligand or MK2206, an AKT
1088 inhibitor treatment in MSN culture. (F-G) Western blot images showing Mtss1 expression after AP-Sema3E (2
1089 nM) treatment in cultured MSNs derived from Sema3e KO mice or *Plxnd1* cKO mice. (H-I) Quantification of (F
1090 and G). Student's t test; AP, n=4, AP-sema3E, n=4 for *sema3e* KO mice, AP n=4, AP-sema3E n=4 for *Plxnd1* cKO
1091 mice in three independent experiments. (J-K) Western blot to analyze the expression of Mtss1 and Plexin-D1 after
1092 MK2206 (100 nM) treatment in cultured MSNs and subsequent quantification for band intensity (L-M). Student's
1093 t test; n=6 for sham, n=6 for MK2206 in six independent experiments. (N-O) Western blot image and analysis
1094 showing Mtss1 expression in *Sema3e* knockout MSNs treated with MK2206 after incubation with AP-Sema3E.
1095 two-way ANOVA with Tukey's post hoc correction for multiple comparisons; n=5 in five independent experiments.
1096 Error bars, mean ± SEM; *p<0.05, **p<0.01, ***p<0.001 by indicated statistical tests. Source data 1. Western
1097 blots shown in Figures 2A, 2C, 2F, 2G, 2J, 2K, and 2N.

1098

1099 **Figure 3. Mtss1 contributes to neurite extension of Drd1a-positive MSNs under the regulation of Sema3E-**
1100 **Plexin-D1 signaling.** (A) Immunocytochemistry for Mtss1 (green), Tau (gray), and F-actin (red) in cultured MSNs
1101 at DIV3 obtained from WT or *Mtss1* cKO mice. White dotted boxes are shown in the inset image on the bottom.
1102 Scale bar, 10 μm. (B) Representative images of Drd1a+ MSNs at DIV3 derived from WT (*Drd1a-tdT; Mtss1*$^{f/f}$) or
1103 *Mtss1* cKO (*Drd1a-tdT; Nes-cre; Mtss1*$^{f/f}$) mice. Scale bar, 20 μm. (C) Quantification of neurite length in (B) was
1104 performed as previously reported (Chauvet et al., 2016). The values represent the average ratio of the fold change
1105 in length compared to the control samples. Student's t test; n=179 for WT, n=184 for *Mtss1* cKO, in three
1106 independent experiments. (D) Percentage of Drd1a-positive MSNs with neurites shorter than twice the cell body
1107 diameter in (B-C). $\chi 2$ test; n=48 for WT, n=48 for *Mtss1* cKO in four independent experiments. (E) Representative

1108 images of Drd1a+ MSNs at DIV6 derived from WT (*Drd1a-tdT; Mtss1*$^{f/f}$) or *Mtss1* cKO (*Drd1a-tdT; Nes-cre;*
1109 *Mtss1*$^{f/f}$) mice. Scale bar, 50 μm. (F) Quantification of neurite length in (E). Student's t test; n=210 for WT, n=260
1110 for *Mtss1* cKO in three independent experiments. (G) Representative images of Drd1a+ MSNs at DIV3 derived
1111 from WT (*Drd1a-tdT; Plxnd1*$^{f/f}$) or *Plxnd1* cKO (*Drd1a-tdT; Nes-cre; Plxnd1*$^{f/f}$) mice. Scale bar, 20 μm. (H)
1112 Quantification of neurite length in (G). Student's t test; n=167 for WT, n=159 for *Plxnd1* cKO in three independent
1113 experiments. (I) Representative images of Drd1a+ MSNs at DIV6 derived from WT or *Plxnd1* cKO mice. Scale
1114 bar, 50 μm. (J) Quantification of neurite length in (I). Student's t test; n=339 for WT, n=403 for *Plxnd1* cKO in
1115 three independent experiments. (K) Representative images of GFP- or Mtss1-myc-transfected-Drd1a+ MSNs at
1116 DIV6 derived from WT or *Plxnd1* cKO mice. Scale bar, 50 μm. (L) Quantification of neurite length in (K). Error
1117 bars, mean ± SEM; *p<0.05, ****p<0.0001 by one-way ANOVA with Tukey's post hoc correction for multiple
1118 comparisons; n=163 for WT+GFP, n=187 for *Plxnd1* cKO+GFP, n=195 for *Plxnd1* cKO+Mtss1-myc in three
1119 independent experiments. Error bars, mean ± SEM; ns p>0.05, *p<0.05, ****p<0.0001 by indicated statistical
1120 tests.

1121

1122 **Figure 4. The Mtss1 I-BAR domain directly binds to Plexin-D1, independent of Sema3E.** (A) Schematics
1123 depicting full-length constructs of Mtss1 and its truncation mutants. (B) Coimmunoprecipitation and immunoblot
1124 analysis of HEK293T cells transfected with Mtss1-myc with vsv-Plexin-D1. The interaction between Mtss1 and
1125 Plexin-D1 was investigated by immunoprecipitation with anti-vsv (left) or anti-myc (right) antibodies and
1126 subsequent Western blotting with reciprocal antibodies. (C) Immunoprecipitation and Western blot analysis after
1127 Plexin-D1 and Mtss1 overexpression. The vsv-Plexin-D1ΔICD did not bind to Mtss1-myc. (D)
1128 Immunoprecipitation and Western blot assays to identify the binding domain in Mtss1 that interacts with Plexin-
1129 D1. (E) The interaction between Mtss1 and Plexin-D1 was assessed over time following treatment with Sema3E
1130 (2 nM) and was not affected by AP-Sema3E treatment. (F) Graph quantifying the band intensity in (E). Error bars,
1131 mean ± SEM; ns p>0.05 by two-way ANOVA with Bonferroni's post hoc correction for multiple comparisons;
1132 n=3 in three independent experiments. (G) Pull-down assay and visualization of the protein bands using
1133 Coomassie staining. His-Mtss1-IBAR binds directly to Plexin-D1-ICD-strep. Source data 1. Western blots and
1134 Gel shown in Figures 4B, 4C, 4D, 4E, and 4G.

1135 **Figure 5. Mtss1 facilitates Plexin-D1 transport to the growth cone in cultured Drd1a-positive MSNs.**
1136 (A) Immunocytochemistry for Mtss1-myc or Mtss1ΔI-BAR -myc (green), vsv-Plexin-D1 (red) in the axons of
1137 MSNs transfected with vsv-Plexin-D1 and Mtss1-myc or Mtss1ΔI-BAR-myc, using *Mtss1*-null mice as a
1138 background. The images were acquired using structured illumination microscopy (N-SIM). Scale bar, 5 μm. (B)
1139 Quantification of the fluorescence intensity in the axons of (A). two-way ANOVA with Tukey's post hoc
1140 correction for multiple comparisons; vsv-Plexin-D1+Mtss1-myc, n=21, and vsv-Plexin-D1+Mtss1ΔI-BAR-myc,
1141 n=14. (C) Quantification of colocalization by Pearson's correlation coefficient calculated using Costes'
1142 randomized pixel scrambled image method. Student's t test; vsv-Plexin-D1+Mtss1-myc, n=21, and vsv-Plexin-
1143 D1+Mtss1ΔI-BAR-myc, n=14. (D) Immunocytochemistry for vsv-Plexin-D1 (red), Mtss1-myc (green), and F-
1144 actin (gray) in the growth cones of MSNs transfected with vsv-Plexin-D1 and Mtss1-myc or Mtss1ΔI-BAR-myc
1145 originating from *Mtss1*-null mice. Scale bar, 5 μm. (E) Quantification of the intensities in the growth cones. The
1146 values represent the average fold change in expression compared to the control samples (vsv-Plexin-D1+Mtss1-
1147 myc). two-way ANOVA with Tukey's post hoc correction for multiple comparisons; vsv-Plexin-D1+Mtss1-myc,
1148 n=8, and vsv-Plexin-D1+Mtss1ΔI-BAR-myc, n=9. (F) Quantification of colocalization by Pearson's correlation
1149 coefficient calculated using Costes' randomized pixel scrambled image method. Student's t test; vsv-Plexin-
1150 D1+Mtss1-myc, n=8, and vsv-Plexin-D1+Mtss1ΔI-BAR-myc, n=9. (G) Representative time-lapse images of
1151 Plexin-D1-GFP-positive vesicles (Green) from wild-type or *Mtss1* cKO MSNs at DIV6. Plexin-D1-positive
1152 vesicles transported towards distal or proximal directions are indicated by red and yellow arrowheads, respectively.
1153 White arrowheads indicate stationary vesicles. A mean velocity of less than 0.1 μm/s was considered to be a
1154 stationary condition. See videos 1-4. Scale bar, 5 μm. (H-J) Quantification of mean velocity (H), total travel
1155 distance (I), and number of vesicles (J) along neurites of Plexin-D1-positive vesicles. Student's t test; n=23 for
1156 WT, n=25 for *Mtss1* cKO in four independent experiments. (K) Distribution analysis of vesicle directionality. (L)
1157 The AP-Sema3E binding assay was performed to visualize Plexin-D1 protein (black arrows) in the growth cones
1158 of WT or *Plxnd1*-deficient MSNs. Scale bar, 10 μm. (L) The AP-Sema3E binding assay performed to visualize
1159 Plexin-D1 protein (black arrows) in the growth cones of WT or *Mtss1*-deficient MSNs. Localization of Plexin-D1
1160 (black arrows) in the growth cone investigated in cultured MSNs from WT (*Drd1a-tdT; Mtss1*$^{f/f}$) or *Mtss1* cKO
1161 (*Drd1a-tdT; Nes-cre; Mtss1*$^{f/f}$) mice. (M) Quantification of Plexin-D1 intensity shown in (L). Mann–Whitney test;
1162 WT n=51, KO n=50. Error bars in all graphs, mean ± SEM; *p<0.05, **p<0.01, ***p<0.001. ****p<0.0001 by

1163 indicated statistical tests.

1164 **Figure 6. The repulsive response through Sema3E-Plexin-D1 signaling is attenuated in the absence of Mtss1.**
1165 (A) A growth cone collapse assay in the presence or absence of Sema3E (2 nM) was performed with MSN cultures
1166 derived from WT (*Drd1a-tdT; Mtss1*$^{f/f}$) or *Mtss1*-KO (*Drd1a-tdT; Nes-cre; Mtss1*$^{f/f}$) mice at DIV3. Scale bar, 10
1167 μm. The images were obtained from N-SIM. (B) Quantification of collapsed growth cones in (A). Error bars,
1168 mean ± SEM; ***p<0.001, ****p<0.0001 by χ2 test; WT+AP, n=155, WT+AP-Sema3E, n=163, KO+AP, n=149,
1169 KO+AP-Sema3E, n=149. (C) A growth cone collapse assay in the presence or absence of Sema3E (2 nM) was
1170 performed with MSN cultures following ectopic expression of Mtss1-myc or Mtss1ΔI–BAR-myc in the *Mtss1*-
1171 null background at DIV3. Scale bar, 10 μm. (D) Quantification of collapsed growth cones in (C). Error bars, mean
1172 ± SEM; ***p<0.001, ****p<0.0001 by χ2 test; Mtss1-myc+AP, n=28, Mtss1-myc +AP-Sema3E, n=28, Mtss1ΔI-
1173 BAR-myc+AP, n=28, Mtss1ΔI–BAR-myc +AP-Sema3E, n=43. (E) Quantification of the collapse assay in the
1174 presence or absence of Sema3E (2 nM) was performed with MSN cultures at DIV6 from WT (*Drd1a-tdT; Plxnd1*$^{f/f}$)
1175 or *Plxnd1*-KO (*Drd1a-tdT; Nes-cre; Plxnd1*$^{f/f}$) mice. ****p<0.0001 by χ2 test; WT+AP, n=44, WT+AP-Sema3E,
1176 n=45, KO+AP, n=45, KO+AP-Sema3E, n=46. in three independent experiments. (F) Quantification of a growth
1177 cone collapse assay in the presence or absence of Sema3E (2 nM) was performed with MSN cultures following
1178 ectopic expression of vsv-Plexin-D1 or vsv-Plexin-D1ΔICD in the *Plxnd1*-KO background at DIV6.
1179 ****p<0.0001 by χ2 test; vsv-Plexin-D1+AP, n=35, vsv-Plexin-D1+AP-Sema3E, n=32, vsv-Plexin-D1ΔICD+AP,
1180 n=30, vsv-Plexin-D1ΔICD+AP-Sema3E, n=26 in three independent experiments. tdT, tdTomato.

1181

1182 **Figure 7. A reduced number of Plexin-D1 molecules localize to the developing striatonigral projections in**
1183 ***Mtss1*-deficient mice.** (A) AP-Sema3E binding assay (top) to detect Plexin-D1 expression (white arrows) in
1184 striatonigral projections and immunohistochemistry (bottom) for neurofilaments (NFs) indicated by red dotted
1185 square, performed in adjacent parasagittal sections at E17.5 of WT or *Mtss1* cKO mice. The diminished
1186 projections are marked by white brackets (middle of the striatum) and arrowheads (near substantia nigra regions).
1187 Scale bar, 500 μm. (B) Quantification of the Plexin-D1-positive area in the total striatonigral projection at E17.5
1188 of WT or *Mtss1* cKO mice. Student's t test; WT, n=12, KO, n=12 (3 sections/mouse). (C) Quantification of the
1189 fluorescence density (intensity/area) of neurofilament (NF) in striatonigral projections at E17.5 in WT or *Mtss1*

cKO mice. Student's t test; WT, n=16, KO, n=17 (3 or 4 sections/mouse). (D) Quantification of the AP density (intensity/area) in striatonigral projections at E17.5 in WT or *Mtss1* cKO mice. Student's t test; WT, n=16, KO, n=17 (3 or 4 sections/mouse). (E) The ratio of AP to NF density (intensity/area). Student's t test; WT, n=16, KO, n=17 (3 or 4 sections/mouse). (F) Coronal view of Plexin-D1 localization in striatonigral projections at E17.5 in WT or *Mtss1* cKO mice. Yellow dotted lines indicate the corridor between the thalamus and globus pallidus. Insets show the images in dotted boxes at higher resolution. Scale bar, 200 μm. (G) Representative images of Plexin-D1 molecules in striatonigral projections visualized by AP-Sema3E binding assay in WT or *Mtss1* cKO mice at P5. White arrows indicate striatonigral projections. Scale bar, 1 mm. (H) Schematic representing the quantified region. The dotted blue lines indicate the striatonigral projection-covering areas. The width (red segment) of the striatonigral tract was measured as previously described (Burk et al., 2017). (I-J) Quantification of the Plexin-D1-positive area (%) in dotted blue area and projection width at P5 according to the scheme shown in (H). Mann–Whitney test (I) and Student's t test (J). n=18 (3 sections/mouse). (K) Immunohistochemistry of coronal sections of striatal projections labeled with td-Tomato endogenously expressed through the *Drd1a* promotor in WT (*Drd1a-tdT; Mtss1*$^{f/f}$) or *Mtss1* cKO mice (*Drd1a-tdT; Nes-cre; Mtss1*$^{f/f}$) at P5. The white dotted boxes in the left images are shown in the inset images on the right, which were captured in a single plane using a high-resolution confocal microscope. Scale bar, 500 μm. (L-M) Quantification of the density (intensity/area) (L) and area size (M) of the striatonigral projection in the dotted region in the inset images. Mann–Whitney test (L) and Student's t test (M); n=18 per group (6 sections/mouse). (N) AP-Sema3E binding assay and tdT immunostaining in adjacent sections of WT or *Mtss1* cKO mice located near the SNr. The green line in H indicates the location for cross-sectioning. The inset images of Plexin-D1-positive striatonigral projections were taken from the blue dotted boxes in the left panels. The dotted white lines indicate the tdT-positive striatonigral projections. Scale bar, 200 μm. (O-P) Quantification of the density (intensity/area) of tdT (O) and AP (P) of striatonigral projections WT or *Mtss1* cKO mice. (Q) The ratio of AP to tdT density (intensity/area). Student's t test; WT, n=18, KO, n=18 (6 sections/mouse). (R) Immunohistochemistry of coronal views of striatonigral projections in WT (*Drd1a-tdT; Plxnd1*$^{f/f}$) or *Plxnd1* cKO mice (*Drd1a-tdT; Nes-cre; Plxnd1*$^{f/f}$) at P5. The white dotted boxes in the left images are shown in the inset images on the right, which were obtained using a high-resolution confocal microscope in a single plane. Scale bar, 500 μm. (S-T) Quantification of the density (intensity/area) of tdT (S) and area size (T). Student's t test; n=18 per group (6 sections/mouse). Error bars, mean ± SEM; *p<0.05, **p<0.01, ***p<0.001. ****p<0.0001 by indicated

statistical tests. str, striatum; cx, cortex; Th, thalamus; SNr, substantia nigra; EP, entopeduncular nucleus; Gp, globus pallidus; Hp, hippocampus.

Figure 8. Direct-pathway MSNs exhibit irregular projection patterns in the absence of either Mtss1 or Plexin-D1. (A) Immunohistochemistry of parasagittal sections of striatonigral projections labeled with Drd1a-tdT in WT or *Mtss1* cKO mice at P5. The white boxes in the left images are shown in the inset image on the right. Misguided striatonigral projections are indicated by white arrowheads. The phenotype was observed in five out of five *Mtss1* cKO mice at P5. Scale bar, 500 μm. (B) Schematics depicting DiI injection (red asterisk) into the dorsal striatum for sparse labeling of striatonigral projections. The regions indicated in the blue square were captured for three-dimensional (3-D) visualization. (C) Representative 3-D images of DiI-labeled axonal tracks in WT or *Mtss1* cKO mice at P5. Compared to the fasciculated straight projections in WT (Top panels), the striatonigral projections of *Mtss1* cKO mice presented relatively defasciculated (Bottom panels) and occasionally severely misrouted patterns (white arrow in the bottom right panel). The phenotype was observed in three out of three *Mtss1* cKO mice. Scale bar, 200 μm. (D) Representative images showing parasagittal sections of brains from WT or *Plxnd1* cKO mice at P5. The misrouted projections are also indicated by white arrowheads in the magnified inset images. The phenotype was observed in four out of four *Plxnd1* cKO mice at P5. Scale bar, 500 μm. (E-F) Quantification of the number of intersecting axonal bundles within the corresponding area from Mtss1 cKO (A) or Plxnd1 cKO (D). (E) Student's t test; n=5 mice for WT, n=5 mice for Mtss1 cKO. (F) Student's t test; n=5 mice for WT, n=4 mice for Plxnd1 cKO. Error bars, mean ± SEM; **$p<0.01$, ***$p<0.001$ by indicated statistical tests. (J) Model showing that Mtss1, upregulated by the Sema3E-Plexin-D1 signaling pathway, promotes axonal growth and directs Plexin-D1 to the growth cone to receive a repulsive guidance signal.

Supplemental figure legends

Figure S1. Identification of Mtss1 in the striatum on P5 through RNA sequencing (RNA-seq) analysis. (A) Expression of *Plxnd1* mRNA from wild-type (WT) (*Plxnd1*$^{f/f}$) or conditional-knockout (cKO) (*Nes-cre; Plxnd1*$^{f/f}$) littermate mouse striatum at P5 was examined via *in situ* hybridization (ISH). Scale bars, 500 μm. (B) *Plxnd1* mRNA expression was determined by reverse transcription-polymerase chain reaction (RT–PCR). (C) Common gene expression patterns were determined through two independent experiments and by RNA-seq. The values in the principal component analysis (PCA) plot indicate the amount of variation attributed to each principal component. Small circles indicate individual samples, and large ovals represent experimental groups. (D) Heatmap showing differential gene expression patterns as determined through RNA-seq analysis. Each row represents hierarchically clustered genes, and each column represents experimental samples with dendrograms and clusters generated with RNA-seq data. Red in the heatmap indicates upregulation of gene expression, and blue denotes downregulation of gene expression; the measures were based on z score. (E) The most highly enriched Gene Ontology (GO) biological process and cellular component categories in *Nes-cre; Plxnd1*$^{f/f}$ samples were visualized on the basis of significant differentially expressed genes (DEGs) determined by RNA-seq. The size of a circle represents enriched genes, and the color represents the $-\log_{10}$ of the P value. Source data 1. RT-PCR shown in Figure S1B.

Figure S2. Sema3E expression through thalamostriatal projections at E16.5. (A) The expression levels of *Plxnd1* mRNA (green) and *Sema3e* mRNA (red) in the brains of E16.5 mice were detected by double fluorescence *in situ* hybridization. The red arrow in the bottom right image indicates the Sema3E protein detected by AP-Plexin-D1-ECD (extracellular domain). Scale bar, 1 mm. (B) Thalamostriatal projections in the parasagittal sections of the brains at E16.5 were stained by DiI to visualize the projecting axons from neurons in the thalamus. Scale bar, 500 μm. (C) Sema3E protein in the striatum of E16.5 brains was detected by Western blot analysis. * indicates a nonspecific band. cx, cortex; str, striatum; and Th, thalamus. Source data 1. Western blots shown in Figure S2C.

Figure S3. Expression of Mtss1 induces I-BAR domain-dependent morphological changes in COS7 cells, generating protrusions. (A) Western blot images showing that weakly expression of endogenous Mtss1 was not

altered by overexpression of Plexin-D1 with or without Sema3E in COS7 cells. Asterisk indicates nonspecific band. (B) Quantification of the band intensity in (A). Error bars, mean ± SEM; ns p>0.05 by two-way ANOVA with Bonferroni's post hoc correction for multiple comparisons; n=3. (C) Schematics describing the full-length construct of Mtss1-myc and its deletion mutant constructs (Mtss1ΔI-BAR-myc, Mtss1ΔWH2-myc, and I-BAR-myc). (D) Immunocytochemistry images taken after overexpression of each construct. Constructs show the I-BAR domain leading to diverse cell protrusion morphologies. Some of the protrusions were excessively spiked or thin and long (arrowheads). Overexpression of the I-BAR domain only (I-BAR-myc) can induce extreme protrusion structures. Scale bar, 20 μm. Source data 1. Western blots shown in Figure S3A.

Figure S4. The interaction between BAR domain-containing proteins and Plexin-D1, or between Mtss1 and Plexin family proteins. (A-C) Coimmunoprecipitation and immunoblot analysis of HEK293T cells transfected with BAR family genes (SH3BP1-HA (N-BAR), HA-srGAP2 (F-BAR), and IRSP53-Flag (I-BAR)) with vsv-Plexin-D1. (D-E) Immunoprecipitation and Western blot analysis after overexpression of Mtss1-myc and Plexin proteins (vsv-Plexin-B2 and vsv-Plexin-B3). The vsv-Plexin-B2 and vsv-Plexin-B3 did not bind to Mtss1-myc. Source data 1. Western blots shown in Figures S4A, S4B, S4C, S4D, and S4E.

Figure S5. Mtss1 expression alters Plexin-D1 localization to the protrusion structure in COS7 cells without affecting its endocytosis or Sema3E binding. (A) Cell surface biotinylation and subsequent Western blot analysis to analyze the surface localization of Plexin-D1 in COS7 cells. (B) Quantification of the surface Plexin-D1 level as shown in (A). The values represent the averages of the fold ratios compared to those of total Plexin-D1. Error bars, mean ± SEM; ns p>0.05 by Student's t test; n=3. (C) Endocytosed biotinylated vsv-PlexinD1 was detected by Western blot analysis following cell surface stripping in the presence or absence of AP-Sema3E (2 nM). (D) Quantification of the band intensity shown in (C). The values in the graph represent the average fold change compared to the expression in control samples (vsv-Plexind1 treated with AP-Sema3E). (E) AP-Sema3E binding assay to test the effect of Mtss1 on the interaction between Sema3E and Plexin-D1. Error bars, mean ± SEM; ns p>0.05 by Kruskal–Wallis test with Dunn's post hoc correction for multiple comparisons; n=8 for vsv-Plexin-D1+AP; n=7 for vsv-Plexin-D1+Mtss1-myc+AP, n=8 for vsv-Plexin-D1+Mtss1-myc+AP, and n=8 for vsv-

1294 Plexin-D1+Mtss1-myc+AP-Sema3E, in three independent experiments. (F) Immunocytochemistry for vsv-
1295 Plexin-D1 (red), Mtss1-myc (green), and F-actin (gray) in COS7 cells. Images were obtained by structured
1296 illumination microscopy (N-SIM). White arrows (top) indicate colocalized Plexin-D1 and Mtss1 in the protrusion
1297 structure. White arrowheads (middle) indicate high Mtss1 levels localized in cell protrusions without Plexin-D1.
1298 Yellow arrows (bottom) indicate the normal cell surface with Mtss1ΔI-BAR but no Plexin-D1 colocalization.
1299 Scale bar, 5 μm. (G) Quantification of colocalization rates shown in (F) between vsv signals and myc signals was
1300 assessed by Pearson's correlation coefficient calculated using Costes' randomized pixel scrambled image method.
1301 Error bars, mean ± SEM; *p<0.05, **p<0.01, ****p<0.0001 by one-way ANOVA with Tukey's post hoc
1302 correction for multiple comparisons; vsv-Plexin-D1+Mtss1-myc, n=12; vsv-Plexin-D1ΔICD+Mtss1-myc, n=12;
1303 vsv-Plexin-D1+Mtss1DI-BAR-myc, n=11. (H) Immunocytochemistry for vsv-Plexin-D1 (red) and Mtss1-myc
1304 (green) with or without AP-Sema3E in COS7 cells. The white dotted boxes are magnified in the panels on the
1305 right. The presence of Sema3E did not affect the positioning of Plexin-D1 and Mtss1 within the protrusion
1306 (arrowheads). Scale bars, 50 μm (left) and 20 μm (magnified images in the right two panels). Source data 1.
1307 Western blots shown in Figures S5A and S5C.

1308

1309 **Figure S6. No significant alteration in the expression of vsv-Plexin-D1 or Mtss1-myc or Mtss1ΔI-BAR-myc**
1310 **in the MSN soma.** (A) Representative image of Immunocytochemistry for vsv-Plexin-D1 (red), Mtss1-myc or
1311 Mtss1ΔI-BAR -myc (green) in the cell body of cultured MSNs transfected with vsv-Plexin-D1 and Mtss1-myc or
1312 Mtss1ΔI-BAR-myc, using Mtss1-null mice as a background. (B) Quantification of the fluorescence intensity in
1313 the cell body of (A). Error bars, mean ± SEM; ns p>0.05 by two-way ANOVA with Tukey's post hoc correction
1314 for multiple comparisons; vsv-Plexin-D1+Mtss1-myc, n=5, and vsv-Plexin-D1+Mtss1ΔI-BAR-myc, n=5. Scale
1315 bar, 5 μm.

1316

1317 **Figure S7. Expression of Mtss1 in the striatonigral tract and SNr at P5.** (A) Illustration showing the region
1318 acquired for the striatonigral tract (area 1) and SNr (area 2). (B) Immunohistochemistry showing tdTomato-
1319 expressing Drd1a+ MSNs (red) and Mtss1 (green) in the striatonigral tract (area 1) and SNr (area 2) in WT (*Drd1a-*
1320 *tdT*; *Mtss1*$^{f/f}$) or *Mtss1* cKO mice (*Drd1a-tdT; Nes-cre; Mtss1*$^{f/f}$) at P5. The white arrow indicates that Mtss1 was

1321 expressed in the striatonigral tract (white star). Scale bars, 100 μm.

1322

1323 **Figure S8. Mtss1 or Plexin-D1 deficiency reduced striatonigral axonal bundles without altering**
1324 **striatonigral projection patterns at P30.** (A) Immunohistochemistry of coronal section images in WT or *Mtss1*
1325 cKO mice at P30. The white dotted boxes in the left images are shown in the inset images, which were captured
1326 in a single plane using a high-resolution confocal microscope. Scale bar, 500 μm. (B-C) Quantifications as
1327 described for the results obtained at P5. Error bars, mean ±SEM; ****$p<0.0001$ by Mann–Whitney test (B) and
1328 ns $p>0.05$ by Student's t test (C); n=18 per group (6 sections/mouse). (D) Coronal images of striatonigral
1329 projections in WT or *Plxnd1* cKO mice at P30. Scale bar, 500 μm. (E-F) Quantification of the density
1330 (intensity/area) (E) and the area size (F) at P30. Error bars, mean ± SEM; **$p<0.01$ by Mann–Whitney test (E)
1331 and ns $p>0.05$ by Student's t test (F); n=18 per group (6 sections/mouse). (G-H) Representative images showing
1332 parasagittal sections of brains from WT or *Mtss1* cKO mice (G) or *Plxnd1* cKO (H). The white boxes in the left
1333 images are shown in the inset image on the right. Misguided striatonigral projections were not observed at P30.
1334 Scale bar, 500 μm. Hp, hippocampus; str, striatum; cx, cortex; Th, thalamus; Gp, globus pallidus; SNr, substantia
1335 nigra.

1336

1337 **Figure S9. The absence of Mtss1 does not affect MSN survival, dendritic arborization, and Plexin-D1**
1338 **expression during striatonigral pathway development.** (A) Immunohistochemistry staining for cleaved caspase
1339 3 (CC3) in the striatum of WT or *Mtss1* cKO mice. The white dotted boxes in the left images are shown in the
1340 inset images on the right at a better resolution. Scale bar, 25 μm. (B) Quantification of cell death by the number
1341 of CC3-positive cells in a 1 mm^2 area covering the dorsal part of the striatum in WT or *Mtss1* cKO mice. Error
1342 bars, mean ± SEM; ns $p>0.05$ by Mann–Whitney test; WT, n=20; *Mtss1* cKO mice, n=20 (5 sections/mouse). (C)
1343 Representative images of Golgi staining at low (top panels) and high (bottom panels) magnification. Scale bars,
1344 100 μm. Sholl analysis of dendritic morphology (D) and dendritic length (E) performed by using Neurolucida360
1345 in 3D analysis. Error bars, mean ± SEM; ns $p>0.05$ by Student's t test; WT, n =12, and *Mtss1* cKO mice, n=15,
1346 from three mice. (F-G) Western blot images and quantification of Plexin-D1 expression in the striatum of WT or
1347 *Mtss1* cKO mice at P5. Error bars, mean ± SEM; *$p<0.05$ by Student's t test; WT mice, n=3, and *Mtss1* cKO mice,

n=4. (H) Plexin-D1 expression in MSNs obtained from the striatum of WT or *Mtss1* cKO mice at P0 and measured at DIV6 in culture. (I) Quantification of the western blots shown in (H). Error bars, mean ± SEM; *p<0.05, by Student's t test; n=3 for WT, n=3 for KO in three independent experiments. Source data 1. Western blots shown in Figures S9F and S9H.

Figure S10. Striatonigral projection defects are observed in Sema3e-null mice at P5. (A) Immunohistochemistry was performed on coronal sections from WT or *Sema3e* KO mice at P5. The white dotted boxes in the left images are shown in the inset images, which were captured in a single plane using a high-resolution confocal microscope. Scale bar, 500 μm. (B-C) Quantification of the density (intensity/area) (B) and the area size (C) at P5. Error bars, mean ±SEM; ns p>0.05, ***p<0.001 by Student's t test; n=18 per group (6 sections/mouse). (D) Diagram depicting the width (red line) of the striatonigral pathway. (E) Quantification of the width of the striatonigral projections at P5. Error bars, mean ± SEM; ***p<0.001 by Student's t test; WT, n=15, KO, n=14. (3-4 sections/mouse). (F) Representative images showing parasagittal sections of brains from WT or *Sema3e*-KO mice at P5. White boxes are magnified on the right panels. Scale bar, 500 μm. The phenotype of misguided striatonigral projections was observed in three out of four *Sema3e*-KO mice at P5 (white arrowheads). (G) The number of deviated axonal bundles within the corresponding area (white boxes in (F)). Error bars, mean ± SEM; *p<0.05 by Student's t test; n=4 mice for WT, n=4 mice for KO.

Figure S11. No Mtss1 was found in endothelial cells at E14.5, and no vascular defects were observed in *Mtss1*-conditional KO mice. (A) Fluorescence *in situ* hybridization for *Plxnd1* mRNA (green) and *Mtss1* mRNA (red) in the brain and dorsal trunk at E14.5. White dotted boxes are shown in the inset image on the bottom. Scale bars, 100 μm for brain, 50 μm for dorsal trunk. (B) 3D vascular reconstruction analysis images after CD31 immunostaining and tissue clearing obtained using multifunctional fast confocal microscopy Dragonfly 502w. (C) Western blotting to analyze Mtss1 expression after AP-Sema3E (2 nM) treatment in human umbilical vein endothelial cells (HUVECs) or human cortical microvessel endothelial cells (HCMEC/D3). Error bars, mean ± SEM; ns p>0.05 by Mann–Whitney test; AP, n=4, AP-Sema3E, n=4 for HUVECs, ns p>0.05 by Student's t test; AP, n=4, AP-Sema3E, n=4 for HCMEC/D3s in four dependent experiments. Source data 1. Western blots shown in Figure S11C.

1375

1376 **Figure S12. Schematic summary showing striatonigral projection development via a serial reciprocal**

1377 **interaction of the Sema3E-Plexin-D1-Mtss1 complex.**

1378

1379 Video information

1380 **Video 1-2. Time-lapse live imaging of Plexin-D1-GFP-positive vesicles (Green) from wild-type MSNs at**
1381 **DIV6.**

1382 **Video 3-4. Time-lapse live imaging of Plexin-D1-GFP-positive vesicles (Green) from Mtss1 cKO MSNs at**
1383 **DIV6.**

Figure 1

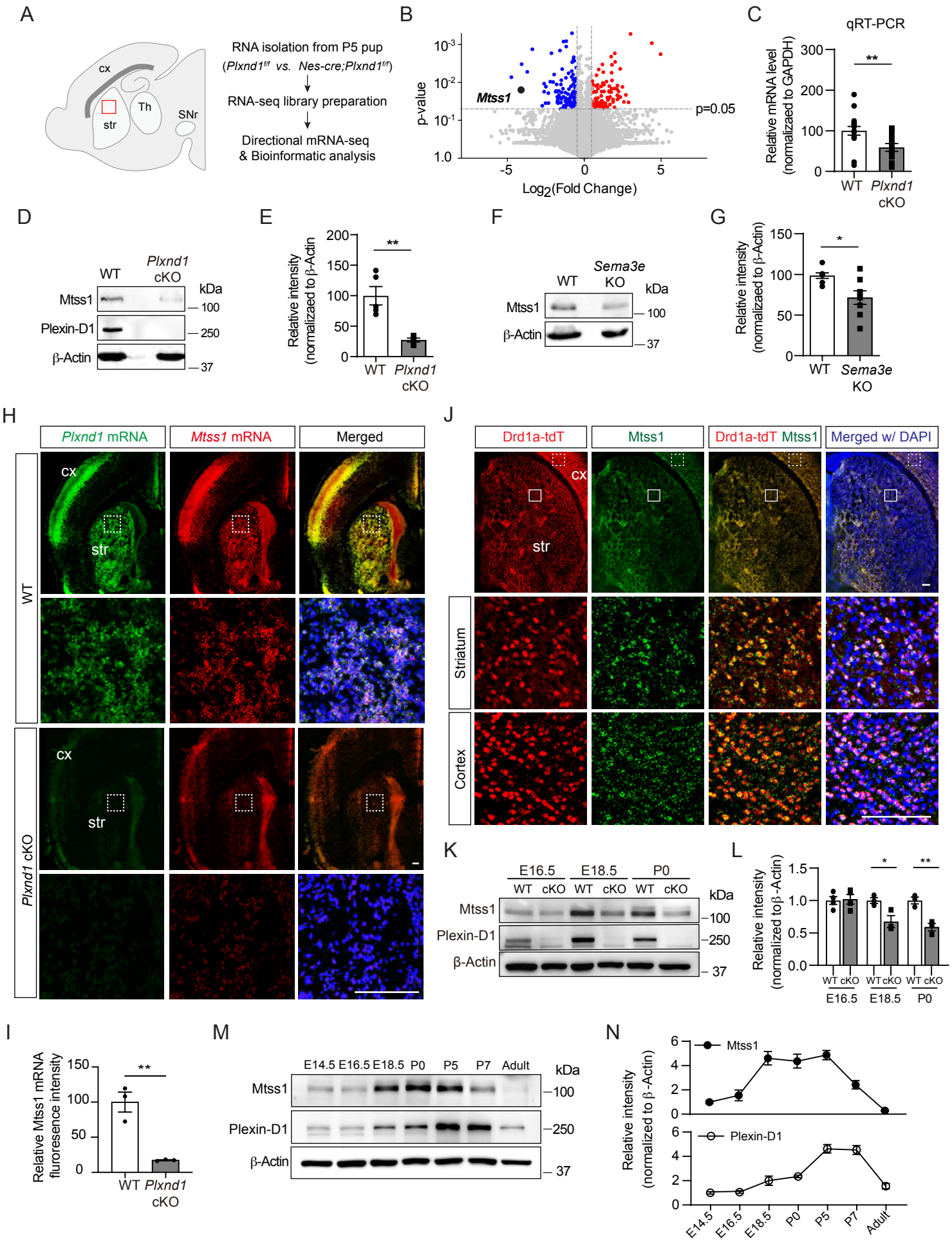
A
cx
str
Th
SNr
RNA isolation from P5 pup
(Plxnd1f/f vs. Nes-cre;Plxnd1f/f)
RNA-seq library preparation
Directional mRNA-seq
& Bioinformatic analysis
B
Mtss1
p-value
p=0.05
Log2(Fold Change)
C
qRT-PCR
Relative mRNA level
(normalizaed to GAPDH)
WT
Plxnd1
cKO
D
WT
Plxnd1
cKO
kDa
Mtss1
Plexin-D1
β-Actin
E
Relative intensity
(normalizaed to β-Actin)
F
Sema3e
KO
G
Relative intensity
(normalizaed to β-Actin)
H
Plxnd1 mRNA
Mtss1 mRNA
Merged
WT
Plxnd1 cKO
J
Drd1a-tdT
Mtss1
Drd1a-tdT Mtss1
Merged w/ DAPI
Striatum
Cortex
K
E16.5
E18.5
P0
L
Relative intensity
(normalized to β-Actin)
I
Relative Mtss1 mRNA
fluroresence intensity
M
E14.5 E16.5 E18.5 P0 P5 P7 Adult
N
Relative intensity
(normalized to β-Actin)
Mtss1
Plexin-D1

Figure 2

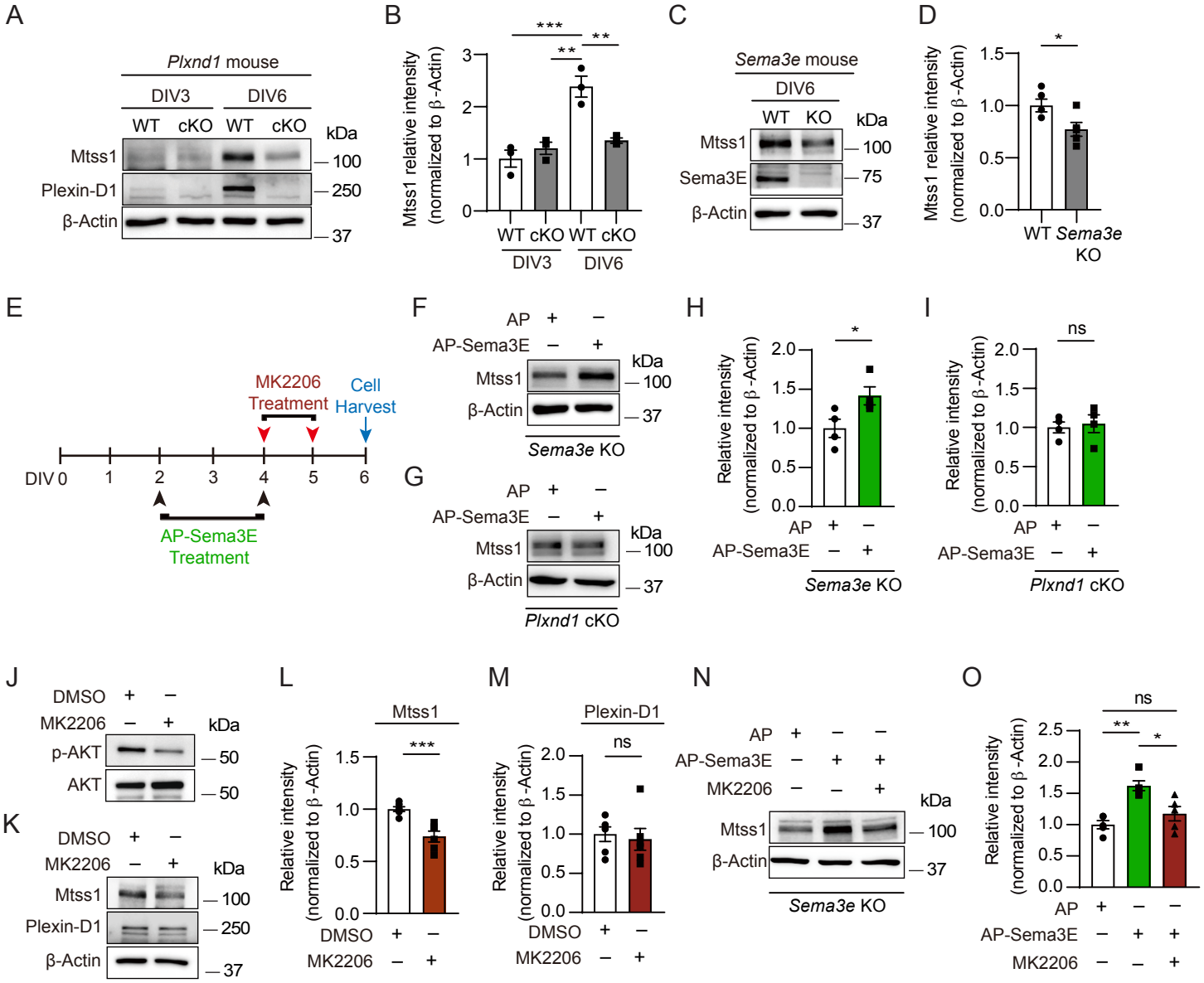
A
Plxnd1 mouse
DIV3
DIV6
WT cKO WT cKO
kDa
Mtss1
Plexin-D1
β-Actin
100
250
37
B
Mtss1 relative intensity (normalized to β-Actin)
***
**
**
WT cKO WT cKO
DIV3 DIV6
C
Sema3e mouse
DIV6
WT KO
kDa
Mtss1
Sema3E
β-Actin
100
75
37
D
Mtss1 relative intensity (normalized to β-Actin)
*
WT Sema3e KO
E
MK2206 Treatment
Cell Harvest
DIV 0 1 2 3 4 5 6
AP-Sema3E Treatment
F
AP + –
AP-Sema3E – +
kDa
Mtss1
β-Actin
100
37
Sema3e KO
G
AP + –
AP-Sema3E – +
kDa
Mtss1
β-Actin
100
37
Plxnd1 cKO
H
Relative intensity (normalized to β-Actin)
*
AP + –
AP-Sema3E – +
Sema3e KO
I
Relative intensity (normalized to β-Actin)
ns
AP + –
AP-Sema3E – +
Plxnd1 cKO
J
DMSO + –
MK2206 – +
kDa
p-AKT
AKT
50
50
K
DMSO + –
MK2206 – +
kDa
Mtss1
Plexin-D1
β-Actin
100
250
37
L
Mtss1
Relative intensity (normalized to β-Actin)
***
DMSO + –
MK2206 – +
M
Plexin-D1
Relative intensity (normalized to β-Actin)
ns
DMSO + –
MK2206 – +
N
AP + – –
AP-Sema3E – + +
MK2206 – – +
kDa
Mtss1
β-Actin
100
37
Sema3e KO
O
Relative intensity (normalized to β-Actin)
ns
**
*
AP + – –
AP-Sema3E – + +
MK2206 – – +

Figure 3

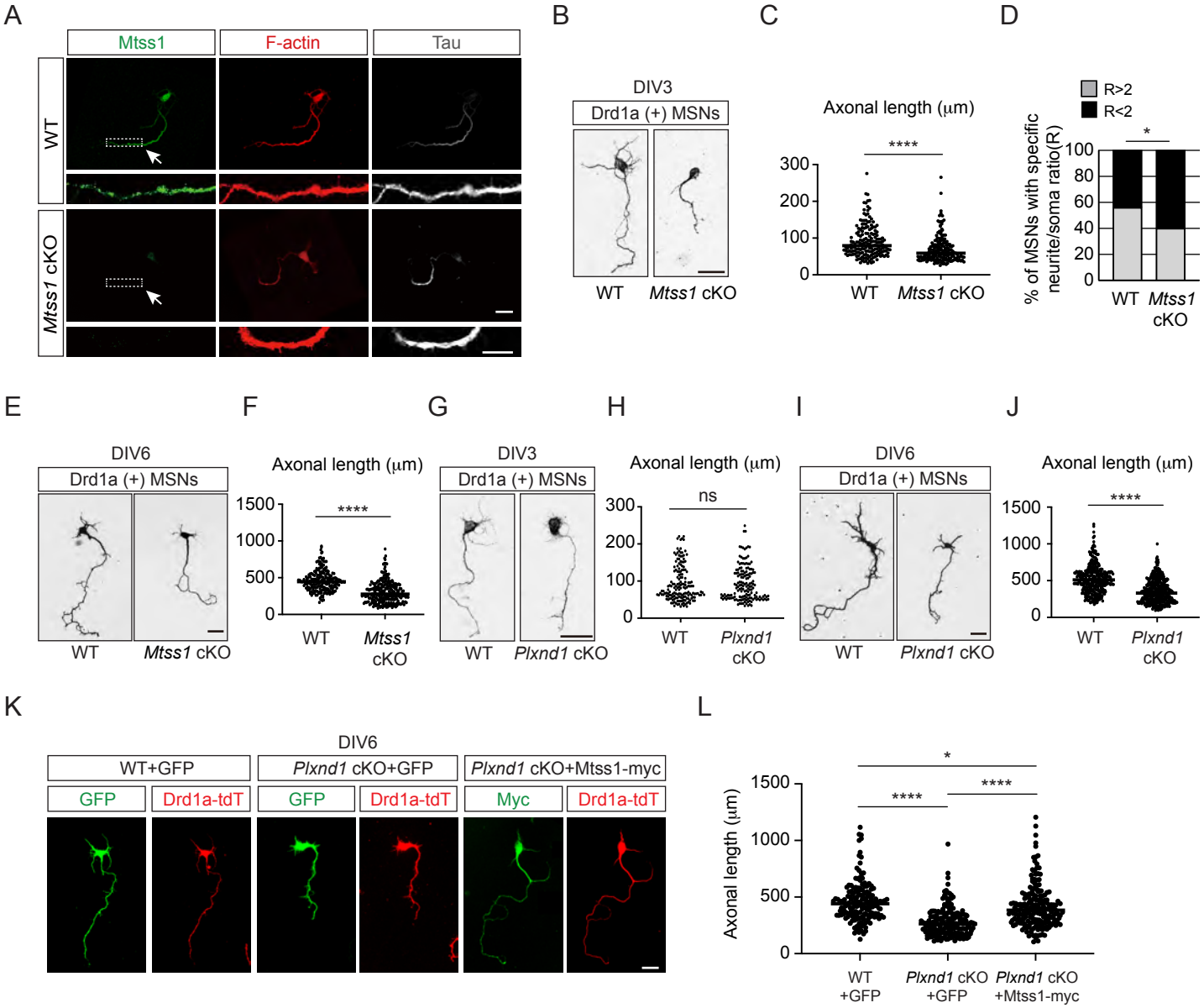
A
Mtss1
F-actin
Tau
WT
Mtss1 cKO
B
DIV3
Drd1a (+) MSNs
WT
Mtss1 cKO
C
Axonal length (μm)
****
300
200
100
0
WT
Mtss1 cKO
D
R>2
R<2
*
% of MSNs with specific neurite/soma ratio(R)
100
80
60
40
20
0
WT
Mtss1 cKO
E
DIV6
Drd1a (+) MSNs
WT
Mtss1 cKO
F
Axonal length (μm)
****
1500
1000
500
0
WT
Mtss1 cKO
G
DIV3
Drd1a (+) MSNs
WT
Plxnd1 cKO
H
Axonal length (μm)
ns
300
200
100
0
WT
Plxnd1 cKO
I
DIV6
Drd1a (+) MSNs
WT
Plxnd1 cKO
J
Axonal length (μm)
****
1500
1000
500
0
WT
Plxnd1 cKO
K
DIV6
WT+GFP
Plxnd1 cKO+GFP
Plxnd1 cKO+Mtss1-myc
GFP
Drd1a-tdT
GFP
Drd1a-tdT
Myc
Drd1a-tdT
L
*
****
****
Axonal length (μm)
1500
1000
500
0
WT +GFP
Plxnd1 cKO +GFP
Plxnd1 cKO +Mtss1-myc

Figure 4

A

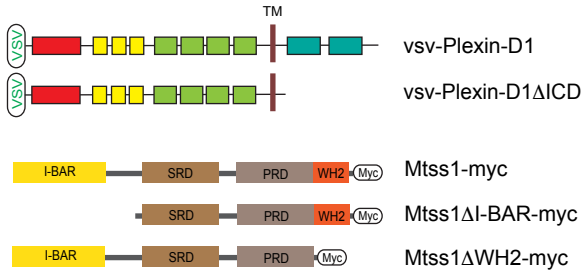

B

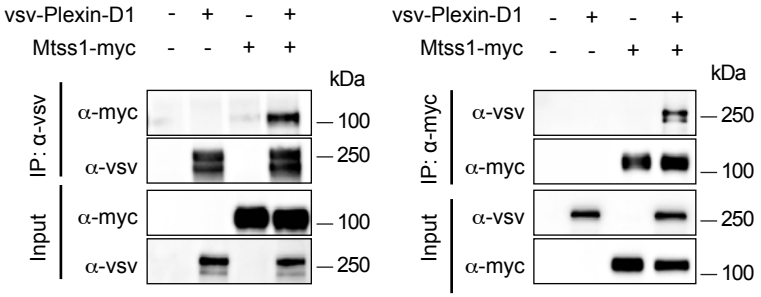

C

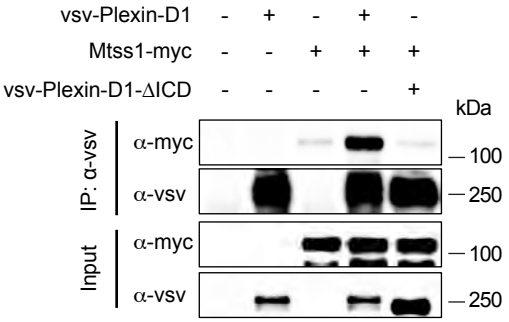

E

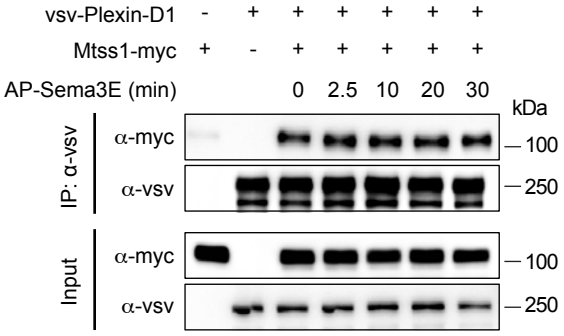

F

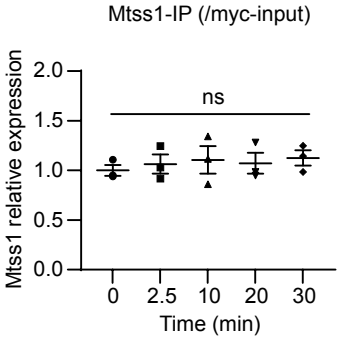

D

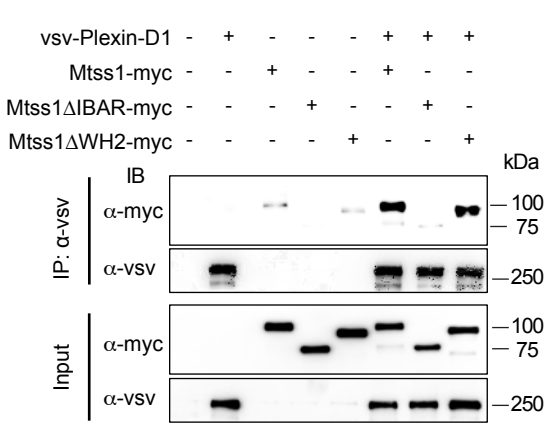

G

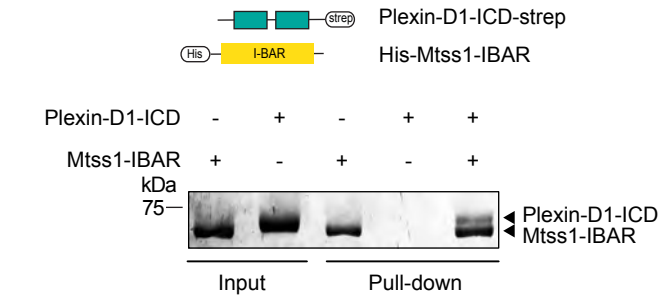

Figure 5

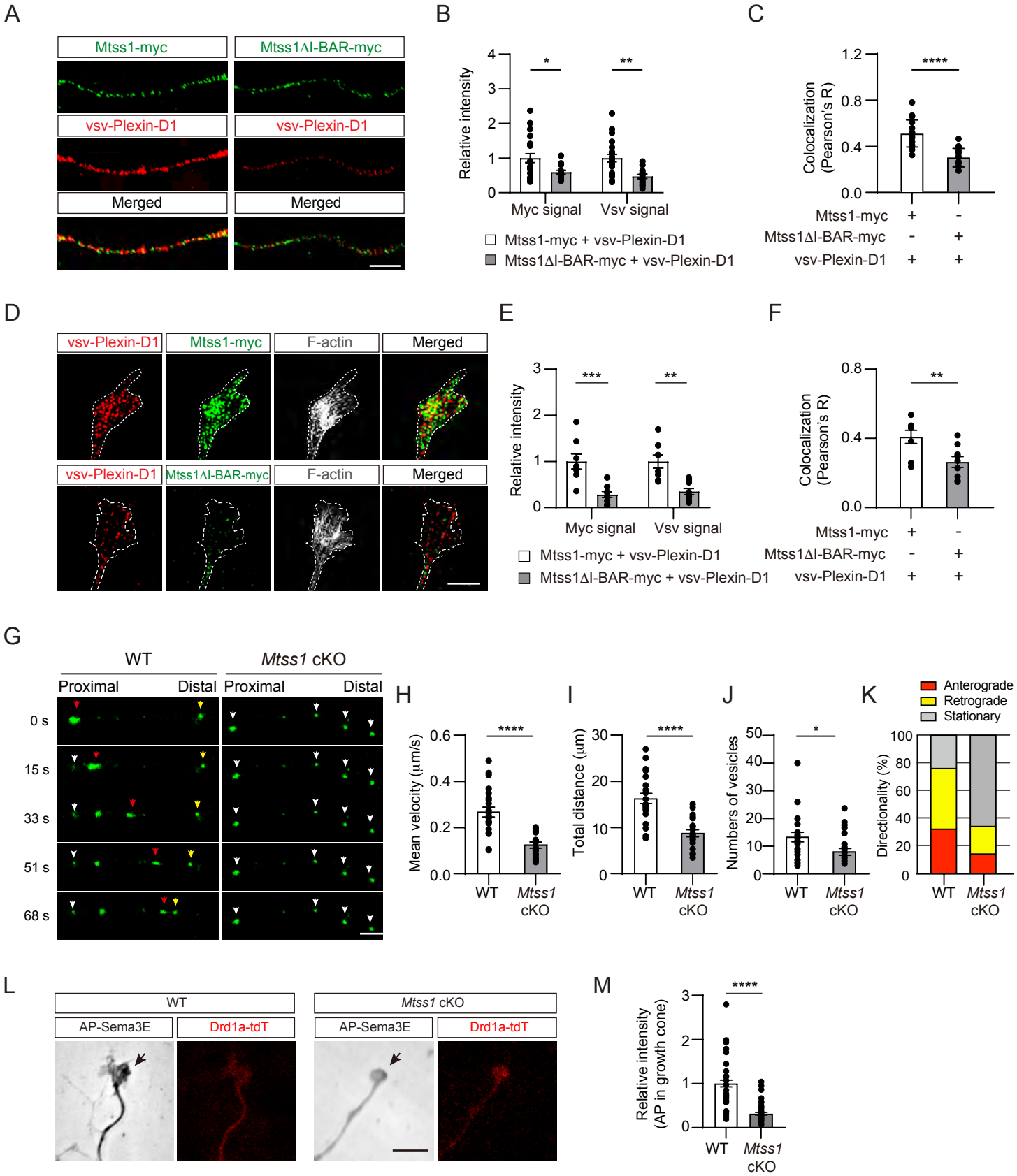
A
Mtss1-myc
Mtss1ΔI-BAR-myc
vsv-Plexin-D1
vsv-Plexin-D1
Merged
Merged
B
Relative intensity
Myc signal
Vsv signal
Mtss1-myc + vsv-Plexin-D1
Mtss1ΔI-BAR-myc + vsv-Plexin-D1
C
Colocalization (Pearson's R)
Mtss1-myc
Mtss1ΔI-BAR-myc
vsv-Plexin-D1
D
vsv-Plexin-D1
Mtss1-myc
F-actin
Merged
vsv-Plexin-D1
Mtss1ΔI-BAR-myc
F-actin
Merged
E
Relative intensity
Myc signal
Vsv signal
Mtss1-myc + vsv-Plexin-D1
Mtss1ΔI-BAR-myc + vsv-Plexin-D1
F
Colocalization (Pearson's R)
Mtss1-myc
Mtss1ΔI-BAR-myc
vsv-Plexin-D1
G
WT
Mtss1 cKO
Proximal
Distal
Proximal
Distal
0 s
15 s
33 s
51 s
68 s
H
Mean velocity (μm/s)
WT
Mtss1 cKO
I
Total distance (μm)
WT
Mtss1 cKO
J
Numbers of vesicles
WT
Mtss1 cKO
K
Anterograde
Retrograde
Stationary
Directionality (%)
WT
Mtss1 cKO
L
WT
Mtss1 cKO
AP-Sema3E
Drd1a-tdT
AP-Sema3E
Drd1a-tdT
M
Relative intensity (AP in growth cone)
WT
Mtss1 cKO

Figure 6

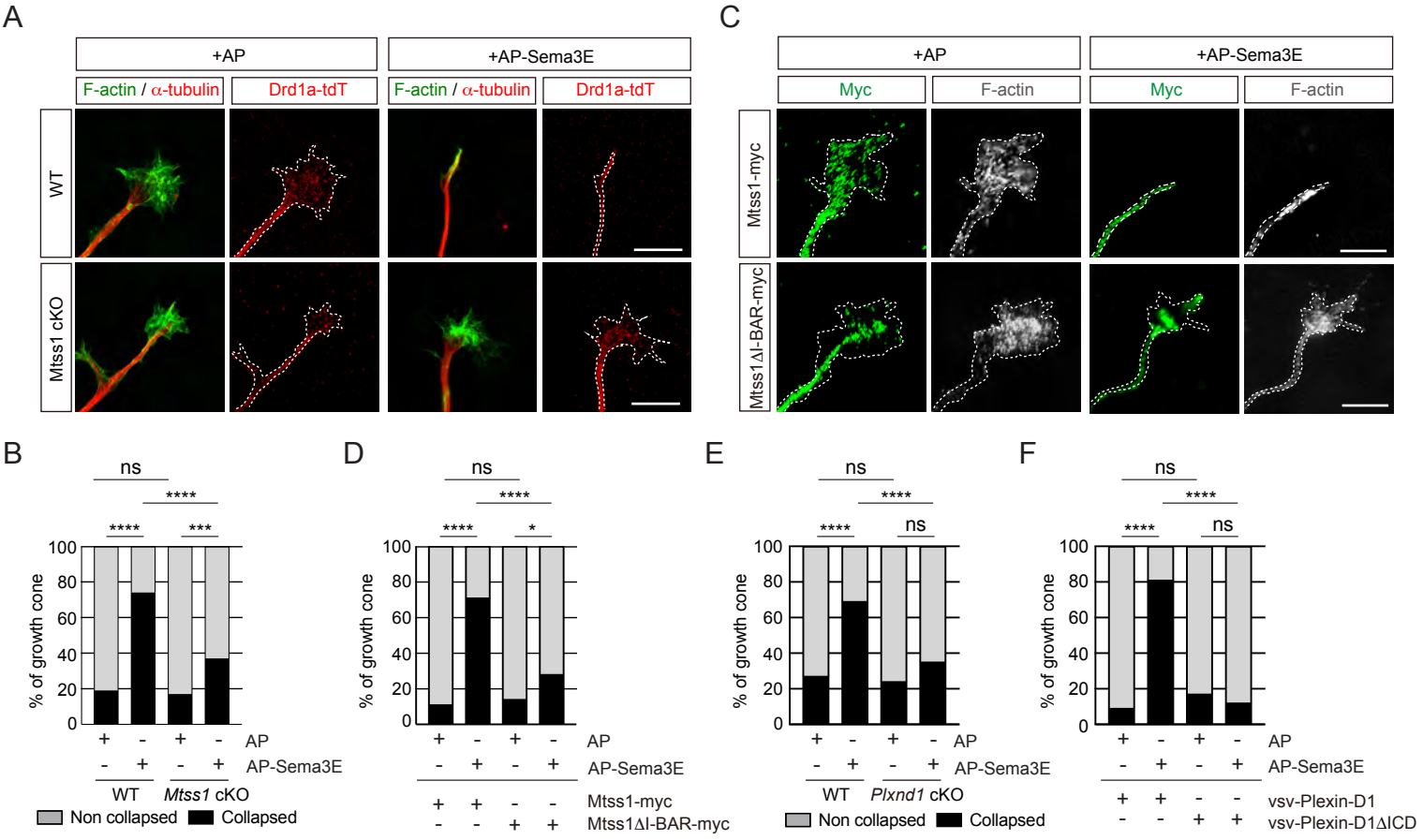
A
+AP
+AP-Sema3E
F-actin / α-tubulin
Drd1a-tdT
WT
Mtss1 cKO
C
Myc
F-actin
Mtss1-myc
Mtss1ΔI-BAR-myc
B
D
E
F
ns
****
***
*
% of growth cone
AP
AP-Sema3E
WT
Mtss1 cKO
Plxnd1 cKO
Mtss1-myc
Mtss1ΔI-BAR-myc
vsv-Plexin-D1
vsv-Plexin-D1ΔICD
Non collapsed
Collapsed

Figure 7

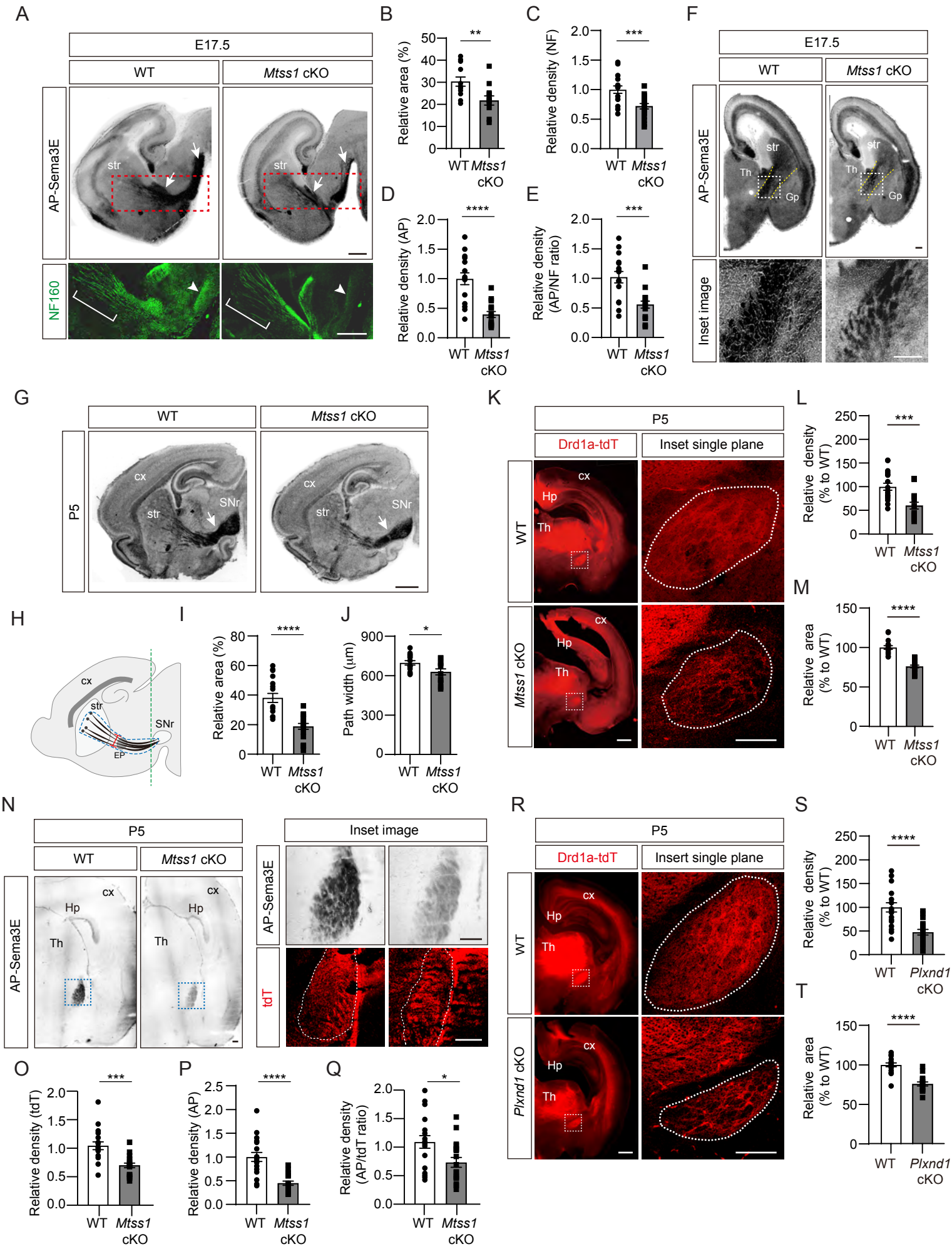
A
E17.5
WT
Mtss1 cKO
AP-Sema3E
NF160
str
B
Relative area (%)
C
Relative density (NF)
D
Relative density (AP)
E
Relative density (AP/NF ratio)
F
Th
Gp
Inset image
G
P5
cx
SNr
H
EP
I
Relative area (%)
J
Path width (μm)
K
Drd1a-tdT
Inset single plane
Hp
L
Relative density (% to WT)
M
Relative area (% to WT)
N
Inset image
tdT
O
Relative density (tdT)
P
Relative density (AP)
Q
Relative density (AP/tdT ratio)
R
Insert single plane
Plxnd1 cKO
S
T

Figure 8

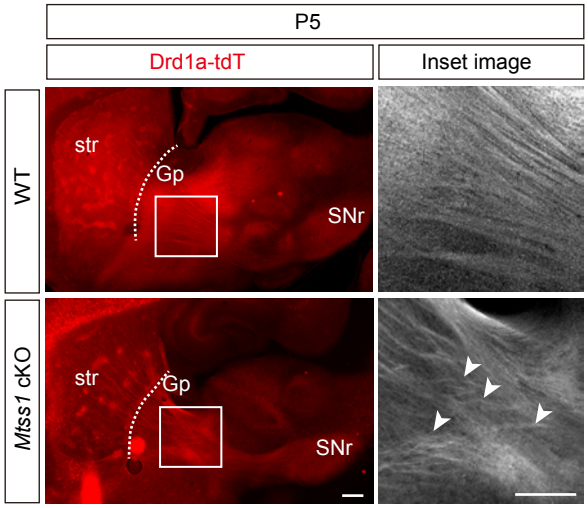
A
P5
Drd1a-tdT
Inset image
WT
Mtss1 cKO
str
Gp
SNr

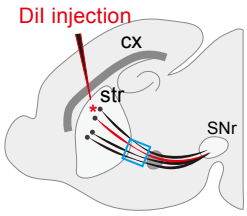
B
DiI injection
cx
str
SNr

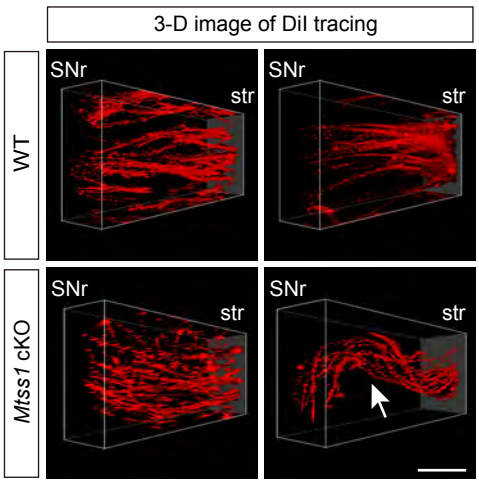
C
3-D image of DiI tracing
WT
Mtss1 cKO
SNr
str

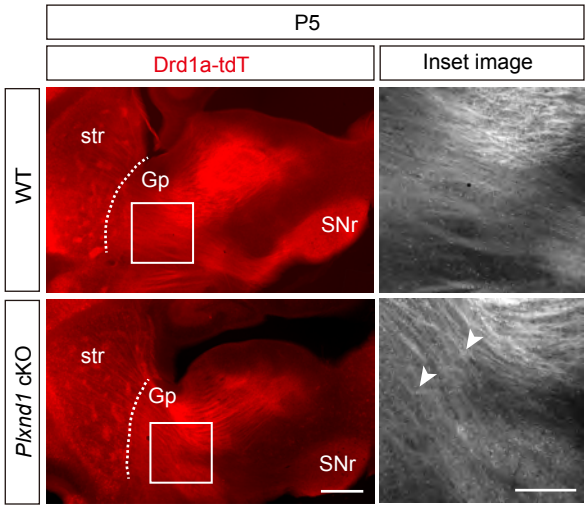
D
P5
Drd1a-tdT
Inset image
WT
Plxnd1 cKO
str
Gp
SNr

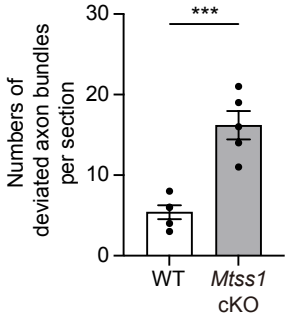
E
Numbers of deviated axon bundles per section
30
20
10
0
***
WT
Mtss1 cKO

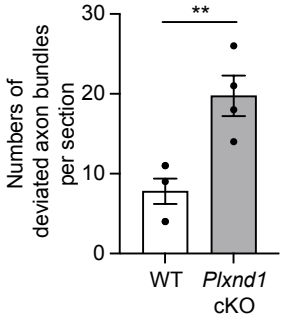
F
Numbers of deviated axon bundles per section
30
20
10
0
**
WT
Plxnd1 cKO

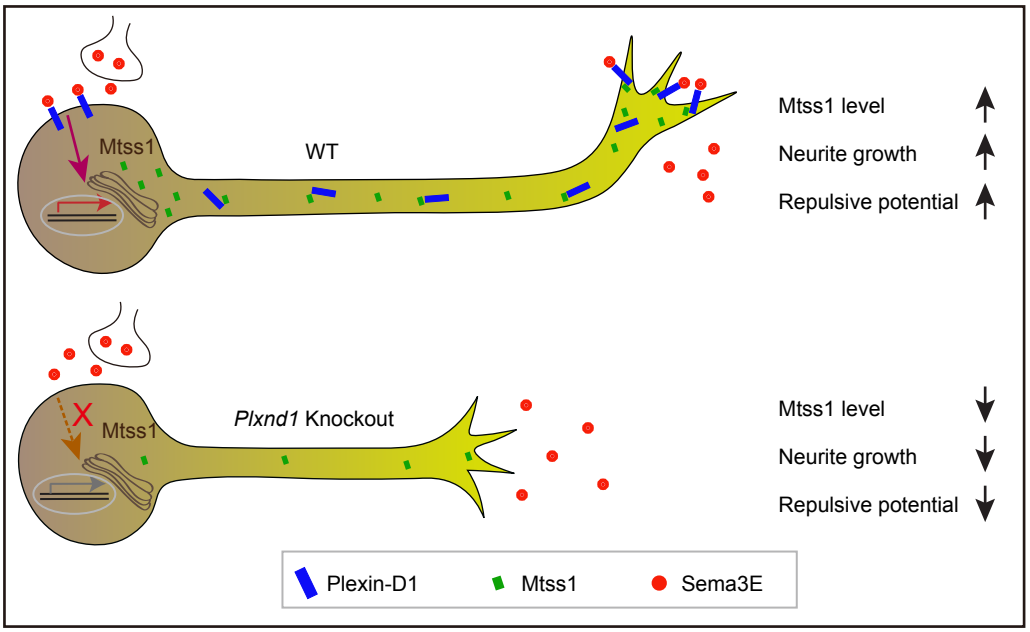
J
Mtss1
WT
Mtss1 level
Neurite growth
Repulsive potential
Mtss1
Plxnd1 Knockout
Mtss1 level
Neurite growth
Repulsive potential
Plexin-D1
Mtss1
Sema3E

Supplementary Figure 1

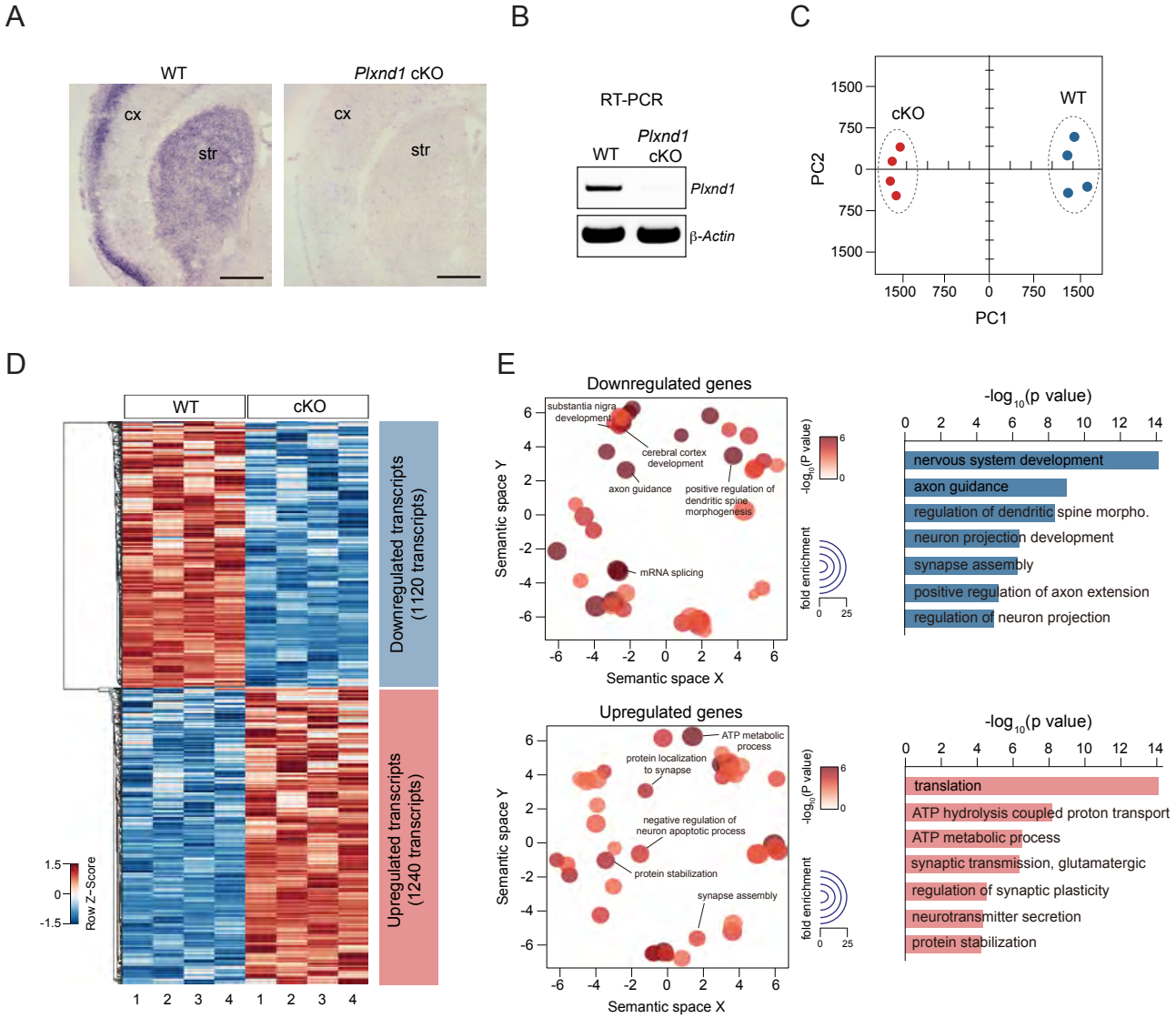

Supplementary Figure 2

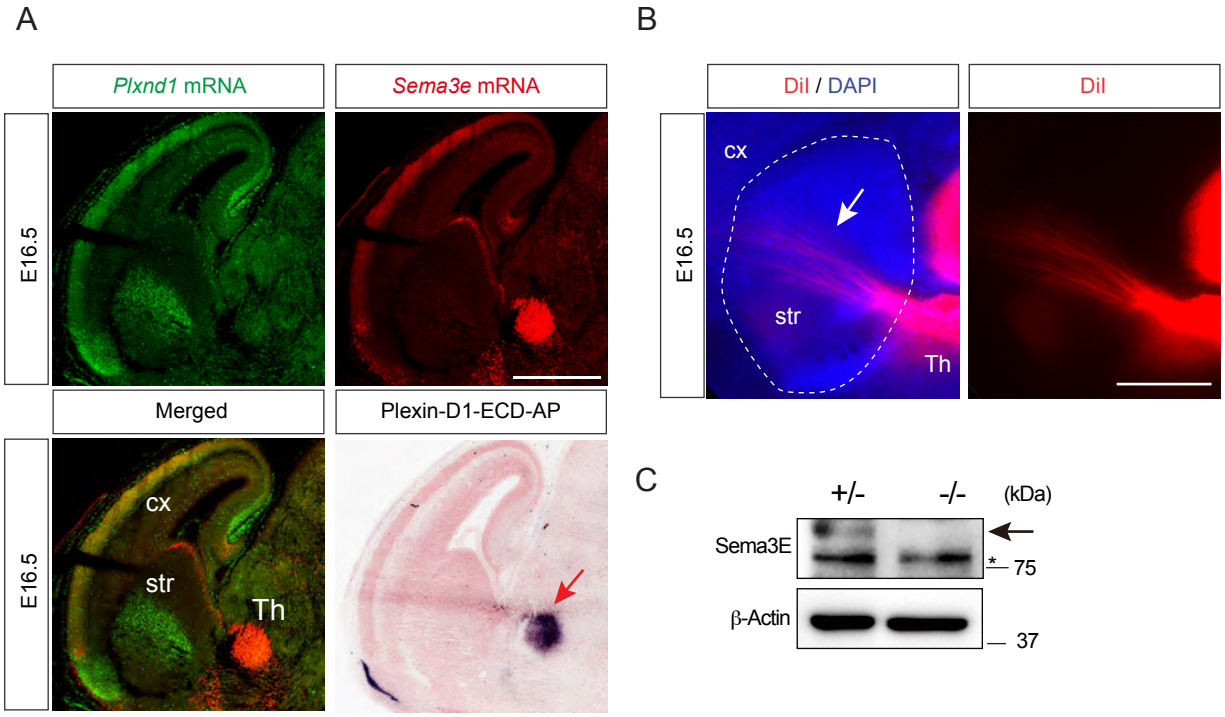

Supplementary Figure 3

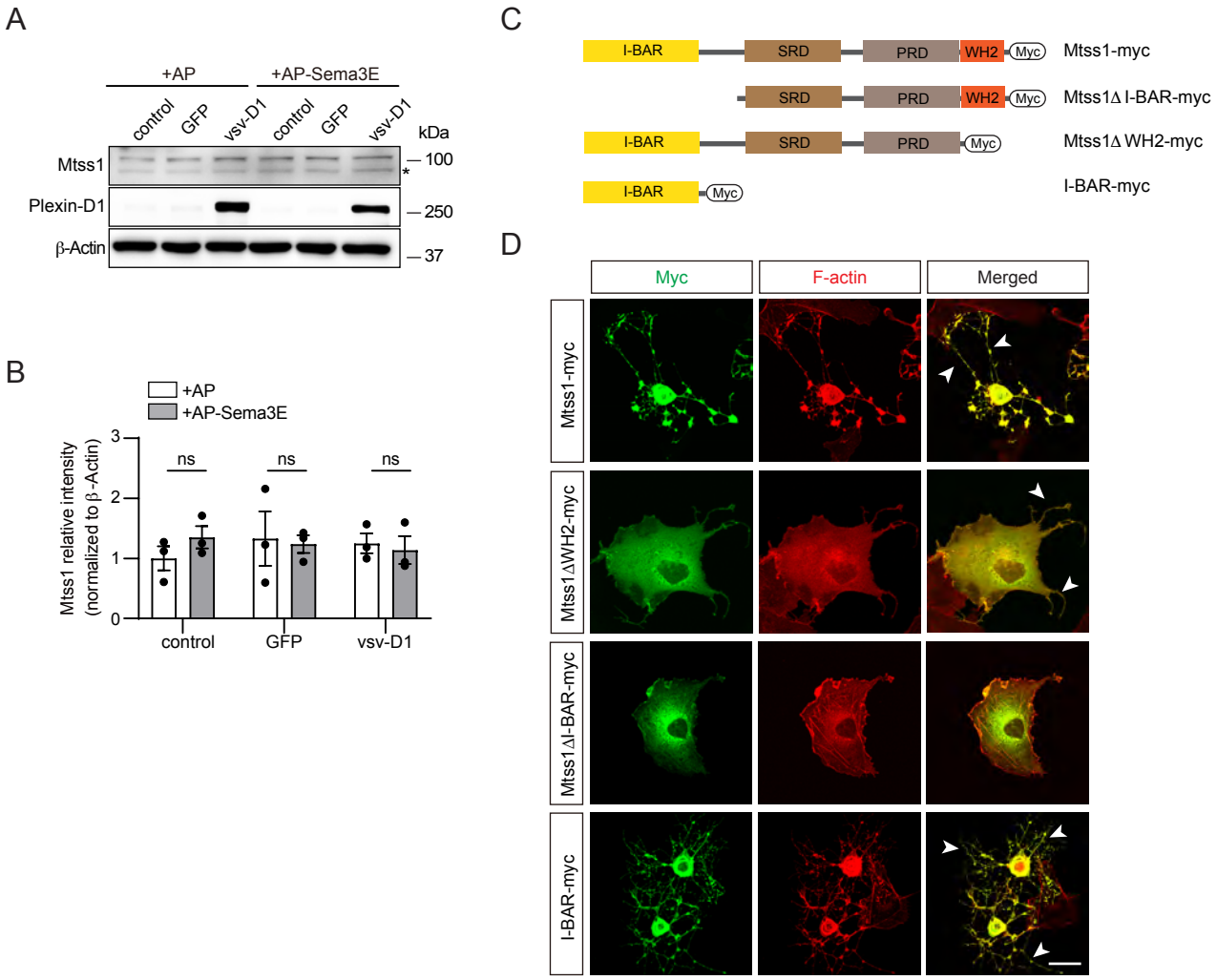

Supplementary Figure 4

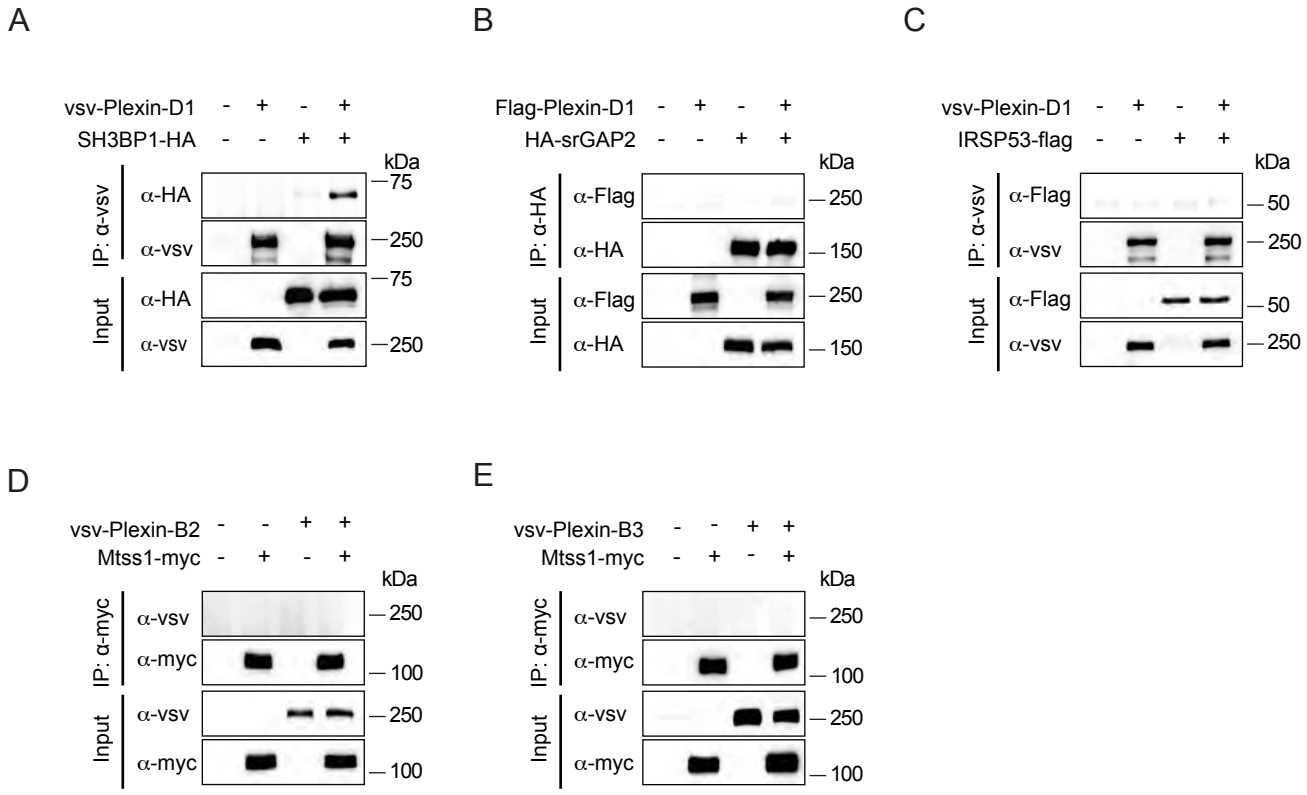

Supplementary Figure 5

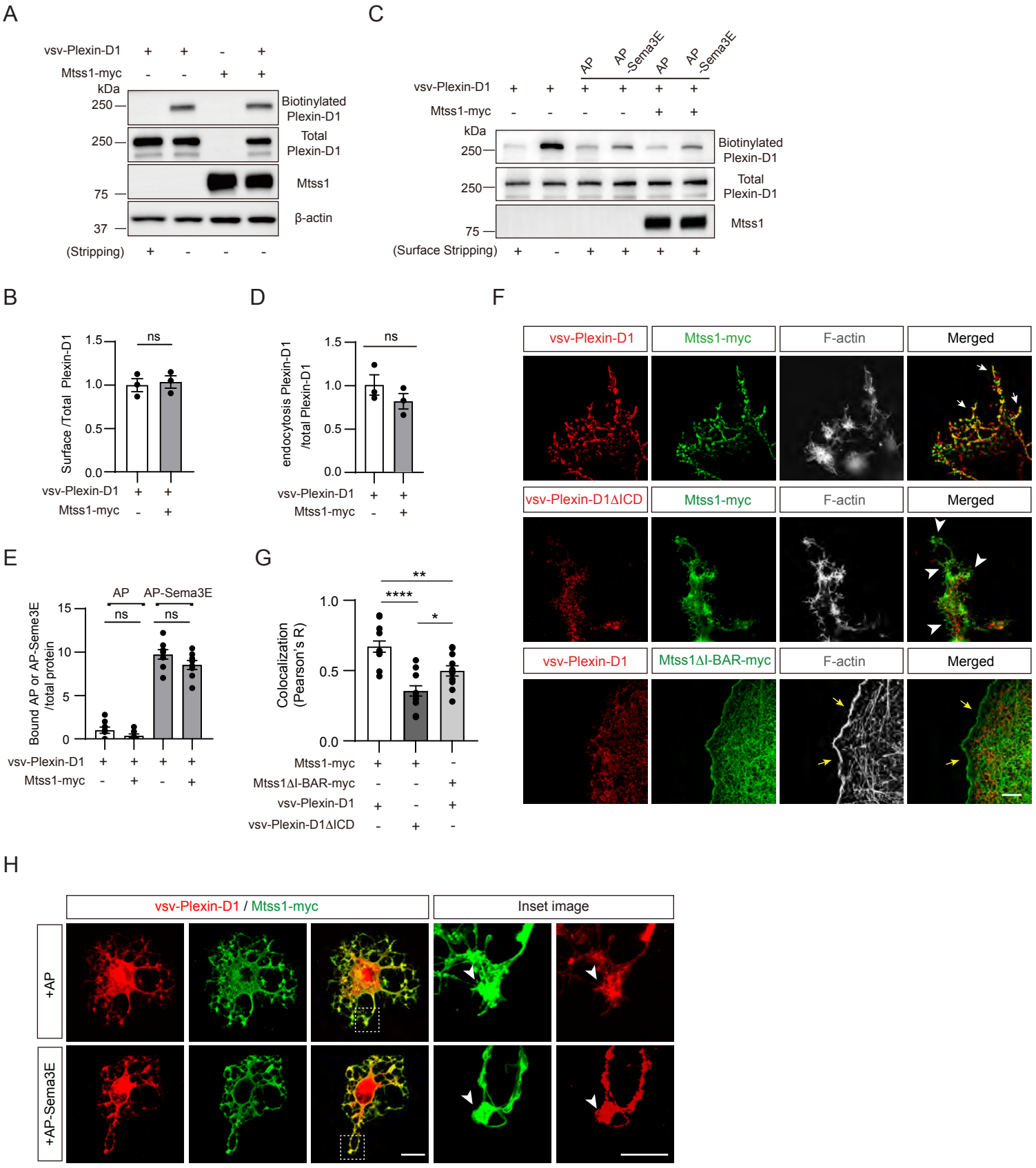

Supplementary Figure 6

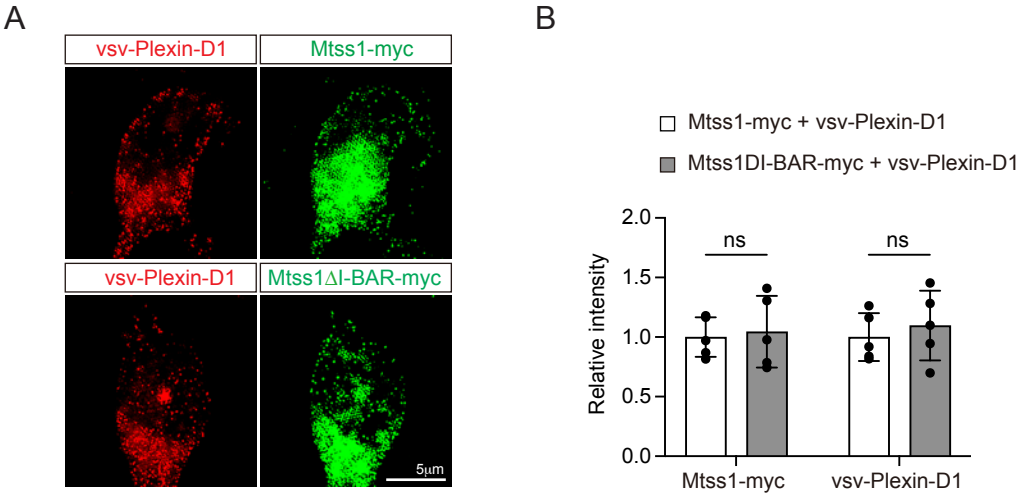

Supplementary Figure 7

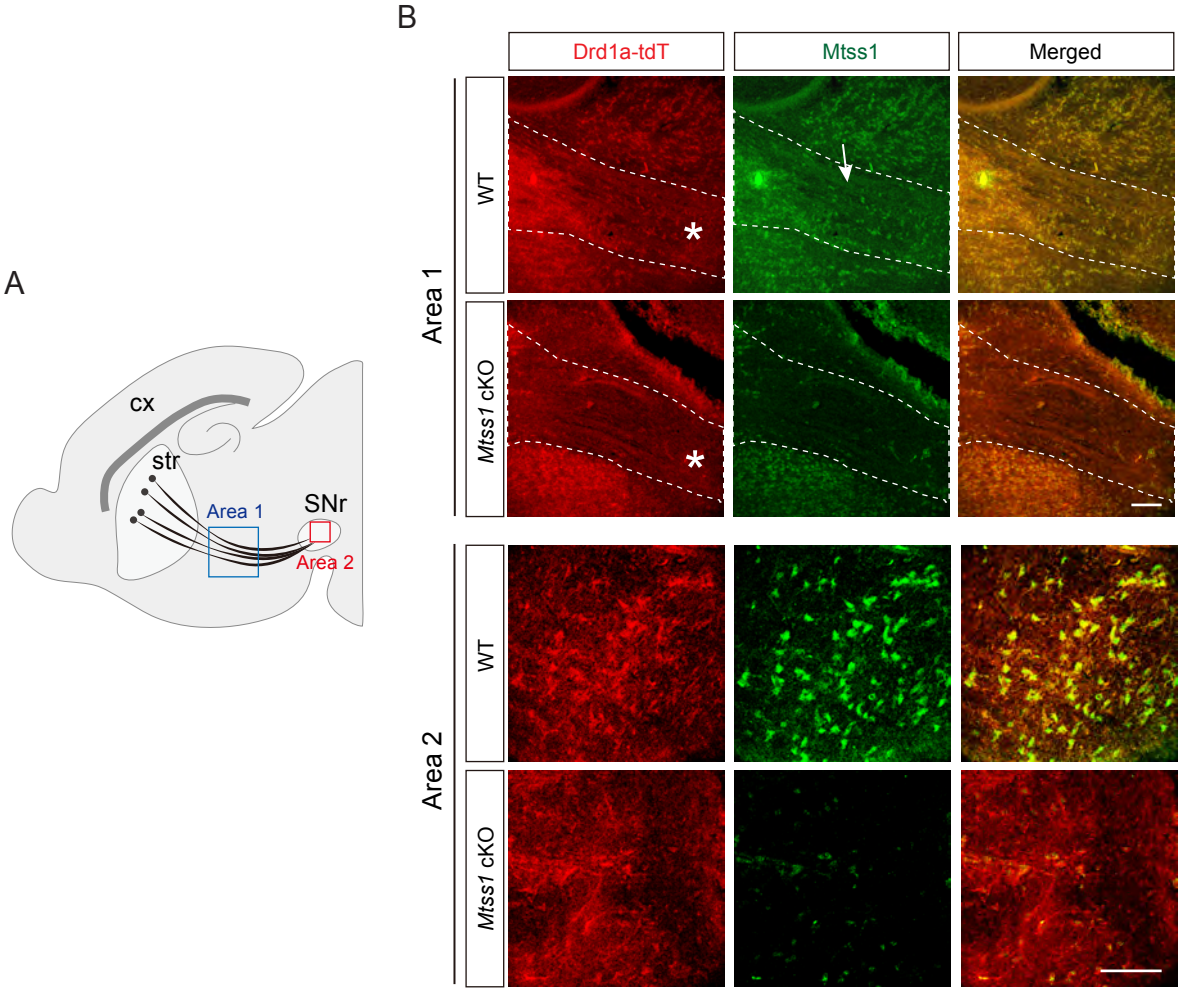

Supplementary Figure 8

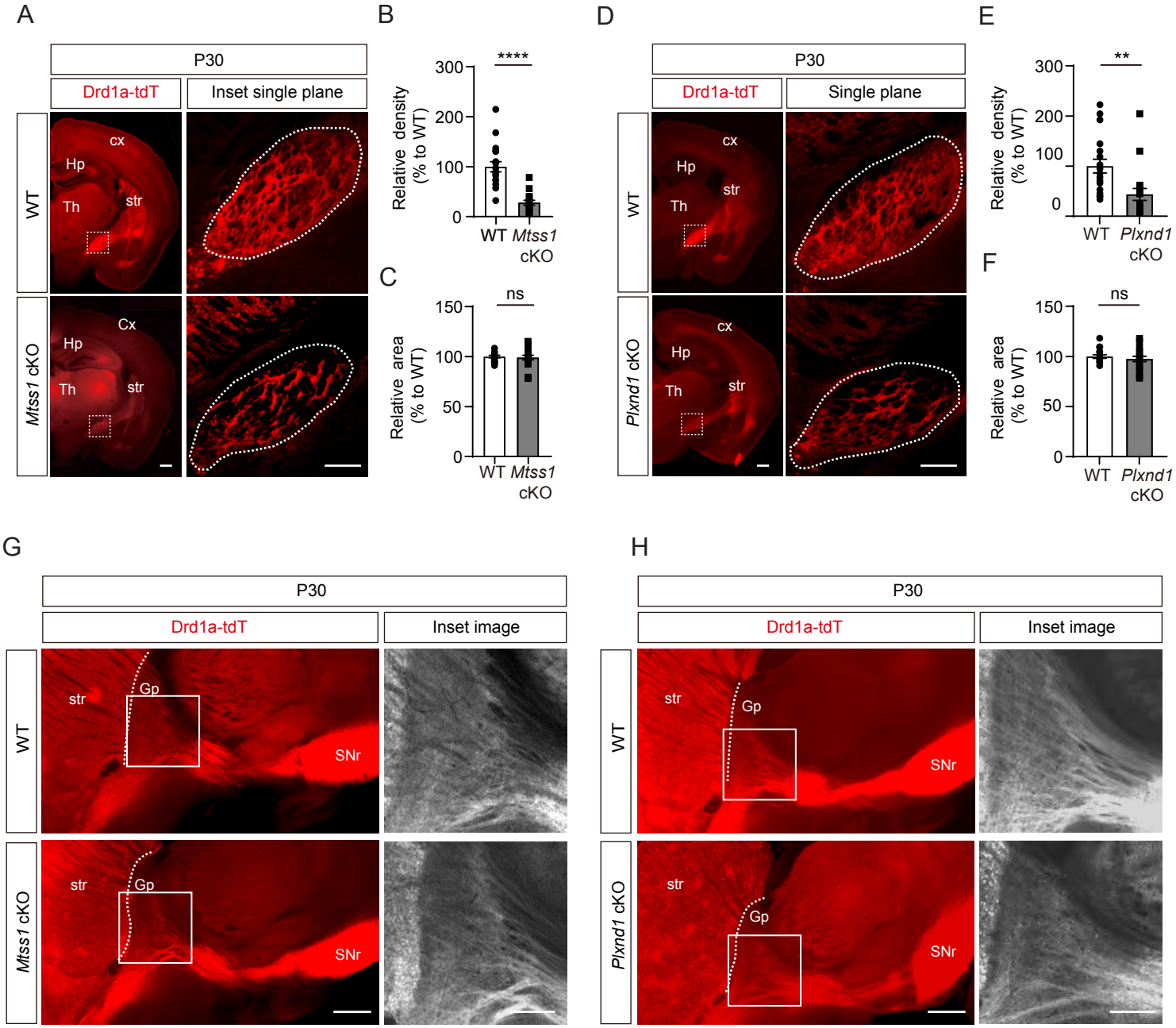

Supplementary Figure 9

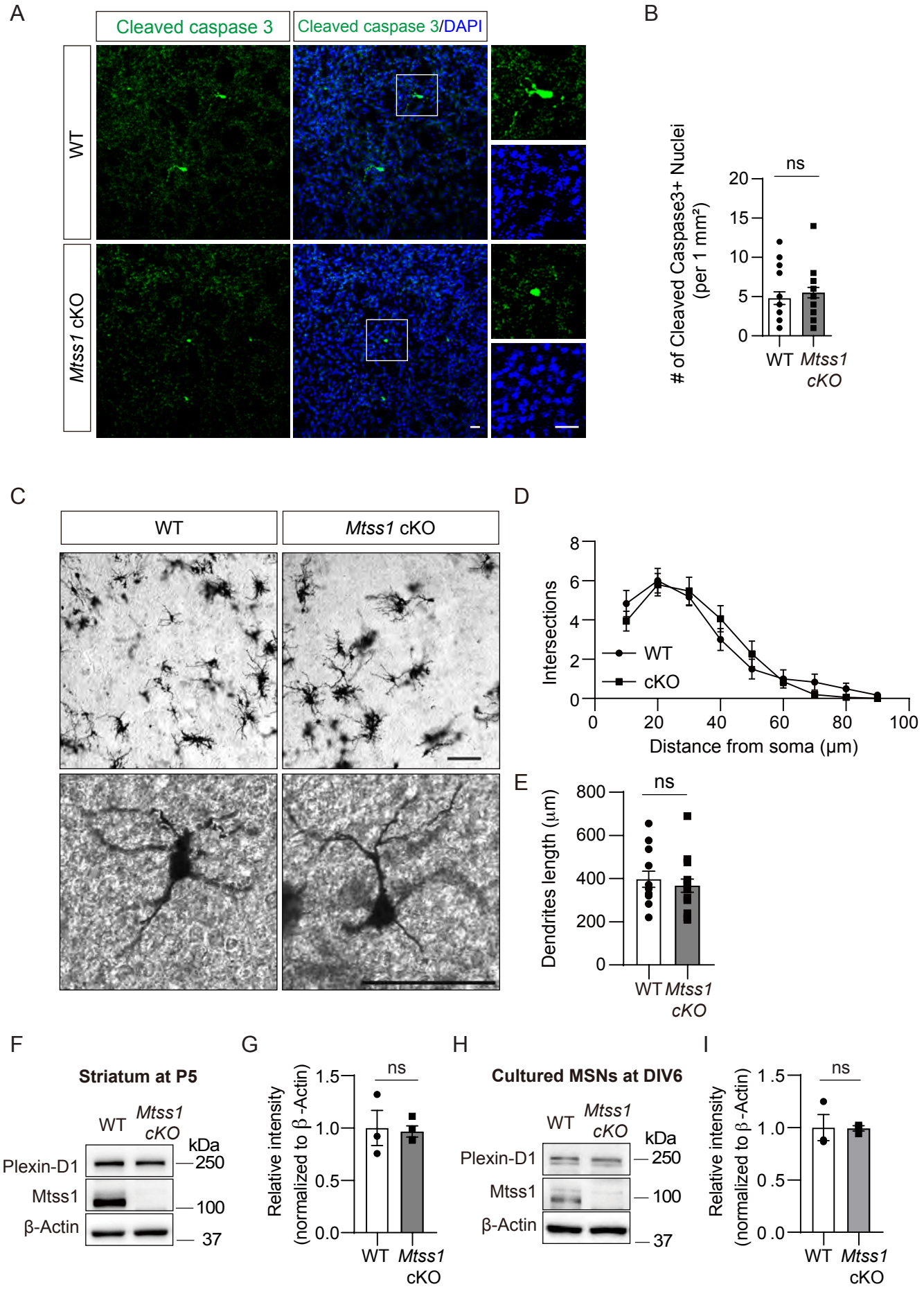

Supplementary Figure 10

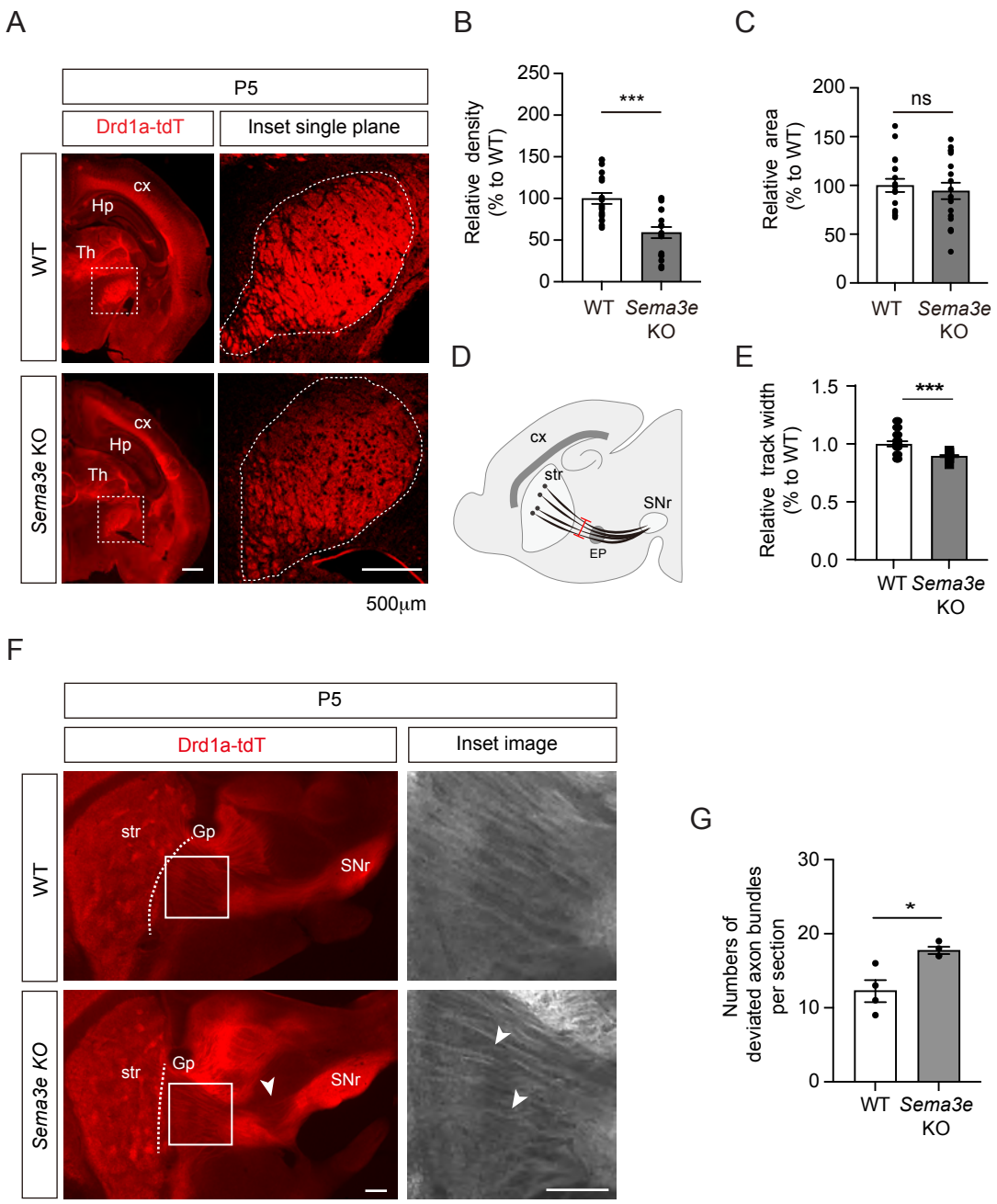

Supplementary Figure 11

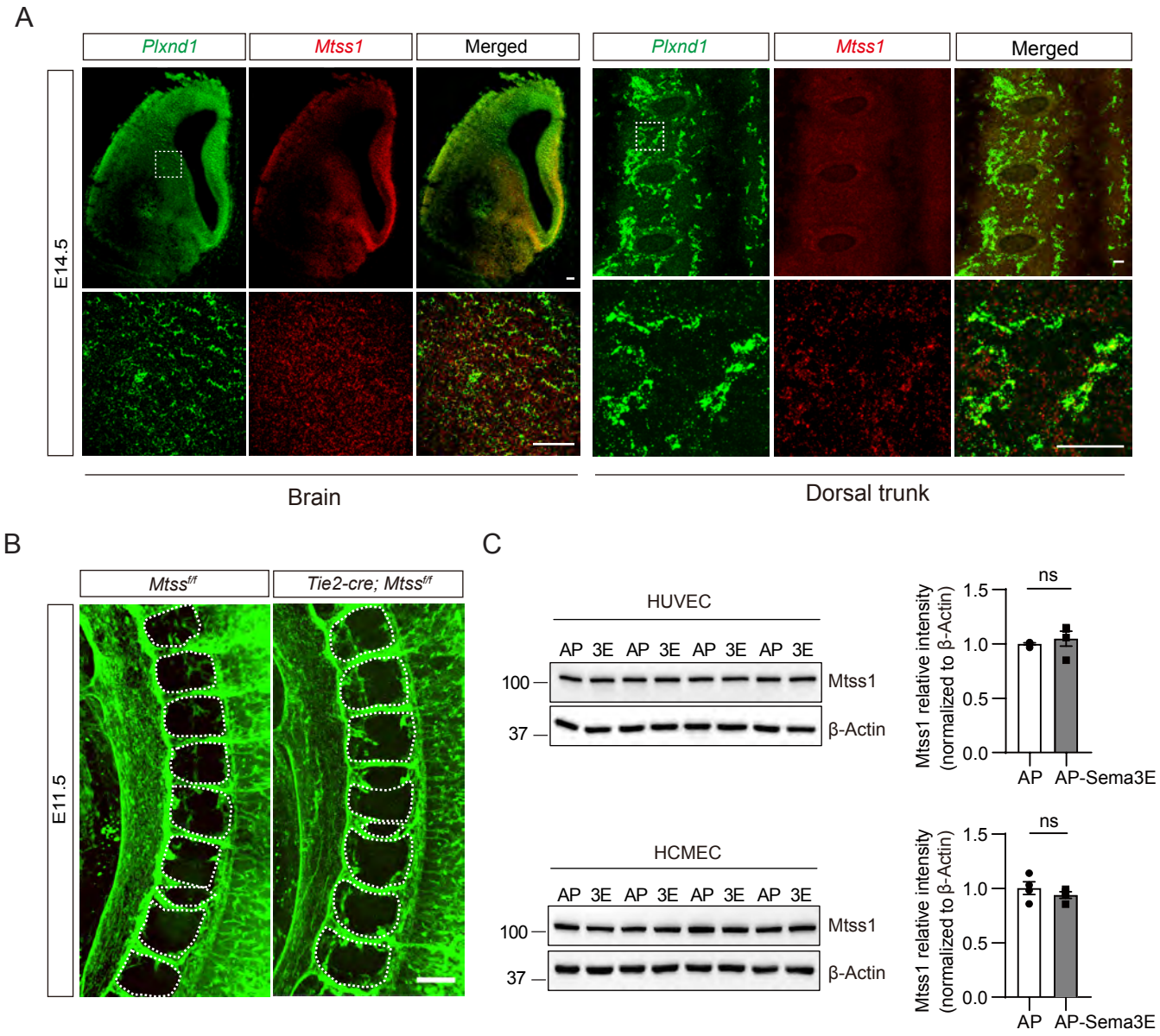
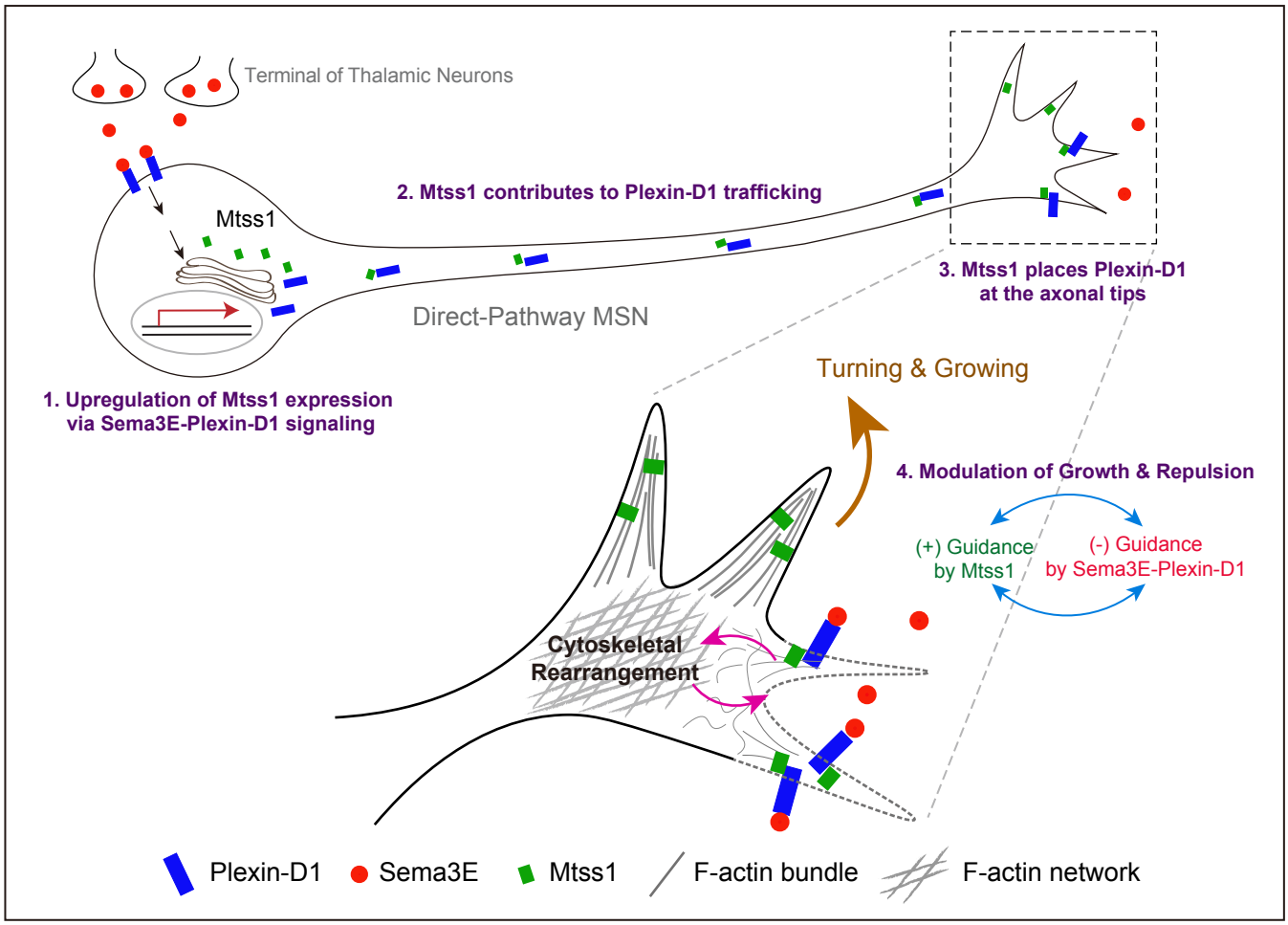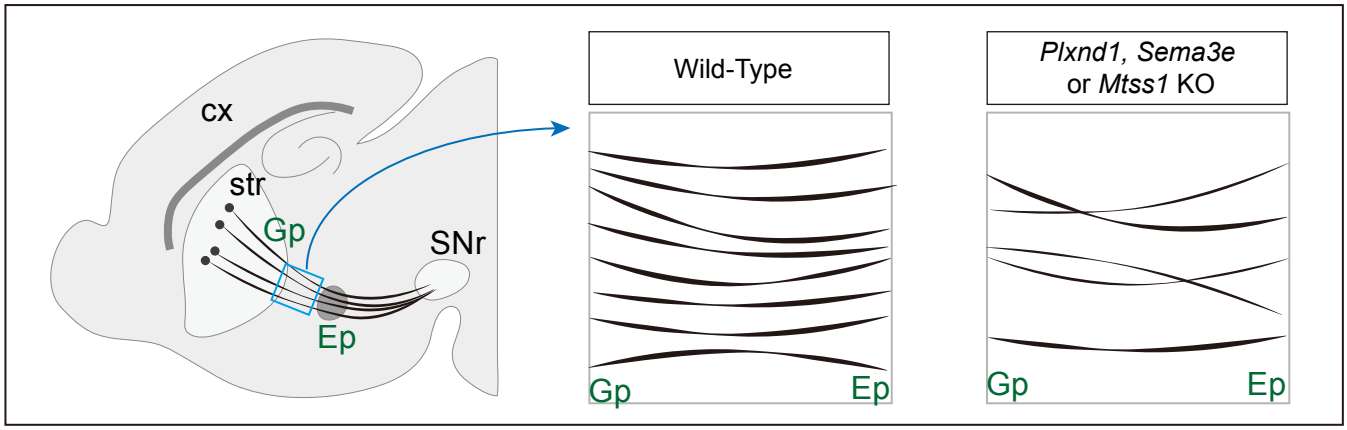
Supplementary Figure 12